2022

IMPROVING THE ANALYSIS AND PREDICTION OF COASTAL FLOODING DURING HURRICANE LANDFALLS THROUGH COUPLED AND INTEGRATED MODELING

Md Arifur Rahman

IMPROVING THE ANALYSIS AND PREDICTION OF COASTAL FLOODING DURING HURRICANE LANDFALLS THROUGH COUPLED AND INTEGRATED MODELING

By

MD ARIFUR RAHMAN

DISSERTATION

Submitted in partial fulfillment of the requirements
for the degree of Doctor of Philosophy at
The University of Texas at Arlington
December 2022

Arlington, Texas, USA

Supervising Committee:

- Dr. Yu Zhang, Supervising Professor
- Dr. Michelle Hummel
- Dr. Jessica Eisma
- Dr. Mohammad Shahidul Islam
- Dr. Saeed Moghimi

ABSTRACT

As the intensity and frequency of landfalling tropical storms are likely on the rise in a warming climate, coastal communities are increasingly being exposed to flooding caused by storm surges compounded by heavy rainfall. Prediction and reanalysis of storm surges, especially compound flooding, rely on wind and pressure fields either from parametric tropical cyclone wind models or numerical weather model reanalysis. Both are subject to significant errors during landfall. Besides, land surface attributes and different storm structures influence the intensity and location of compound flooding in coastal areas. Therefore, this dissertation aims to improve the analysis and prediction of coastal flooding during landfalls through integrated modeling by addressing the above research questions. The dissertation is comprised of three main components. First, the relative accuracy of HWRF reanalysis and a parametric wind model (i.e., Holland 10) during the landfall of Hurricane Florence has been assessed, and the impacts of the wind forcing on storm surge simulations have been estimated. In this component of the study, we validated each wind forcing using an extensive surface data set collected at public and commercial platforms and then used as input forcing to a 2-D coastal hydrodynamic model (i.e., Delft3D Flexible Mesh) to produce storm surge along the Carolina coasts and major sounds. This study reveals that the wind fields from HWRF are overall more accurate than those based on H10 for the periphery of the storm, though they exhibit limitations in resolving high wind speeds near the center. However, HWRF wind fields exhibit a progressively negative bias after landfall, likely due to deficiencies of the model in representing boundary layer processes and to the lack of assimilation of the surface product after landfall to compensate for these deficiencies. When we used HWRF reanalysis wind and pressure fields as the atmospheric forcings to the Delft3D-FM model, it yielded more accurate peak surges simulations. However, there is a severe underestimation of the surge along the

shoreline close to the track center. The peak surge simulations by Delft3D are biased low when driven by H10, even though over several locations, the H10 model overpredicts surface wind speeds. This contrast highlights the importance of resolving wind fields further away from the center to reproduce storm surges and associated coastal flooding accurately.

The second component of the dissertation focuses on defining an alternative metric to identify regions with consistently large compound zones and land surface controls on the intensity and locations of compound flooding caused by Hurricane Florence. A prominent feature of this event is the storm surge penetrated more than 60 km inland through the Neuse River in North Carolina, causing more than 3-m surge upstream outside of the coastal zone. This surge most likely has magnified the fluvial flood peak that arrived subsequently by producing the backwater effects. Therefore, this investigation focuses on the impacts of land surface controls on the intensity of compound effects. We developed an integrated ocean-riverine hydrodynamic model using the Delft3D-FM suite. The integrated model ingests inflow from National Water Model 2.1 reanalysis. The model undergoes calibration to accurately capture the peak surge up to the surge-dominated and fluvial zones. The calibrated model is then used in sensitivity runs to appraise the impacts of land surface control. The findings from this study confirm that the baseline metric using the compound ratio of 20% and 80% is insufficient to explicitly define Florence's compound zone. However, changing the threshold values of the compound ratio in alternative metrics to 5% and 95 % demonstrates significant compounding effects. So, the alternative metric is more conservative than the baseline. In addition, the presence of salt marsh significantly impacts the compound zone, and the compound area reduces by 35 % for the highest intensity of salt marsh. Therefore, Managing flood hazards using a more conservative estimation will minimize the risk of property damage and save lives.

In the third element, we investigate three contrasting storm events over the Amite River watershed in Louisiana to identify the effects of different storm structures on the intensity and location of compound flooding over the region. To this end, we extensively calibrate an integrated modeling framework (i.e., Delft3D-FM) in simulating compound flooding effects resulting from rainfall runoff, astronomical tides, storm surges, and atmospheric forcing within the Lakes Maurepas and Pontchartrain drainage basins. The calibration was performed on two contrasting events: a rainfall-dominated flood event in 2016 and a surge-dominated (i.e., Hurricane Isaac) event in 2012. Then the resulting model was utilized for Hurricane Ida in 2021 to ascertain the extent of the compound and transition zone. Our intermediate results suggest that surge-dominated events only generate floods within the transition zones, whereas rainfall-dominated events contribute to watershed flooding. However, the study reveals that a surge event with heavy rainfall is the actual cause of compound flooding. Moreover, the location and intensity of compound flooding vary in u/s and d/s. This innovative study suggests that a coupled model can be used for operational use in predicting compound flooding in coastal areas as the model reduces computational time by avoiding the complexity of implementing different modeling frameworks separately with multiple parameter estimations. Hence, the outcome of this study will help policymakers take prompt and informed actions during storm events.

KEYWORDS: Hurricane, wind model, storm surge, reanalysis, Delft3D-FM, Florence, compound flooding, land surface control, NWM

ACKNOWLEDGMENTS

First, I would like to offer gratitude to my committee chair and supervisor Dr. Yu Zhang for supporting me financially and academically during my PhD journey. He encourages me to work with great enthusiasm and consistency. I learn how to work rigorously and independently with the help of my supervisor. He helps me to enhance my knowledge and contribute to the field of my interest by publishing research articles in well-known journals and conferences. Dr. Zhang helped me find internships in NWC and AECOM that expanded my horizon to develop my professional career. I got the opportunity to interact and collaborate with scientific communities and professionals in water resources engineering.

This research work was made possible by NSF Grants 1908862/1909367 and through a faculty startup package for Dr. Yu Zhang, the Texas Water Development Board through Contract 1800012276, and NOAA through Grant NA19OAR4310347. I want to express my gratitude to my committee members—Dr. Michelle Hummel, Dr. Jessica Eisma, Dr. Mohammad Shahidul Islam, and Dr. Saeed Moghimi for providing their thoughts and guidance to improve my research and supporting me with the necessary data and technical assistance. I also would like to thank Dr. Ali Abdolali (NOAA) and Dr. Meredith Carr (ERDC) for supporting me as additional board members, Zaizhong Ma at NCEP, Clint Dawson at UT Austin, and Casey Dietrich at NCSU for providing necessary data and technical assistance. I would also like to thank my current and former colleagues at the Hydrology and Water Resources Laboratory, Dr. Mohammadvaghef Ghazvinian, Dr. Yanjun Gan, Dr. Behzad Nazari, Dr. Haojin Shen, Farhad Hassani, and Nahal Maymandi.

Finally, I would like to thank my family for their continuous support and encouragement; without their support, the journey of my Ph.D. would not have been completed.

DEDICATION

I dedicate this dissertation to my beloved parents, dearest nephew, Tazwar, and niece, Rawnaf.

TABLE OF CONTENTS

LIST OF TABLES

LIST OF FIGURES

Chapter 1 General Introduction

Coastal communities are increasingly being exposed to flooding caused by storm surges compounded by heavy rainfall because of the increasing trend in intensity and frequency of landfalling tropical storms due to climate change (Milly *et al.*, 2002; Moftakhari *et al.*, 2015; Bevacqua *et al.*, 2019). A combination of wind, tide, waves, and rainfall across various scales drives flooding over coastal and transition zone. Flooding can emerge either from ocean surges, high river discharges, and extreme rainfalls in the upstream watersheds or a combination of these flood drivers (Zheng *et al.*, 2013; Wahl *et al.*, 2015; Bilskie and Hagen, 2018). Most of the time, damages from the combined hazards during compound flooding are more severe than that of individual sources (Zscheischler *et al.*, 2018). For instance, Florence in 2018 caused significant flooding in the vicinity of the Neuse River in North Carolina, USA, especially at New Bern, because of the combined effect of heavy precipitation (i.e., 900 mm) and high surge (i.e., 3 m) from the Atlantic Ocean (Ye, Huang, *et al.*, 2020). In addition, compound flooding can result from tropical and extratropical cyclones (Cho *et al.*, 2012; Li *et al.*, 2006; Valle-Levinson *et al.*, 2020).

Furthermore, the attributes of the land surface, such as the presence of marshland and other vegetation, may control the intensity and location of compound flooding in the coastal regions. Different storm structures also influence the intensity of compound flooding. Because some storms are surge-dominated, some are rainfall-dominated, and others make landfall with high surges and heavy precipitation, causing massive compounding over the region, especially upstream locations.

However, the definition of compound flooding is debatable. There is no well-established metric to identify the regions with the consistently significant compounding effect. Instead, a recent study conducted by Ye *et al.*, 2020 for hurricane Florence introduced a new metric based on a dominance map. They define dominance as a percentage of the total disturbances. For instance, if the disturbance from an individual forcing is more than 80%, then the location is dominant for that forcing; otherwise, the area will be a compound zone. However, this definition of compound zone based on the dominance map is time-dependent, which sometimes misleading, and cannot detect compound zone for storms with varying structures, especially those landed with secondary peaks. As a result, there is a need to introduce a time- and storm-independent alternative metric to define compound flooding holistically in identifying regions with consistently large compounding effects.

Eventually, improving the resilience of coastal communities compounding effect requires accurate analysis and predictions of coastal flooding. In contrast, complex interactions among multiple processes cannot be modeled efficiently by coupling isolated models. As a result, realistic representation and prediction of storm surges remain challenging. The reasons are manifold. These include uncertainties in atmospheric forcing (Cardone and Cox, 2009; Dietrich *et al.*, 2018; Mayo and Lin, 2019; Abdolali *et al.*, 2021); a lack of available high-quality and high-resolution bathymetric data in shallow areas as well as insufficient grid resolution to resolve the topo-bathy in complex coastal regions (Hell *et al.*, 2012; Jacob and Stanev, 2021; Acosta-Morel *et al.*, 2021); a lack of available high-quality water level records during past tropical storms for model calibration (Asher *et al.*, 2019); under- or misrepresentations of physical processes pertaining to flow and atmosphere-ocean momentum exchange under robust wind regime and in shallow waters (Olabarrieta *et al.*, 2012), a lack of coupling of different model components which have a direct effect on each other (i.e., atmospheric forcing, storm surge, wave, and hydrology; Ma et al., 2020; Santiago-Collazo *et al.*, 2019).

Therefore, the overarching goal of this research work is to improve the understanding of the coastal processes and interaction among flood drivers for enhancing the prediction of coastal flooding and develop a better tool that can integrate all processes by avoiding the complexity of multiple modeling systems. This dissertation is comprised of three main elements. The first element is motivated by the need to determine the relative strengths and deficiencies of the parametric wind model and NWP reanalysis as forcings for storm surge simulations. It offers detailed, comparative analyses of wind and pressure fields from HWRF and the Holland (2010) wind model for Hurricane Florence and the impacts on storm surge simulations driven by each forcing. The second element is motivated by the need to define the alternative metric to identify the regions with consistently significant compounding effects across storms (i.e., Florence) and assess the impacts of land surface controls in determining the maximum impact caused by storm surges. In the third element, we study the effect of various storm structures on the intensity of compound flooding. Here, we selected three different storms, such as surge-dominated, rainfall-dominated, and storm with high surges and heavy precipitations, for a different location than the first two elements.

This dissertation, consisting of five chapters, is structured as follows. Chapter 2 is a reproduction of Rahman *et al.*, 2022, and presents the relative accuracy of two sets of wind/pressure fields for Hurricane Florence of 2018 that made landfall along the Carolinas and impacts on the storm surge simulation. Then Chapter 3 describes the effects of land surface controls on the intensity and locations of compound flooding caused by Hurricane Florence. Chapter 4 elucidates an understanding of the effects of various storm structures on the intensity of compound flooding. Finally, Chapter 5 presents a general conclusion and recommendations for future research.

Chapter 2 Relative Accuracy of HWRF Reanalysis and a Parametric Wind Model during the Landfall of Hurricane Florence and the Impacts on Storm Surge Simulations

Md Arifur Rahman, Yu Zhang, Lixin Lu, Saeed Moghimi, Kelin Hu, and Ali Abdolali

Rahman, M. A., Y. Zhang, L. Lu, S. Moghimi, K. Hu, and A. Abodolali, 2022. Relative Accuracy of HWRF Reanalysis and a Parametric Wind Model during the Landfall of Hurricane Florence and the Impacts on Storm Surge Simulations. Springer Netherlands. doi:10.1007/s11069-022-05702-3

ABSTRACT

Prediction and reanalysis of storm surges rely on wind and pressure fields from either parametric tropical cyclone wind models or numerical weather model reanalysis. Both are subject to significant errors during landfall. This study assesses two sets of wind/pressure fields for Hurricane Florence that made landfall along the Carolinas in September 2018 and appraises the impacts of differential structural errors in the two suites of modeled wind fields on the predictive accuracy of storm surge driven thereby. The first set was produced using Holland 2010 (H10), and the second set is the Hurricane Weather Research and Forecasting (HWRF) reanalysis created by the NWS National Centers for Environmental Prediction (NCEP). Each is validated using an extensive surface data set collected at public and commercial platforms. Then it is used as input forcing to a 2-D coastal hydrodynamic model (i.e., Delft3D Flexible Mesh) to produce storm surge along the Carolina coasts and major sounds. Major findings include the following. First, wind fields from HWRF are overall more accurate than those based on H10 for the storm's periphery, though they exhibit limitations in resolving high wind speeds near the center. Second, applying H10 to the best track data for Florence yields an erroneous spike in wind speed on September 15th, when the storm reduced to a tropical depression. Third, HWRF wind fields exhibit a progressively negative bias after landfall, likely due to deficiencies of the model in representing boundary layer processes and to the lack of assimilation of the surface product after landfall to compensate for these deficiencies. Fourth, using HWRF reanalysis as the forcings to Delft3D yields more accurate peak surges simulations, though there is a severe underestimation of surges along the shoreline close to the track center. The peak surge simulations by Delft3D are biased low when driven by H10, even though over several locations, the H10 model overpredicts surface wind speeds. This contrast highlights the importance of resolving wind fields further away from the center to reproduce storm surges and associated coastal flooding accurately.

Keywords: Hurricane, wind model, storm surge, reanalysis

2.1 INTRODUCTION

Flooding in the coastal areas caused by rainfall and storm surges imposes devastating effects on the lives, environments as well as the economy of nations across the globe. Improving the resilience of coastal communities requires accurate predictions of coastal flooding in general and storm surge in particular. Despite the recent advances in modeling and computational techniques, accurate representation and prediction of storm surges remain challenging. Hydrodynamic models are often unable to adequately reproduce patterns of coastal flooding both in space and time. The reasons are manifold. These include uncertainties in atmospheric forcing (Cardone and Cox, 2009; Dietrich *et al.*, 2018; Mayo and Lin, 2019; Abdolali *et al.*, 2021); a lack of available high-quality and high-resolution bathymetric data in shallow areas as well as insufficient grid resolution to resolve the topo-bathy in complex coastal regions (Hell *et al.*, 2012; Jacob and Stanev, 2021; Acosta-Morel *et al.*, 2021); a lack of available high-quality water level records during past tropical storms for model calibration (Asher *et al.*, 2019); under- or misrepresentations of physical processes pertaining to flow and to atmosphere-ocean momentum exchange under strong wind regime and in shallow waters (Olabarrieta *et al.*, 2012), a lack of coupling of different model components which have a direct effect on each other (i.e., atmospheric forcing, storm surge, wave, and hydrology; Ma et al., 2020; Santiago-Collazo *et al.*, 2019). Among these, abrupt changes in wind fields during landfall due to the increased drag have been recognized as a major source of errors in the simulation and prediction of wind fields by numeric weather models (Wang, 2012; Leroux *et al.*, 2018; Kim *et al.*, 2020), and these errors have been cited as a key impediment to accurate storm surge simulations for locations along estuaries and coastal streams further away from the coast (Ferreira *et al.*, 2014).

To date, post-analysis of storm surge and coastal risk assessment have often relied on parametric models of tropical cyclone (TC) wind and pressure fields constructed using semi-empirical relations (Mattocks and Forbes, 2008; Vickery *et al.*, 2009; Forbes *et al.*, 2010). These models incorporate idealized assumptions of tropical storm structures and boundary layer processes (Holland, 1980; Demaria *et al.*, 1992; Houston and Powell, 1994; Vickery *et al.*, 2000; Phadke *et al.*, 2003; Willoughby *et al.*, 2006; Zhang *et al.*, 2011; Chavas *et al.*, 2015; Kepert *et al.*, 2016), require only a few storm parameters and therefore simple to implement, and have the advantages of being able to integrate forecasted and observed TC track data directly. Among the contemporary parametric models, perhaps the most well-known is the model by Holland (1980) and its later variants (i.e., Holland, 2008 and Holland *et al.*, 2010), which now serve as the default forcing mechanism for coastal hydrodynamic models such as ADCIRC (Luettich *et al.*, 1992) and Delft3D (Deltares, 2014).

While these parametric wind models have been widely applied and, in many cases, yielded satisfactory storm surge simulations, several concerns remain. It is well known that these models are limited in their ability to resolve inter-storm variations in wind profiles, asymmetry in the storm structures, and changes of TC structures induced by enhanced friction drags during landfall (MacAfee and Pearson, 2006; Fang *et al.*, 2020). In addition, parametric models lack the ability to resolve background wind and pressure fields. These impair their ability to capture the waves, swells, and surges generated by wind and pressure at a longer distance from the TC center (Abdolali *et al.*, 2021). Though practitioners often resort to the calibration of hydrodynamic models as a countermeasure to compensate for biases and errors in forcings as well as deficiencies in model structures (Lin and Chavas, 2012), the efficacy of this practice, however, remains questionable.

Over recent years, high-resolution numerical weather prediction models (NWP) real-time or retrospective analyses of past landfalling TCs have become widely available, and these products have been increasingly applied in predicting/reconstructing storm surge events. Notable extant real-time analysis and reanalysis products include those from the Hurricane Weather Research and Forecasting (HWRF) model that is operational at the US National Weather Service (NWS; Ma et al. 2020), Hurricanes in a Multi-Scale Ocean-coupled Non-hydrostatic model (HMON) running operationally at NCEP, GFDL model, and HiRES from European Center for Medium-range Weather Forecast (ECMWF; Molteni *et al.*, 1996). These NWP models incorporate explicit representations of states of the atmosphere and their interactions with ocean and land, and have the ability to assimilate a variety of surface and remotely sensed observations. HWRF forecast, for example, is produced by assimilating Doppler velocity from ground-based or air-borne Doppler radar (Tong *et al.*, 2018; Lu and Wang, 2020; Davis *et al.*, 2021); upwelling microwave radiation measured by an airborne radiometer (Chen *et al.*, 2018), and dropsonde observations (Powell *et al.*, 2003; Franklin *et al.*, 2003; Ryan *et al.*, 2019). Owing to these strengths, these products are expected to offer physically more realistic depictions of TC wind and pressure fields during landfall than do those from parametric models. Nonetheless, the NWP models themselves are subject to biases and errors that arise from mis- or underrepresentation of processes. In particular, there have been reports of significant departures of HWRF wind analysis and prediction of TCs after landfall (Kloetzke, 2019; Ma *et al.*, 2020), which likely reflect inadequate representations of boundary layer processes.

Heretofore, a plethora of studies have been undertaken with the purpose of illuminating the evolution of TC wind structures (Chen *et al.*, 2012; Wang, 2012) over the ocean and during landfall, assessing the skills (Resio *et al.*, 2017; Annane *et al.*, 2018) of NWP models in prognosticating TC tracks and structures, and predicting storm surge (Leroux *et al.*, 2018; Bucci *et al.*, 2021). Yet, very few of these have attempted to appraise the relative realism of wind and pressure fields produced by parametric models versus those from parametric models prior to, during, and after landfall or to assess the impacts of structural errors in these products on the surge simulations driven thereby. A notable exception is Dietrich *et al.* (2018), in which the authors examined the storm surge forecasts forced by a parametric model and predictions from a WRF model for Hurricane Isaac. The study, however, did not delve into the differential structural errors in the wind profiles that led to the contrasting predictive accuracy of ADCIRC.

The present study is motivated by the need to determine the relative strengths as well as deficiencies of the parametric wind model and NWP reanalysis as forcings for storm surge simulations; it offers detailed, comparative analyses of wind and pressure fields from HWRF and the Holland (2010) wind model (henceforth referred to as H10) for Hurricane Florence, and the storm surge simulations driven by each. The specific objectives of the present study are twofold. The first is to determine the relative skill of H10 vs. HWRF in reproducing the evolution of wind and pressure fields of Florence during and after its landfall, with a focus on identifying distance and quadrant-dependent errors that can be related to the interactions between the storm and land. The second is to gauge the relative efficacy of the two forcing data sets in reproducing the inundation processes along the coast and major sounds. Hurricane Florence was chosen for the study for three reasons: 1) it is one of the most devastating landfall Hurricanes along the Carolinas in recent history; 2) it produced a storm surge that penetrated far upstream (>50 km), and speed and direction of wind over land may have strongly modulated the intensity of flooding along major sounds, and 3) a high-resolution HWRF reanalysis is available, so are a rich set of surface wind observations for validating the wind fields. Our working hypotheses include: a) the accuracy of wind fields from both H10 and HWRF reanalysis would deteriorate after landfall; b) the quality of the H10 wind fields would decline more drastically due to its lack of explicit accounting for the increase in friction drags; c) using HWRF reanalysis would yield more accurate storm surge simulations throughout the event.

The remainder of this paper is structured as follows. Section 2 provides descriptions of the methods, including the wind forcing (i.e., H10 and HWRF), selected hydrodynamic model (i.e., Delft3D-FM), model parameters and inputs, and validation matrices. The objectives of this study are accomplished in Section 3 (i.e., Results), where the relative accuracy of two wind forcings is assessed, and the impact of the storm surge simulations is determined. Section 4 discusses the findings of the study in detail, and Section 5 summarizes the findings and offers recommendations for future works.

2.2 MATERIALS AND METHODS

2.2.1 Hurricane Florence

According to NOAA's National Centers for Environmental Information (NCEI) and National Hurricane Center (NHC), Hurricane Florence of 2018 was by far one of the costliest (i.e., 12th) hurricanes that hit the mid-Atlantic region in recent history. The hurricane was first spotted as a tropical disturbance near Cape Verde Island off the West African coast in late August, experiencing rapid intensification in early September. It became a Category 4 hurricane around 5 September. The storm's strength then declined to a tropical storm while traversing the Atlantic Ocean until 11 September, when it intensified to a Category 1 hurricane. Florence made its first landfall south of Wrightsville Beach, NC, on 14 September while retaining Category 1 strength, even though wind speed was mainly below 70 mph while approaching the coast (Fig.2.1).

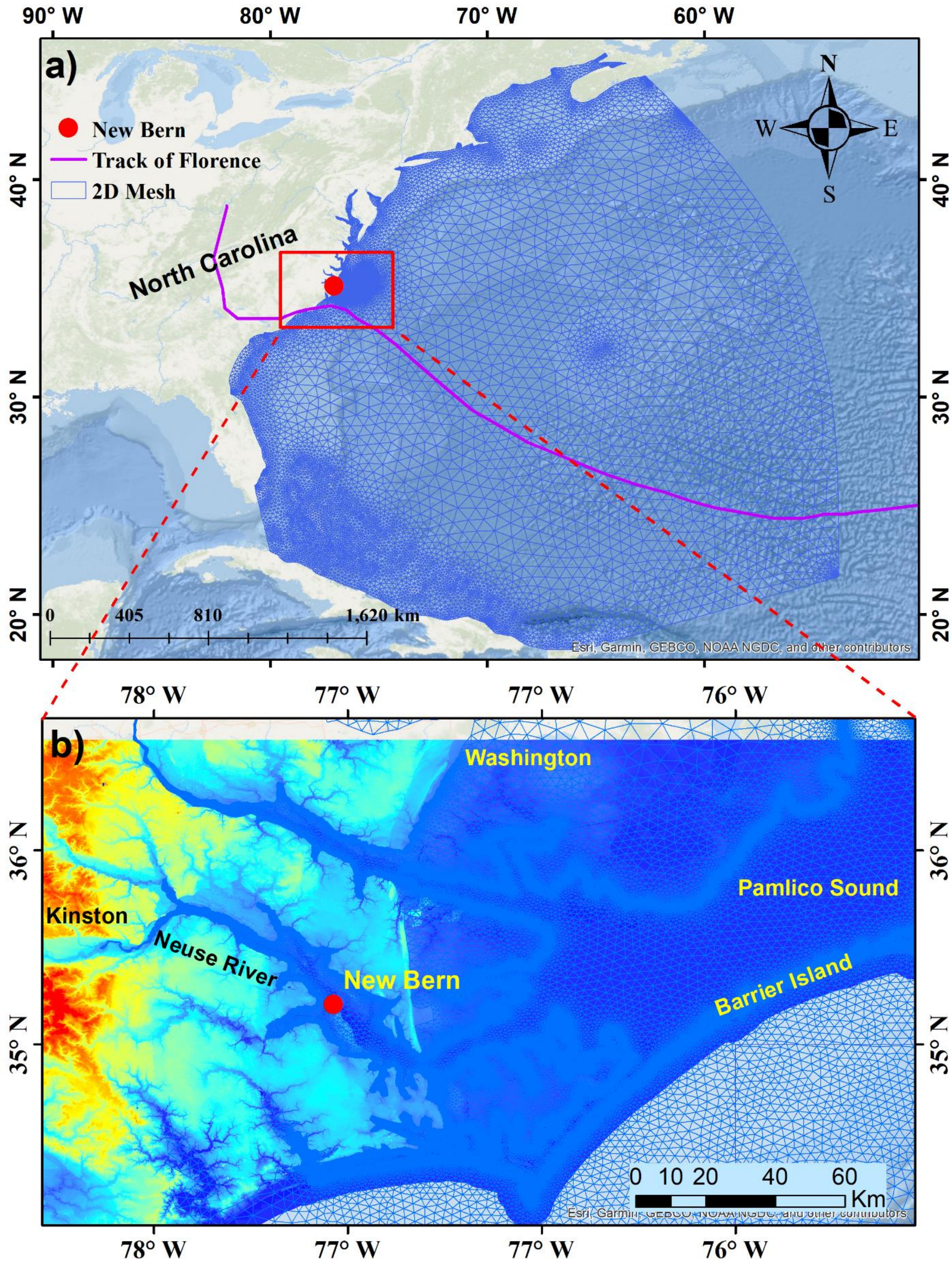

90° W
80° W
70° W
60° W
a)
New Bern
Track of Florence
2D Mesh
North Carolina
N
W
E
S
40° N
30° N
20° N
0
405
810
1,620 km
Esri, Garmin, GEBCO, NOAA NGDC, and other contributors
78° W
77° W
77° W
76° W
b)
Washington
36° N
35° N
Pamlico Sound
Kinston
Neuse River
New Bern
Barrier Island
0 10 20 40 60
Km
Esri, Garmin, GEBCO, NOAA NGDC, and other contributors

Fig. 2.1: Map showing Delft3D model domain and grid mesh (a) and a blow-up of the region that is the focus of the analysis on storm surge (b). Superimposed are the track of Hurricane Florence and the location of New Bern, which experienced severe flooding during the landfall of Florence

The storm produced sizable surges across the NC coast, penetrating as far as 50-60 km inland through major rivers. Along the Neuse River near the city of New Bern, the storm surge exceeded 3-m and caused widespread flooding across the city, which made the national headline. The major devastations by the storm were caused by its heavy rainfall - the maximum storm totals (up to 17 September) exceeded 900 mm in NC, shattering the previous record for the state. The storm degenerated into a depression on 15 September and underwent an extratropical transition on 17 September before dissipating on the 18th, though flooding in many locations lingered on till the end of the month (Stewart and Berg, 2019).

2.2.2 Wind Speed and Surface Pressure Fields

2.2.2.1 Reanalysis Product Based on Observation:

The Hurricane Weather Research and Forecast (HWRF) system tropical-storm predictions were by a consortium using the WRF Non-hydrostatic Mesoscale Model (WRF NMM; Janjic, 2004) core maintained by the NWS National Centers for Environmental Prediction (NCEP). First introduced to operation in 2007, it has become one of the primary forecasting models for TC predictions in the NWS. The HWRF uses telescopic nesting: in its current operational setting, the parent domain of HWRF spans approximately 77.2° × 77.2° with a ~27 km mesh, the intermediate domain ~17.8° × ~17.8° with a ~9 km mesh, and the innermost domain ~5.9° × ~5.9° with ~1.5 km mesh (Biswas *et al.*, 2018). The latest version has 75 vertical levels with a 10 hPa increment. HWRF runs are coupled with Princeton Ocean Model (MPIPOM-TC) for all oceanic basins in the northern hemisphere.

The HWRF model uses forecasts from the Global Forecast System (GFS) on the parent domain as lateral boundary conditions. In the forecast mode, it relies on a synthetic vortex to initialize a TC forecast (Biswas et al. 2018) and a bogus vortex to cold-start strong storms. The bogus vortex is created by smoothing the wind profile of the 2-D vortex until its maximum radial wind (RMW) matches the observed values. The HWRF uses a vortex relocation procedure in which a 6-h HWRF forecast from the previous cycle is used to determine the location of the vortex (Nadimpalli *et al.*, 2021), which infuses position, structure, and intensity from the National Hurricane Center (NHC) storm message (Leslie and Holland, 1995; Kwon and Cheong, 2010; Zou *et al.*, 2015; Biswas *et al.*, 2018; Zhang *et al.*, 2021). After identifying the vortex location, the initial conditions are further refined by assimilating a variety of observations, including those by Stepped Frequency Microwave Radiometer (SFMR; Uhlhorn and Nolan, 2012), airborne Doppler radar units, and dropsonde (Biswas *et al.*, 2018).

In this study, we acquired the HWRF reanalysis wind and pressure fields for Hurricane Florence (2018) created at the NCEP EMC that are available from 0600 UTC on September 09, 2018, through 1200 UTC on September 18, 2018, or 9 days. The reanalysis production involved retrospectively running the HWRF using the best track from NHC and assimilating the surface and remotely sensed products. The HWRF wind and pressure reanalysis are on a grid mesh of approximately 1.5 km at 1-h intervals.

2.2.2.2 Parametric Wind Model:

In this study, we adopted the Holland *et al.* (2010; referred to henceforth as H10) parametric pressure and wind model. H10 evolved from the original parametric model by Holland (1980, referred to henceforth as H80). In comparison to other contemporary analytical models (e.g., Emanuel, 2010; Emanuel and Rotunno, 2011; Chavas *et al.*, 2015), it has the advantages of structural simplicity, relying on few assumptions regarding the structure of the hurricane boundary layer, and being widely used and tested. For example, Holland et al. (2010) demonstrated that H10 outperforms Emanuel (2004) model in capturing the surface wind profile detected by aircraft reconnaissance. Lu *et al.* (2018) found that a parametric rainfall model based on H80, the predecessor of H10, better represents the rainfall fields for Hurricanes Isabel and Irene.

A brief review of the structure and evolution of the Holland models is provided here. The first Holland model, the H80, was formulated with the assumption that wind speed is invariant with height in the boundary layer (or the so-called slab model; Holland, 1980) and the surface pressure profile is approximated by a rectangular hyperbola (Schloemer, 1954). The model relies on the assumption of cyclostrophic balance to estimate the wind speed close to the eye and of gradient wind balance to derive the wind-pressure relations further away from the center. H80 uses two parameters, namely *a*, the scale parameter, and *b*, the shape parameter. It requires an input center and environmental pressure, maximum wind speed, and the radius of maximum wind speed, Holland (2008) replaces the fixed b parameter with a time-variant b_s that is estimated either from observed surface pressure and temperature when such observations are available or from pressure drop at the center, change in pressure, translation speed and latitude. The resulting model, referred to as H08, produces a wind profile directly at the surface without resorting to boundary-layer reduction relations (though in H80, the b parameter can be tuned to yield surface wind).

H08 further refines the model by introducing a radially variable exponent *x* to replace the constant ½ that arises from the cyclostrophic balance.

In the wind model of Holland (2010), herein denoted as H10, surface wind speed takes the following forms,

$$V_s = \left[\frac{100 b_s \Delta P_s \left(\frac{r_{v_{ms}}}{r}\right)^{b_s}}{\rho_s e^{\left(\frac{r_{v_m}}{r}\right)^{b_s}}} \right]^x \qquad (1)$$

Where ΔP_s is the pressure drop from a defined external pressure p_{ns} to the cyclone center P_{cs}, ρ_s is the surface air density, and e is the base of natural logarithms. The exponent b is a scaling parameter that defines the proportion of pressure gradient near the maximum wind radius. The equation can be rewritten as follows:

$$V_s = v_{ms} \left\{ \left(\frac{r_{v_{ms}}}{r}\right)^{b_s} e^{\left[1-\left(\frac{r_{v_{ms}}}{r}\right)^{b_s}\right]} \right\}^x \qquad (2)$$

where the subscript *s* refers to surface values at a nominal height of 10 m, v_{ms} denotes maximum wind speed (Vmax); r_{v_m} is the radius of maximum wind speed (RMW), and x is a scaling parameter that adjusts the profile shape. Parameter b_s is related to the original b by $b_s = b g_s^x$, where g_s is the reduction factor for gradient-to-surface winds.

The b_s parameter is estimated by following Holland (1980) using,

$$b_s = \frac{v^2{}_{ms} \rho_{ms} e}{100(P_{ns} - P_{cs})} \qquad (3)$$

In the absence of surface observations of pressure and temperature, b_s for a given radius range is expressed as a function of incremental variation in pressure along the radius, temporal change in central pressure, translation velocity, and latitude:

$$b_s = -4.4x10^{-5} \Delta P_s^2 + 0.01 \Delta P_s + 0.03 \frac{\partial P_{cs}}{\partial t} - 0.014\varphi + 0.15 v_t^x + 1.0 \qquad (4)$$

Where Δp_s in hPa, $\frac{\partial P_{cs}}{\partial t}$ is the intensity change in hPah^{-1}; φ is the absolute value of latitude in degrees; and v_t is the translation speed of cyclone in ms^{-1}.

The exponent x is related to incremental change in pressure.

$$x = 0.6\left(1 - \frac{\Delta P_s}{215}\right) \qquad (5)$$

And, the maximum wind speed is determined by surface pressure depression, vapor pressure and the revised Holland b_s parameter:

$$v_{ms} = \left(\frac{100 b_s}{\rho_{ms} e} \Delta P_s\right)^{0.5} \qquad (6)$$

H10 recommends blending in a secondary wind maximum that has often been observed in major hurricanes (Willoughby *et al.*, 1982; Wunsch and Didlake, 2018). However, the authors caution that a large perturbation may result in a change of vorticity gradient and lead to barotropic instability (Holland *et al.*, 2010). In order to avoid this instability, and out of the concern of uncertainties associated with respect to the locations and magnitude of the maxima, we chose not to implement the secondary maximum; instead, we adopted the central pressure–maximum wind relationship in this study that was described in Holland (2008), and our implementation uses radius for wind speeds of 34, 50, 64 and 100kts that are provided in the NHC Best Track (i.e., HURDAT2; Landsea et al., 2004).

2.2.3 Storm Surge Model

The Delft3D Flexible Mesh, also known as Delft3D-FM, is a fully integrated software suite by Deltares (2014), consisting of models that simulate a variety of processes in ocean, estuarine, tidal and inland streams, including those related to flow, sediment transport, morphodynamics, and water quality. Its hydrodynamic model, Delft3D-FLOW, is a finite-element model that uses an unstructured (triangular) grid mesh. Delft3D-FLOW allows for both 2- and 3-dimensional representations of flows. The 3-D, depth-resolving version solves the full incompressible, non-hydrostatic Reynolds-Averaged Navier-Stokes (RANS) equations (Kim *et al.*, 2016; Díaz-Carrasco *et al.*, 2021). The 2-D version solves the shallow-water equations. In this study, we implemented a 2-D version of the model for its computational efficiency, and our region of focus spans the Pamlico Sound and the Neuse River, where severe flooding was reported.

Many recent storm surge modeling efforts account for the impacts of near-shore waves, which have been shown to play major roles in amplifying the surge (Sheng *et al.*, 2010; Weaver and Slinn, 2005; Dietrich *et al.*, 2011; Abdolali et al., 2021). During the landfall of Hurricane Katrina, wave setup was shown to bring more than 0.5 m of additional surge along the lower Mississippi River Delta (Dietrich et al., 2010; Bunya et al., 2010). Over the study domain, however, we found the impacts of near-shore wave often muted due to the sheltering effects of the Barrier Island. As a result, we opted to exclude the modeling of near-shore wave (Ye, Huang, *et al.*, 2020).

2.2.3.1 Model Configuration:

Several high-quality bathymetric and topographic data for this study have been combined in implementing the Delft3D FM. The entire western North Atlantic Ocean was built using global SRTM15_PLUS bathymetry (Tozer *et al.*, 2019), while NCEI Bathymetric Digital Elevation Model (30-meter resolution) data has been utilized to enhance the representation of the bathymetry of the barrier island and Pamlico sound (Mulligan *et al.*, 2019). These data are merged to create an unstructured grid mesh that spans much of the west Atlantic – the model domain extends from latitude 34.0° N and longitude 78.0° W to latitude 36.5° N and longitude 72.0° W, and mesh resolution ranges from 2000-m offshore to 30-m near the shoreline and up along major sounds and tributaries (Fig.2.1).

The open water boundary, located in the deep ocean, was forced with tidal water level extracted from tidal model TPXO 9.0 (Egbert and Erofeeva, 2002), whereas the upstream river boundary, located at Barnwell in the vicinity of Neuse River, was forced with observed discharge time series from USGS. However, the initial condition was fixed at mean sea level (MSL). Space-varying wind forcing from HWRF and H10 models was applied to the entire model domain. The dependency of the drag coefficient on the wind speed was specified according to Smith and Banke (1975), where a linearly varying two breakpoints, at 0 m/s (i.e., C_d = 0.00063) and 100 m/s (i.e., C_d = 0.00723), were specified. The boundary smoothing time was fixed at 3600s for the numerical parameters, and the dry cell threshold was set to 0.01 m to satisfy the wetting and drying algorithm. Additionally, spatially varying bottom friction based on land use types, adopted from literature (Chow, 1959; Kaiser *et al.*, 2011), was defined using Manning's friction coefficients. In this study, the tide-generating force due to the earth's rotation was neglected as the model domain is not large enough to exhibit the Coriolis effect. However, the horizontal eddy viscosity (i.e., 0.2 m^2/s) and eddy diffusivity (i.e., 20 m^2/s) were assumed to be constant for the entire domain. The default values of all other model parameters were used for this study. The simulation time of the storm event (i.e., Florence) was set from 09 September 2018 00:00:00 to 18 September 2018 00:00:00 local time using a user-defined time step of 30 seconds with an initial time step of 1 second and a maximum time step of 600 seconds. However, due to the limitation of the time window in the wind forcing from HWRF, we used two days for the model spin-up. The model was simulated on a Linux cluster with 64 parallel processors, and the total clock time was around 8 hours. Finally, the history output data was saved at 5 minutes intervals, whereas the map outputs were saved at 3 hours intervals.

2.2.3.2 Atmospheric Forcing and Boundary Conditions

The Delft3D model requires atmospheric forcings, including surface wind, pressure, and tidal boundary conditions. As indicated earlier, in this study, we employ two sets of wind and pressure fields to drive the hydrodynamic model, one based on the H10 parametric model and the other on the HWRF reanalysis. We interpolate the zonal and meridional wind speeds (u and v, respectively), as well as surface pressure onto the Delft3D mesh using bilinear interpolation. As astronomical tide can be a crucial factor that contributes to coastal inundation during a storm event (Lai *et al.*, 2021), in this study, we use the output from TPXO 9.0 global tidal model (Egbert and Erofeeva, 2002) as an outer boundary condition for our Delft3D model. We used only 8 main constituents (i.e., m_2, s_2, n_2, k_2, k_1, o_1, p_1, and q_1) out of 37 to generate the tidal water level at the deep ocean.

2.2.3.3 Validation data sets

The wind and pressure fields from H10 and HWRF reanalysis will be validated against surface observations from five networks, namely National Data Buoy Center (NDBC) by NWS, National Water Level Observation Network (NWLON) managed by National Ocean Service, Advanced Surface Observation System (ASOS) by NWS, temporary and permanent gauging stations operated by USGS, and the network by Weatherflow Inc. The Weatherflow network consists of more than 100 stations near coastal urban areas, which are specifically designed to withstand the conditions of a landfalling hurricane with a less than 1% failure rate in surviving and recording winds up to 121 knots. The locations of these stations are shown in Fig. 2.2a, and the list of data sources is presented in Table 2.1.

Table 2.1: Collected required data set

Data Type	NDBC	COOPS	WF	ASOS	USGS	No. of stations
Wind	X	X	X	X	-	95
Pressure	-	X	-	-	X	100
Water Level	-	-	-	-	X	100

We collected water level series from NDBC, NWLON and USGS stations to validate storm surge simulations and high-water marks (HMWs) from USGS (Fig. 2.2b). These data sets were remapped to NAVD 88 in order to validate the Delft3D-FM simulated water levels. It is worth pointing out that a more extensive set of HMWs are available along the NC coasts, but only those along the lower reach of the Neuse River were used for validation because the Delft3D model grid mesh is sufficiently fine in this region (~ 100m).

Conventional metrics were employed for judging model performance, including percentage bias (PB), Pearson's correlation (R), and root mean squared error (RMSE). These metrics are defined as follows:

$$PB = \frac{\sum_{i=1}^{n}(Q_{sim,\mathrm{i}} - Q_{obs,i})}{\sum_{i=1}^{n} Q_{obs,i}} \times 100 \quad (7)$$

$$\mathrm{R} = \frac{\sum_{i=1}^{n}(Q_{obs,i} - \bar{Q}_{obs,i})(Q_{sim,i} - \bar{Q}_{sim,i})}{\sqrt{\sum_{i=1}^{n}(Q_{obs,i} - \bar{Q}_{obs,i})^2}\sqrt{\sum_{i=1}^{n}(Q_{sim,i} - \bar{Q}_{sim,i})^2}} \quad (8)$$

$$\mathrm{RMSE} = \sqrt{\frac{\sum_{i=1}^{n}(Q_{sim,i} - Q_{obs,i})^2}{n}} \quad (9)$$

where $Q_{obs,i}$ and $Q_{sim,i}$ are observed, and simulated datasets (i.e., wind speed, barometric pressure, or water level), respectively, and n is the number of records in the time series.

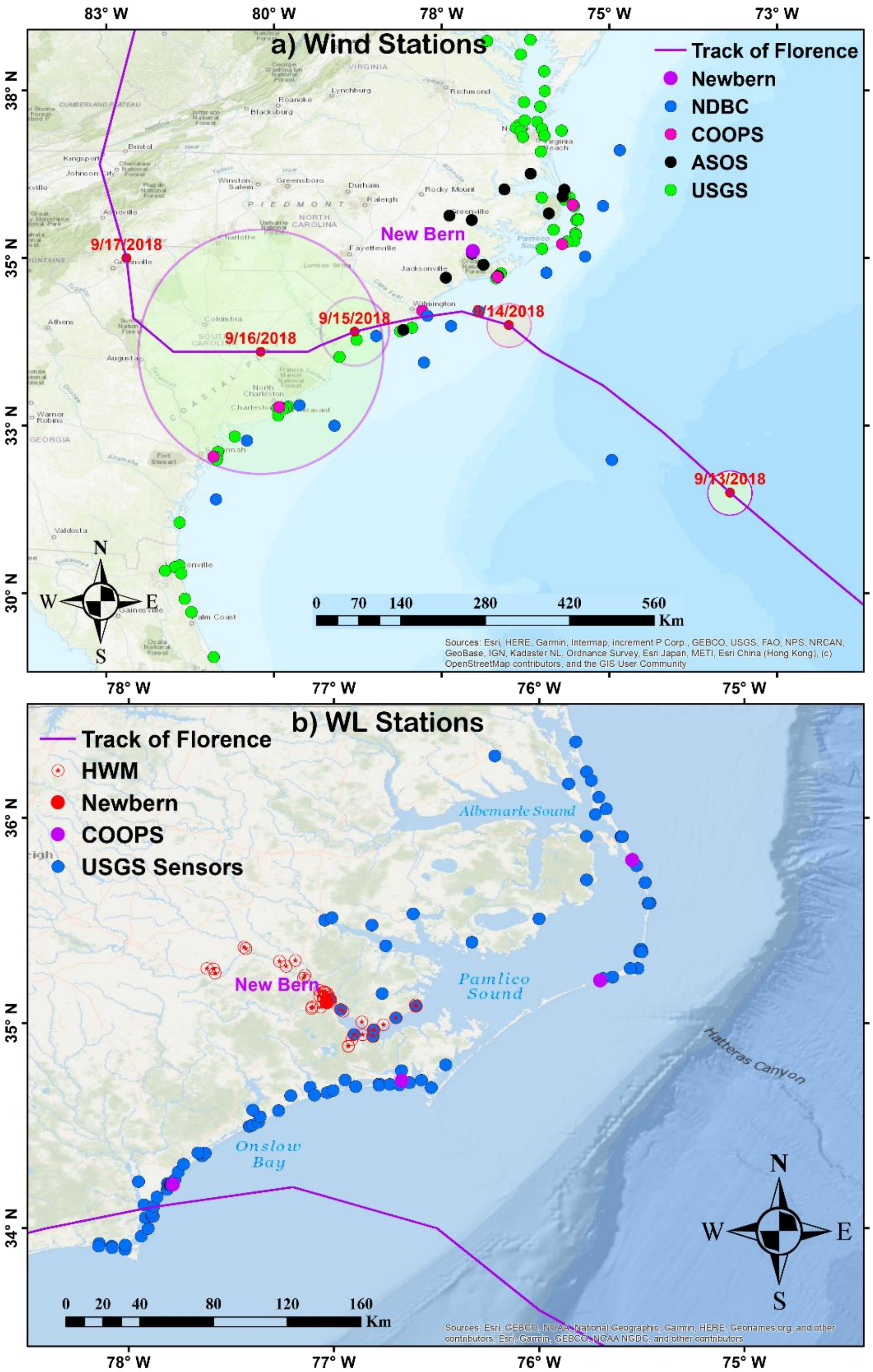

Fig. 2.2: Map showing locations of validation stations; a) wind observations, large circles represent the radius of maximum wind for selected synoptic hours during the landfall, and b) water level observations during Florence. Color legends identify networks associated with each station, which include NOAA's National Data Buoy Center (NDBC), Center for Operational Oceanographic Products and Services (COOPS), and Automated Surface Observing Systems (ASOS), United States Geological Survey stations,

and Weather Flow’s network. Hollow red circles on the lower panel represent locations of high-water marks.

2.3 RESULTS

2.3.1 Validation of Wind Speed and Pressure

The H10 and HWRF wind fields for Florence are first examined through the radial wind profiles for a 48-hour window surrounding the landfall that starts from 0z 14 September. Fig. 2.3 displays the NHC best track over the time window with the evolution of the radius of maximum wind (RMW) highlighted. It is evident that RMW increased slightly through the landfall (i.e., 37 km). Between 12 and 18z 15 September, RMW expanded greatly (i.e., 278 km), corresponding to the degeneration of the storm into a tropical depression.

Our examination will focus on the distribution of horizontal wind speed for each 6-h increment along the Southwest (225° azimuth) to Northeast (45° azimuth) transect (Fig. 2.3). Several authors (e.g., Hu et al., 2013) chose to analyze the distribution of wind speed along both southwest-northeast and northwest-southeast transects. We focus our attention on the former as it roughly aligns with the direction of the Carolina coastline; in particular, the wind intensity in the northeast quadrant (NEQ), which was directed towards the shore during the landfall, most likely had disproportionate impacts on the magnitude of storm surge. Fig. 2.4 displays the wind profiles from HWRF and H10 for each 6-h increment within the 48-h window. Superimposed in each panel are surface wind speed observations at stations that fall in the northeast and southwest (SWQ) quadrants (i.e., the quadrants that intersect with the transect). Prominent observations are summarized and briefly discussed below.

Prior to landfall, the wind speeds from both models exhibit symmetry with comparable Vmax in the NEQ and SWQ (Figs. 2.4a and b). The maximum wind speeds represented by H10 and HWRF

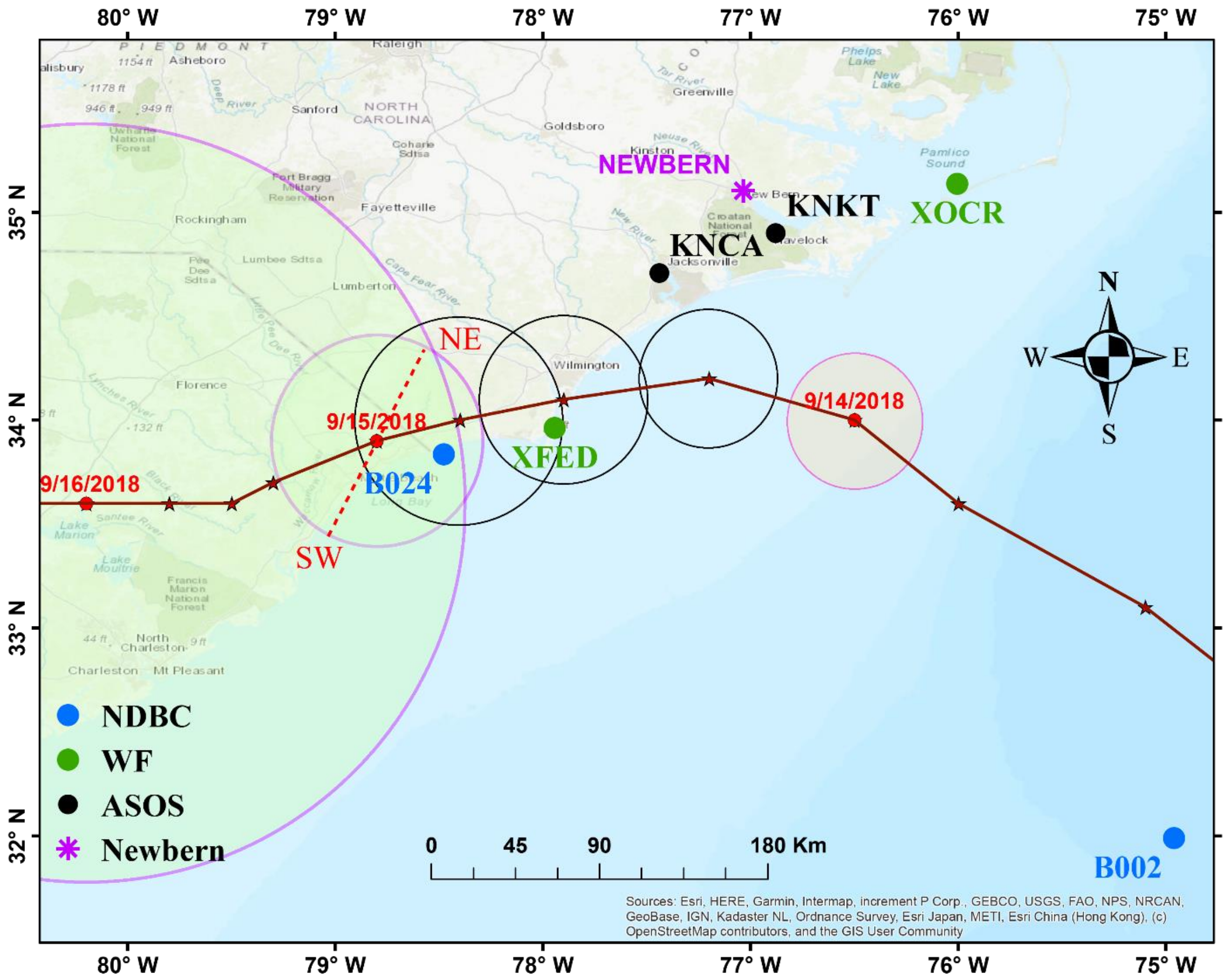

Fig. 2.3: Map showing stations for which the time series of wind speeds are used to validate the H10 and HWRF wind products. As in Fig. 2.2, circles represent the radius of maximum wind for selected synoptic hours during the landfall. The location of New Bern is highlighted in purple, and each star on the track of Florence represents 6-hr increments. The southwest to northeast transect is shown as a dotted line, and the plots for this direction are shown in Fig.2.4.

are close – though HWRF appears to produce slightly higher Vmax values than those supplied by the best track at 0z (Fig. 2.4a). In addition, the H10 wind profile declines at a faster rate with radial distance. At both 0 and 6z on 14 September (Figs. 2.4a and b), HWRF wind speed shows close agreement with surface observations for the NEQ, whereas the opposite is true for the SWQ (Figs. 2.4a and b). These suggest that the HWRF performs reasonably well in reproducing the easterly wind that blew towards the land but somehow exaggerated the land-bound westerly. By contrast, H10 underestimates the wind speed in NEQ and this bias is more pronounced further away from the storm's center.

On 06z September 14 (Fig. 2.4b), a secondary maximum emerges in the NEQ at about 120km from the center. Right at landfall (12z on 14 September), HWRF wind maxima in both quadrants broadly exceed the Vmax from NHC best track. In the NEQ, HWRF wind profile is in close agreement with observations at a further distance (> 120 km) from the center of the storm, whereas it is mostly above observations in the SWQ, echoing the observations in the preceding time step. H10 underestimates the wind in both quadrants compared to observations.

Florence made landfall on 12z September 14 (Fig. 2.4c). Perhaps the most notable feature during this time is that HWRF grossly overestimated the Vmax over both quadrants (i.e., NEQ and SWQ). The HWRF Vmax values over the two quadrants at this hour approach 80 knots, whereas the NHC estimates are about 60 knots. Again, further away from the storm's center, the HWRF wind profile appears to be accurate in the NEQ but is biased high in the SWQ. By contrast, the H10 wind remains negatively biased across the transect.

After landfall, HWRF wind speed weakens rapidly over NEQ, with Vmax declining from 75 to less than 40 knots between 12z and 18z on 14 September. Meanwhile, HWRF-based Vmax for the SWQ shows a relatively minor reduction (from 80 to 65 knots), and closely follows the observations. This results in a sharp asymmetry in the HWRF wind profile. At 18z on 14 September, HWRF wind speed generally agrees with the observations along the transect. Whereas H10 wind speed shows clear, negative bias outside the RMW that tends to be increasingly severer at a further distance to the center of the storm (i.e., > 200 km).

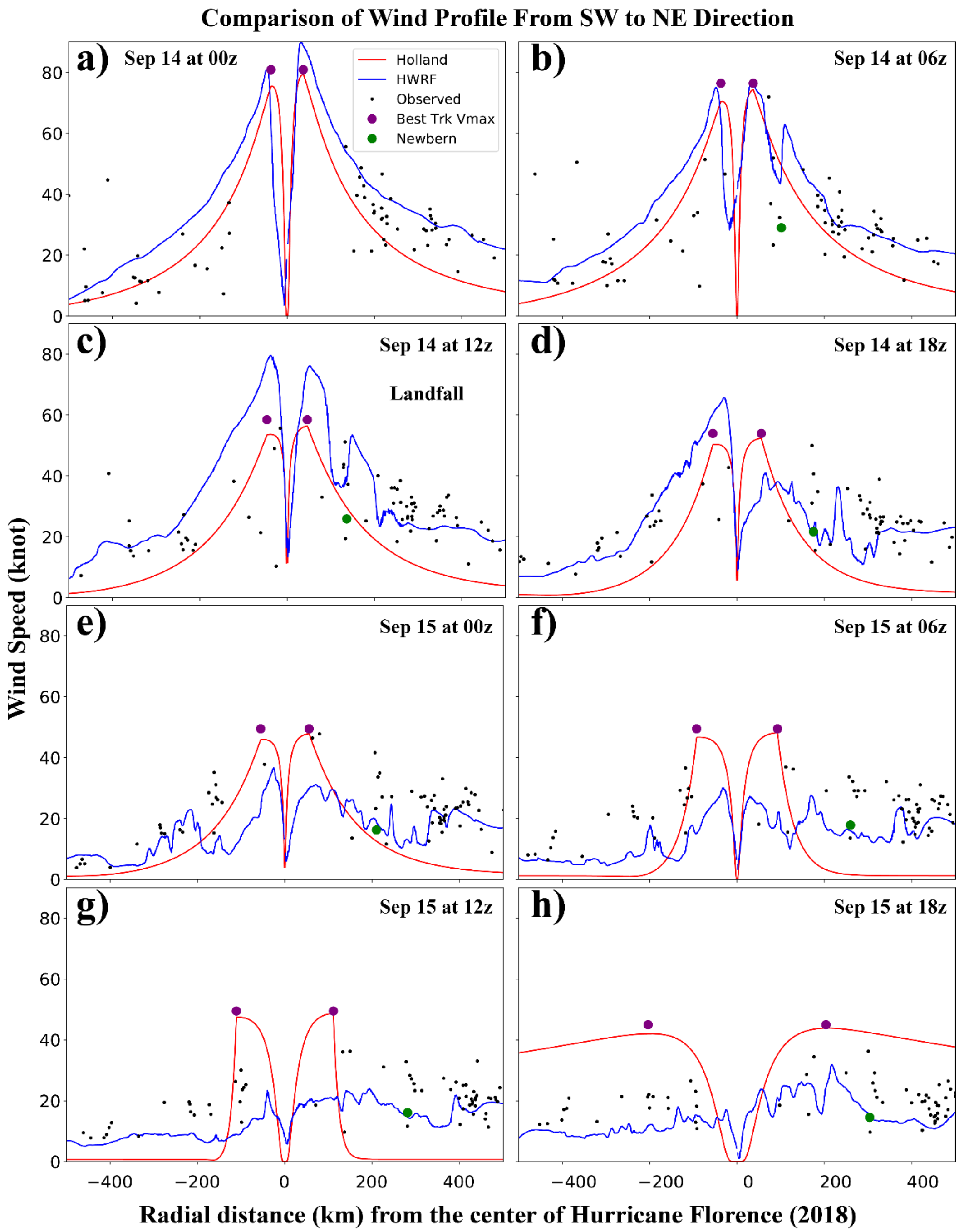

Fig. 2.4: Validation of radial wind profiles along the azimuth angles of 45° (northeast) and 225° (southwest) produced by HWRF and H10 against surface observations (i.e., black dots) over the time window surrounding the landfall of Florence (from 0z on 14 September to 18z on 15 September). Left to the right represents the southwest to northeast direction, as shown in Fig.2.3 as a dotted line. Note the surface observations are sampled from stations with the quadrants in which each radial direction is

embedded. Here the purple circles represent V_{max} of best track data, and the green circle represents wind speed at New Bern.

The relative performance of H10 and HWRF for three subsequent snapshots (0, 6, and 12z on September 15) broadly resembles that at 18z on September 14, except that the HWRF profile appears to be mostly below the observed in both quadrants (Figs. 2.4e, f and g). H10 wind speed appears more consistent with observations within the RMW, but it declines sharply to near zero after 100km, leading to a conspicuous underrepresentation of wind speed beyond RMW. This decline can be partially attributed to the lack of representation of background wind in the H10 model. Between 12 and 18z on September 15, RMW expanded abruptly as a result of dissipating storm intensity. On 18z, H10 wind speed is broadly higher than the observations across the entire transect, and it exhibits a curious slow rate of decline with radius. By contrast, HWRF wind speed more closely matches the observations for this hour, though it appears to be consistently lower than the latter across distance.

We compare the surface pressure profiles from the two models to diagnose factors underlying the differential accuracy of wind profiles as represented by HWRF and H10. Figs.2.5a-h show the pressure profile along the NW-SE transect for the same time instants used in the wind analysis shown in Fig.2.4. Broadly speaking, HWRF surface pressure matches closely with the observations throughout the 48-h window. By contrast, H10 pressure tends to be biased low further away from the pressure center, presumably because its specification of ambient pressure is much lower than the observed. In addition, H10 produces a conspicuously lower central pressure at the center relative to HWRF from 6z to 12z on 15 September. As H10 uses the center pressure from the best track directly, it is clear that HWRF was unable to resolve the pressure drop fully. Another notable observation is that the HWRF pressure profile at the last instant (18z on 15 September) is consistently higher than the observations (Fig. 2.5h). This feature corresponds to, and is most likely causatively related to, the systematically lower wind speed simulated by HWRF shown in Fig. 2.4h.

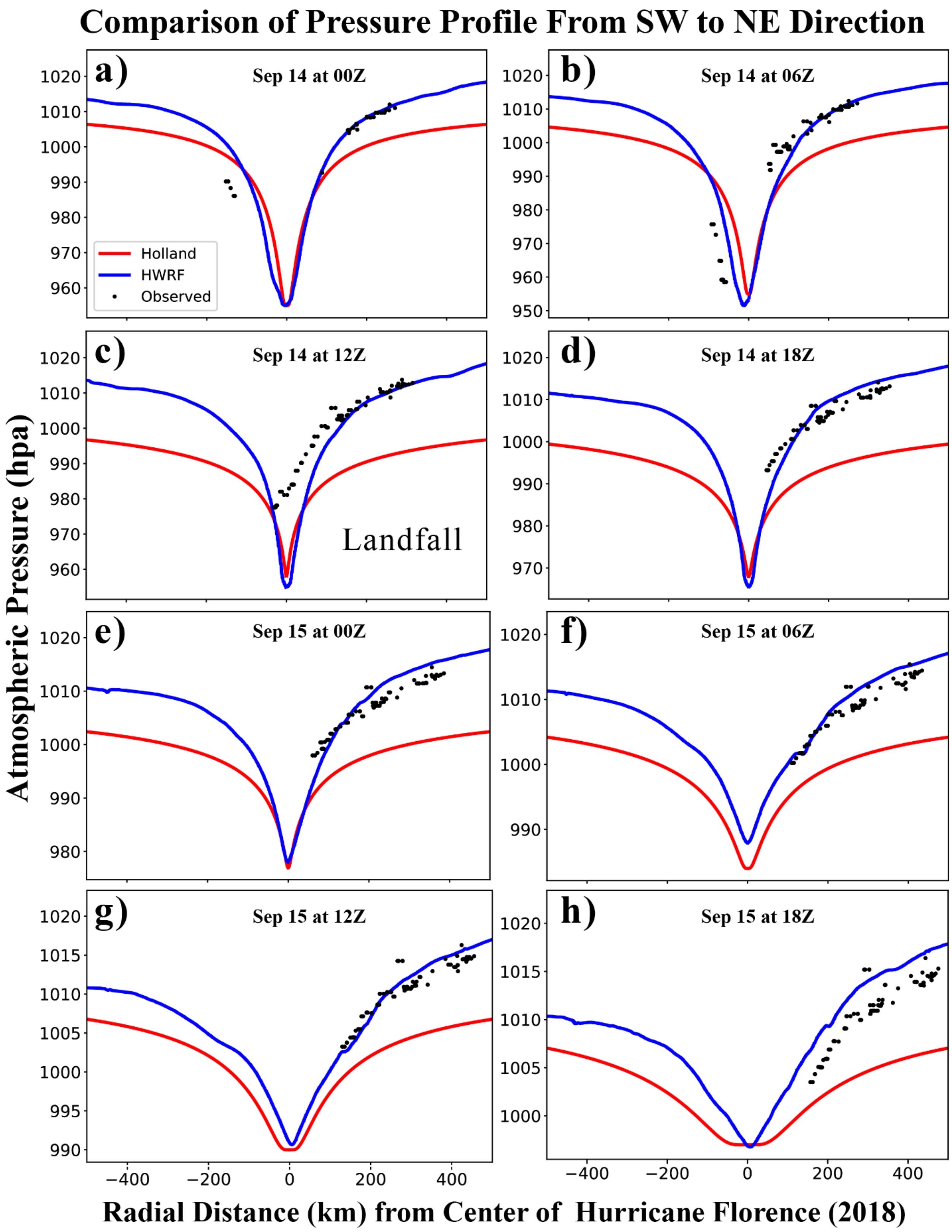

Fig. 2.5: As in Fig. 2.4, except for profiles of surface pressure.

It appears that Florence's intensity declined at a somewhat slower rate on the 15th than what was predicted by HWRF. The performance statistics are presented in tabular form in the appendix. To further assess the accuracy of the two sets of wind fields from the two models as the storm progressed, we compare the two wind speed time series against in situ observations at 6 stations close to the track (Fig. 2.3). Among these stations, B002 and B024 are offshore NDBC stations: B002 is further away from the shore whereas B024 is located near shore and close to the track. XFED and XOCR are Weatherflow stations situated along the shore, and the former is located at the site of landfall. KNKT and KNCA are ASOS stations in Cherry Point and Jacksonville, NC, respectively, and both stations are 10-15km inland. Note that KNKT is situated near the Neuse River downstream of New Bern, where severe flooding was reported. The time series are shown in Figs. 2.6a-f. The validation statistics are presented in Table 2.2.

Table 2.2: Validation statistics of hourly wind speed at selected NDBC, WF, and ASOS stations

Source	Station ID	RMSE (knot)		Correlation Coefficient (R)		% Bias	
		HWRF	H10	HWRF	H10	HWRF	H10
NDBC	B002	4.45	10.26	0.97	0.73	-15	-25
	B024	8.11	7.83	0.93	0.93	-25	-22
WF	XFED	9.93	10.41	0.83	0.71	-18	-13
	XOCR	4.0	16.48	0.98	0.28	-10	-25
ASOS	KNCA	7.83	14.36	0.89	0.57	-19	-7
	KNKT	7.91	10.13	0.84	0.81	47	68

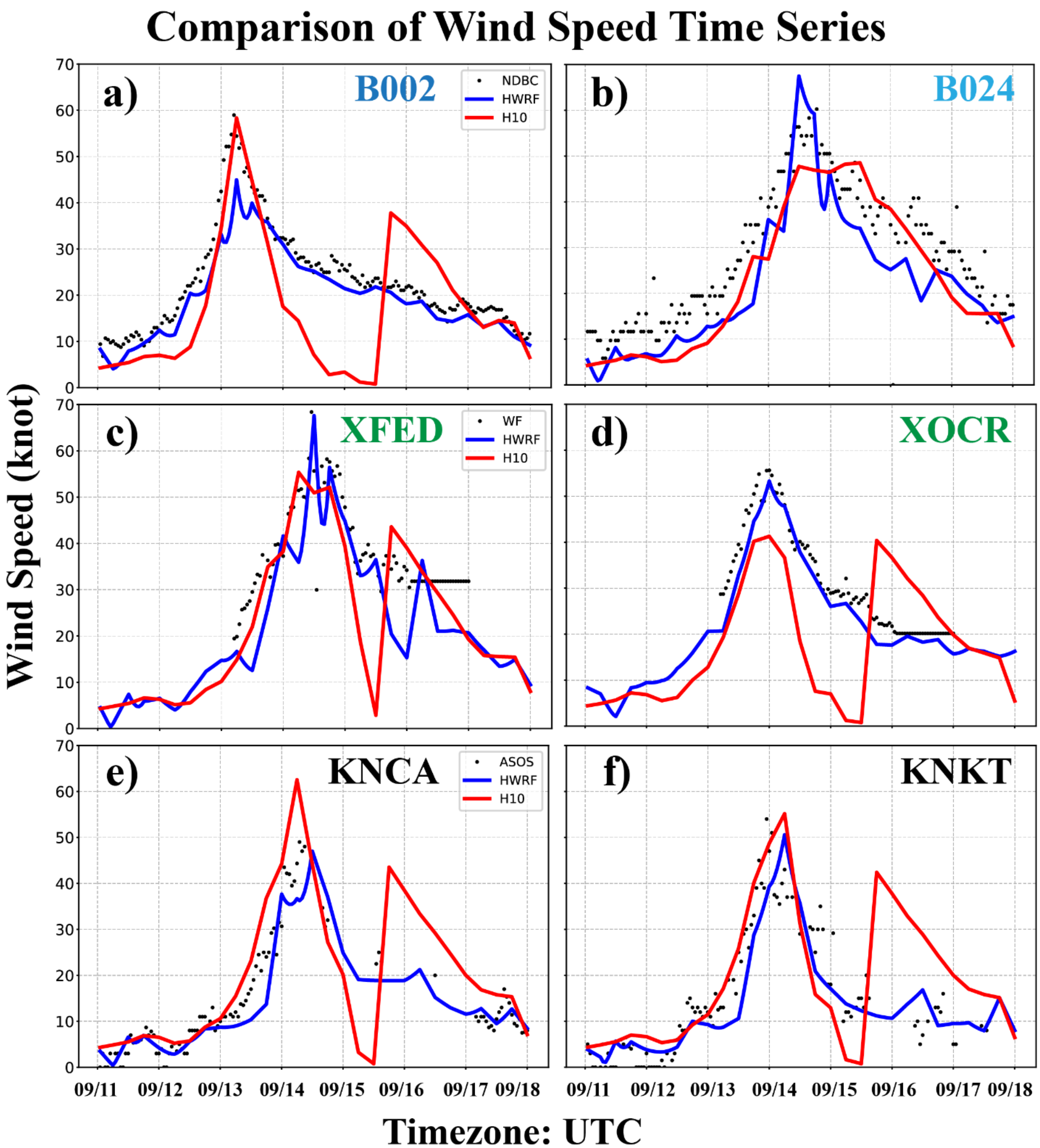

Fig. 2.6: Validation of wind speed time series produced by H10 and HWRF model. Shown in the first, second, and third rows are time series at two NDBC buoy stations offshore (a and b), two Weather Flow (WF) stations located on land along the coast, and two ASOS stations situated further inland.

For B002, the most striking feature is that H10 produces a sizable secondary peak on 18z of 15 September 15 that is not observed by the majority of the stations (Fig. 2.6a). This is apparently a result of H10's inability to accurately represent the wind structure during and after the decay of the storm into a depression. As shown in Fig. 2.4h, when the storm reduces to a depression, wind speed produced by H10 declines at a much slower rate with radius than in previous hours, and this results in a sharp, artificial expansion of the region with high wind speed that translates to a secondary wind peak over the periphery of the storm. By contrast, HWRF wind closely tracks the observed time series, though it exhibits a persistent negative bias that is the most pronounced around the peak time. At B024, the station near the track, this secondary peak is absent in the time series of H10 wind speed, and H10 underrepresents the peak wind speed (Fig. 2.6b). HWRF accurately reproduced the peak, but it exhibited a negative bias during both the rising and falling limbs of the series.

Over the two Weatherflow stations (XFED and XOCR, Figs. 2.6c and d), the bogus secondary maximum is again evident in the H10 wind series. In addition, at both sites, H10 tends to underrepresent the maximum wind speed during landfall. HWRF outperforms H10 at both sites, though there is a slight negative bias at XOCR (Fig. 2.6d). For the two ASOS stations in the north (KNCA and KNKT; Figs. 2.6e and f), H10 conspicuously overrepresents the peak wind speed at KNCA, whereas at KNKT, it accurately captures the peak. Once again, at both sites, the bogus secondary peak is present, and the outperformance of HWRF is evident.

Fig. 2.7 shows the correlation coefficients of H10 and HWRF wind fields against surface observations for each individual station. Note that the HWRF reanalysis was on a 6-h resolution and was first interpolated into hourly intervals prior to computing the correlation. For H10, the correlation contrasts sharply between stations situated to the north and south of the tracks. For the stations in the north, the correlation is broadly poorer (<0.4), with only a few stations close to the track exhibiting values higher than 0.5. By comparison, a cluster of stations to the south of the track exhibit good correlation – almost all of these stations are located in the vicinity of the track. Further away to the south, the correlation declines sharply. For HWRF, the correlation is generally good for a majority of stations, though it tends to be relatively low for a cluster of stations further north along the Chesapeake Bay.

The bias in the peak wind speed, as represented by the two wind data sets at each station, is shown in Fig. 2.8. On both sides of the track, the peak wind speed from H10 is positively biased for a majority of stations further away from the track; whereas close to the track, it is negatively biased or neutral for a slight majority of stations. The negative bias near the track is attributable to the fast decline in the H10 wind speed away from the center, which makes it unable to reproduce the peak wind speed at the stations at a moderate distance from the track. By contrast, the positive bias for the far-away stations is related to the artificial increase in wind speeds, as featured in H10 after the storm reduced to a depression. To elaborate, the observed peak wind speeds during Florence's landfall were weak at these stations, so were the coincidental wind speeds from H10. For H10, the

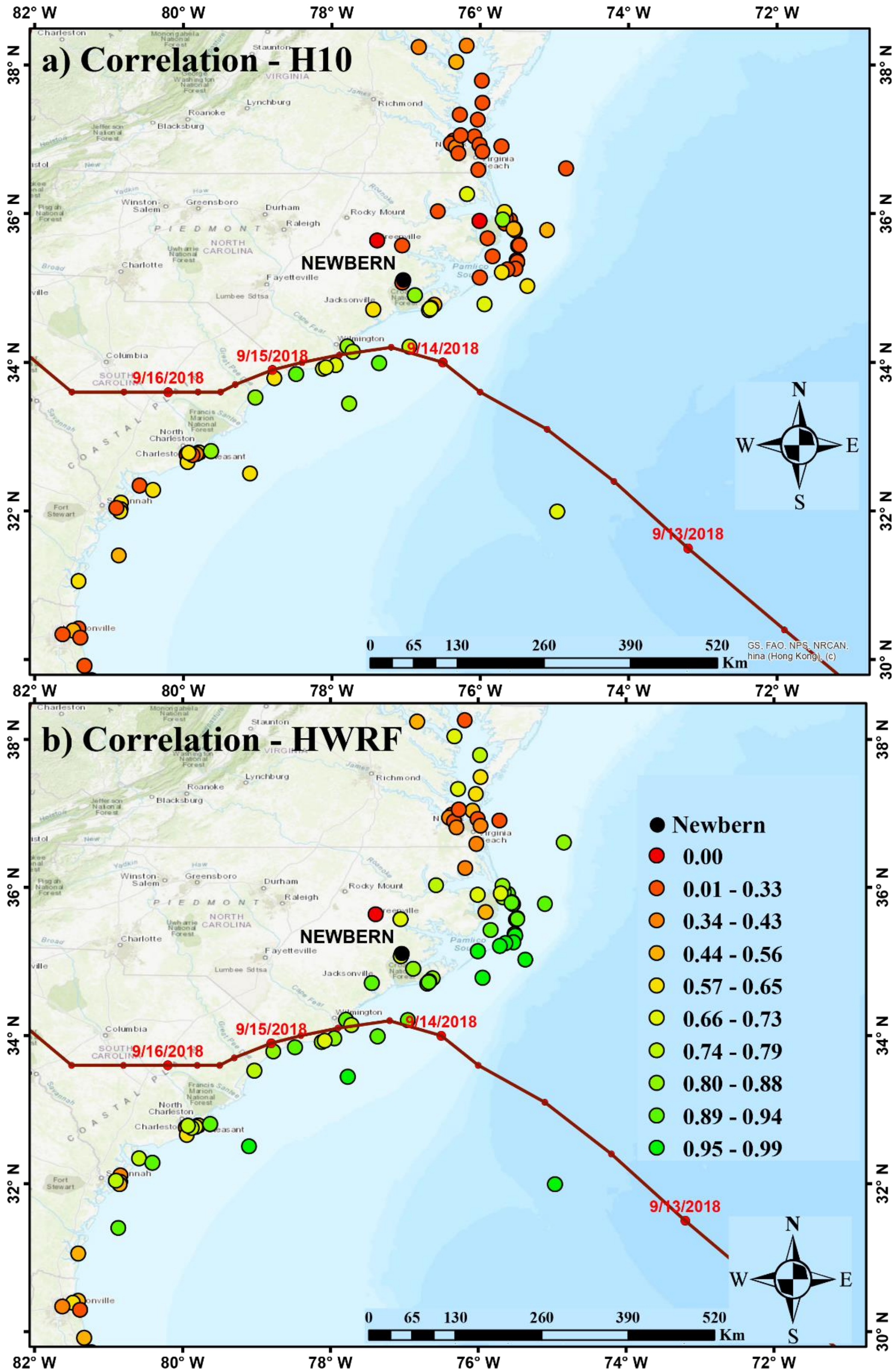
a) Correlation - H10
b) Correlation - HWRF
NEWBERN
9/13/2018
9/14/2018
9/15/2018
9/16/2018
Newbern
0.00
0.01 - 0.33
0.34 - 0.43
0.44 - 0.56
0.57 - 0.65
0.66 - 0.73
0.74 - 0.79
0.80 - 0.88
0.89 - 0.94
0.95 - 0.99
82° W
80° W
78° W
76° W
74° W
72° W
38° N
36° N
34° N
32° N
30° N
0 65 130 260 390 520 Km
N
S
E
W

Fig. 2.7: Spatial distribution of correlation between model (H10 or HWRF) and observed wind speed series at the locations of surface stations for H10 (a), and HWRF (b). The track of Florence is superimposed.

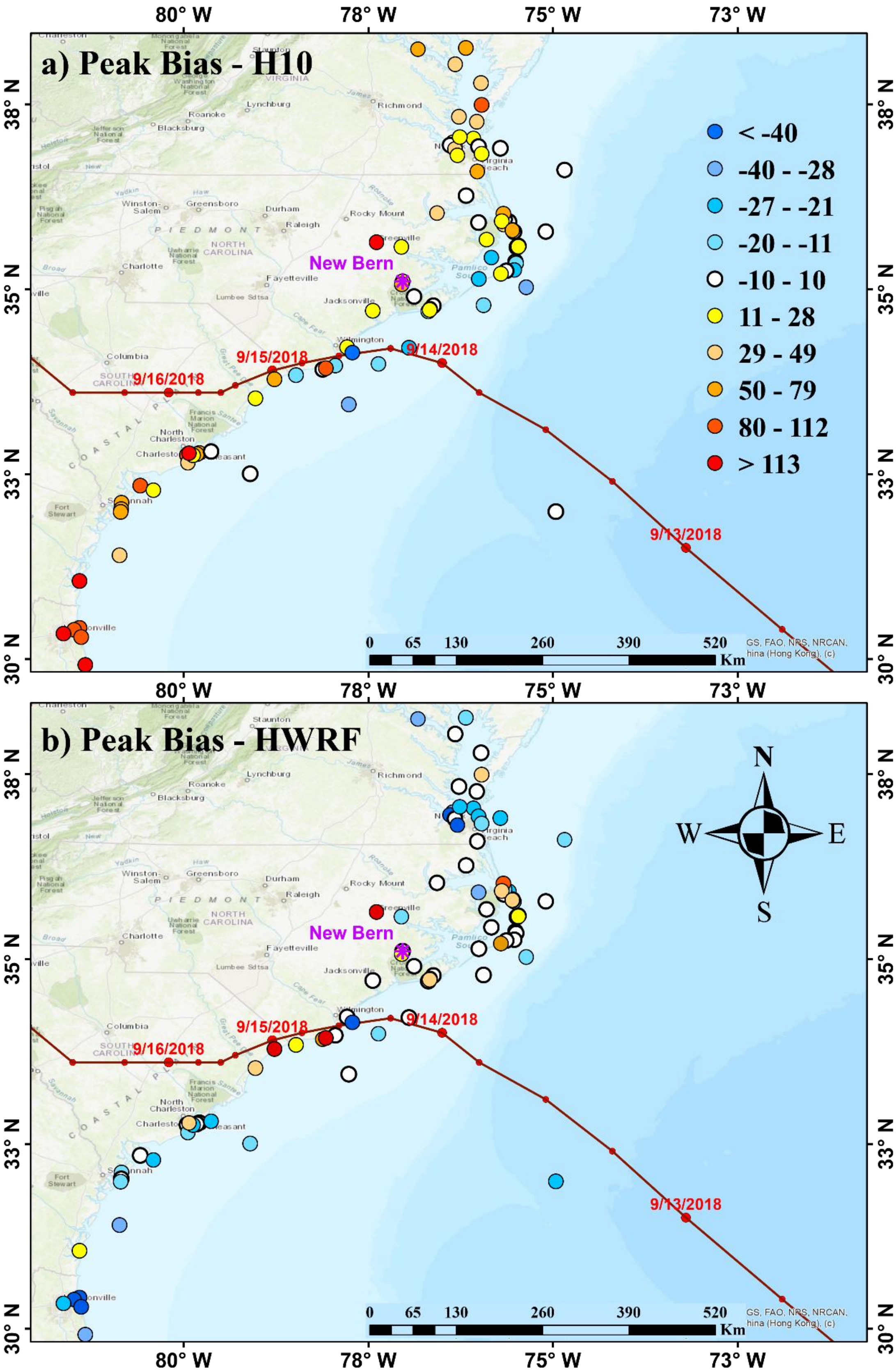

a) Peak Bias - H10
b) Peak Bias - HWRF
< -40
-40 - -28
-27 - -21
-20 - -11
-10 - 10
11 - 28
29 - 49
50 - 79
80 - 112
> 113
New Bern
9/13/2018
9/14/2018
9/15/2018
9/16/2018
80° W
78° W
75° W
73° W
38° N
35° N
33° N
30° N
0
65
130
260
390
520
Km
N
S
E
W

Fig. 2.8: As in Fig. 2.7 expect for percentage peak bias.

peak wind speeds actually arrived later in the series during the depression phase of the storms, and these values were broadly higher than the observed, leading to the positive bias.

The bias in the HWRF peak wind also varies widely among stations. Relative to H10, the HWRF product is nearly bias-neutral for a significant number of stations to the north of the track. For the remaining stations, the bias is mixed: there are a few stations along the NC coast where the bias is clearly positive. To the south of the track, the bias becomes overall negative further away from the track.

2.3.2 Comparison of Simulated Water Level and Inundation Extent

The Delft3D storm surge simulations using wind and pressure fields from H10 and HWRF reanalysis are first validated against in situ observations. Two validation stations located to the north of the track are selected for this purpose (Fig. 2.9). The first one is a COOPS station (ID 8658163) situated offshore of Wrightsville Beach, NC (Table 2.3), and the second is a temporary USGS gauge placed in the Neuse River near New Bern (Table 2.4). Note that there are several other COOPS stations with water level records during the event, but these are not used as their locations are either too far away from the storm center or over areas shielded from storm surges.

Figs. 2.10 and 2.11 show the comparisons of simulated vs. observed water level time series at two stations, with the summary statistics shown in Tables 2.3 and 2.4. For reference, the wind time series are shown alongside the water level series in each plot. At the Wrightsville Beach station, as indicated earlier, the HWRF wind series features two sharp drop-offs that are not consistent with the observations (Fig. 2.10a). Florence produced a small surge around 18UTC on the 14th, with the maximum water level reaching 2m (Fig. 2.10b). Delft3D simulation driven by HWRF yields a surge on the same day but 12 hours earlier, and the maximum water level in the subsequent tidal cycle declined.

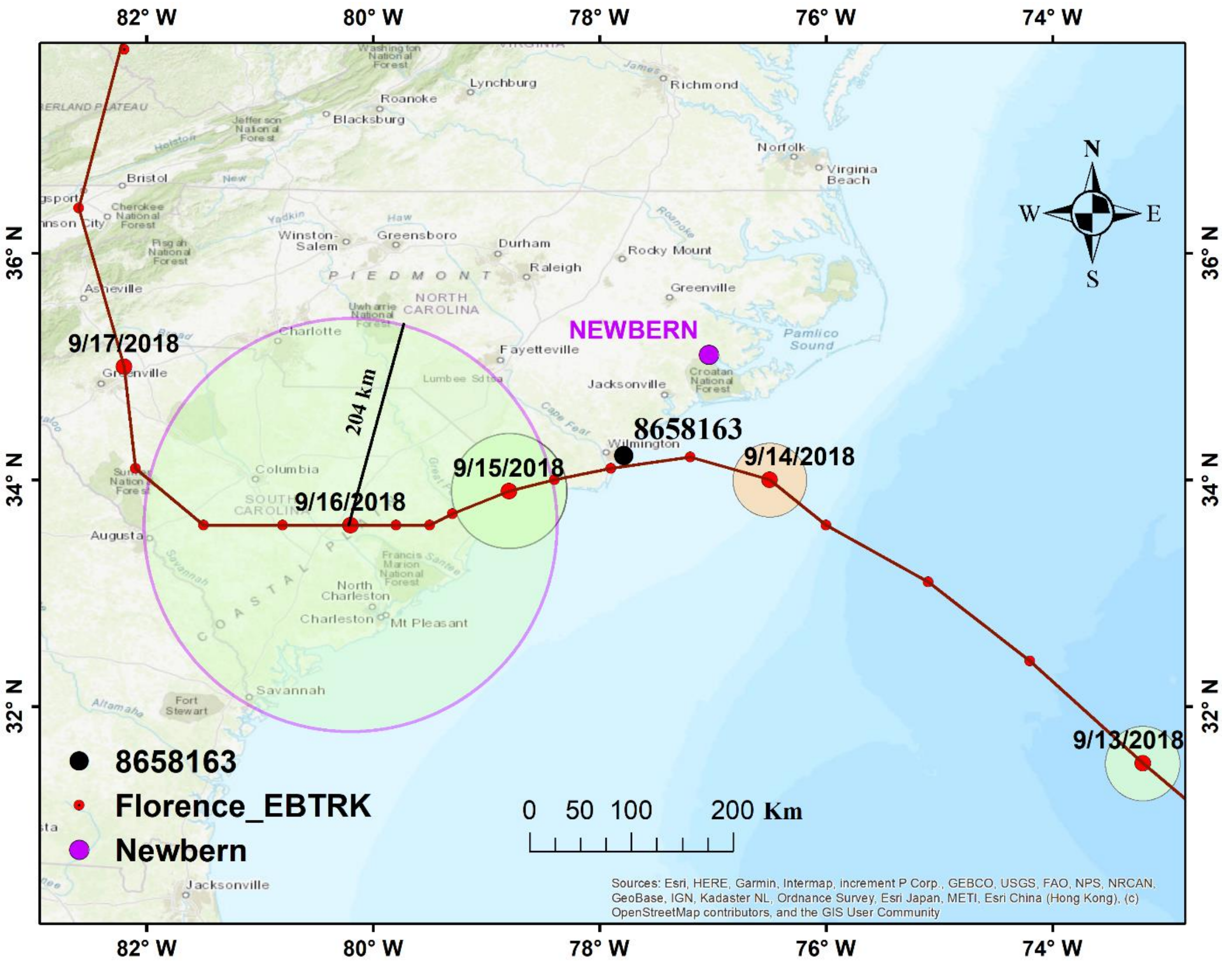

Fig. 2.9: Map showing locations of wind and water level validation stations for the time series analysis; the circles represent the radius at maximum wind speed; black dot represents COOPS (i.e., 8658163), and USGS (i.e., 02092576) stations. Superimposed are the track of Florence and radius of maximum wind at 0z of 14, 15 and 16 of September.

to normal level (~ 1m). By contrast, using H10 as the forcing results in a slightly more accurate water level series on the 14^{th} than that produced by HWRF: the simulated surge level near 6 UTC remains positively biased but is slightly lower than that by HWRF, and the peak surge level near 18 UTC is much closer to the observed. Another noticeable difference is that using H10 leads to depressed ebb levels throughout the time window, whereas HWRF-driven simulation largely resolves the tidal cycles. The inability of the HWRF-driven simulation to reproduce the peak water level, as we surmise, is a consequence of the fast decline in HWRF wind on the 14th, which was associated with the passage of the eye (Fig. 2.9).

Table 2.3: Validation statistics of hourly wind speed and water level at COOPS Stations

Stations	Metrics	Wind Speed		Water Level	
		HWRF	H10	HWRF	H10
8658163	RMSE	6.29 (knot)	8.65 (knot)	0.46 (m)	0.63 (m)
	R	0.90	0.84	0.76	0.80
	Pbias	-14	-4	-22	-62

At the USGS station near New Bern, the contrasts between H10 and HWRF wind series are stark, broadly echoing that shown earlier in Fig. 2.6. H10 produces an earlier rise in wind speed, overpredicts the peak wind, and features a sharp drop-off to 15 September. As shown earlier in Fig. 2.6, the H10 wind series features a bogus secondary peak on the 15th that is related to the rapid expansion in the RMV during the weakening of Florence to a depression. On the other hand, the HWRF wind series closely track the observations, though it features a secondary peak about 12 hours following the primary one. The simulated water level series driven by H10 lags slightly behind that of the observed, and, somewhat paradoxically, the peak level is visibly lower than the observed despite the higher wind speeds during the landfall over the location, as featured by H10. By comparison, those forced by HWRF are closely correlated with the observations, and the peak surge is nearly perfectly captured by the model. In addition, in the H10-driven simulations, the bogus secondary wind peak on 15 September translates to a distinctive bogus spike in water level.

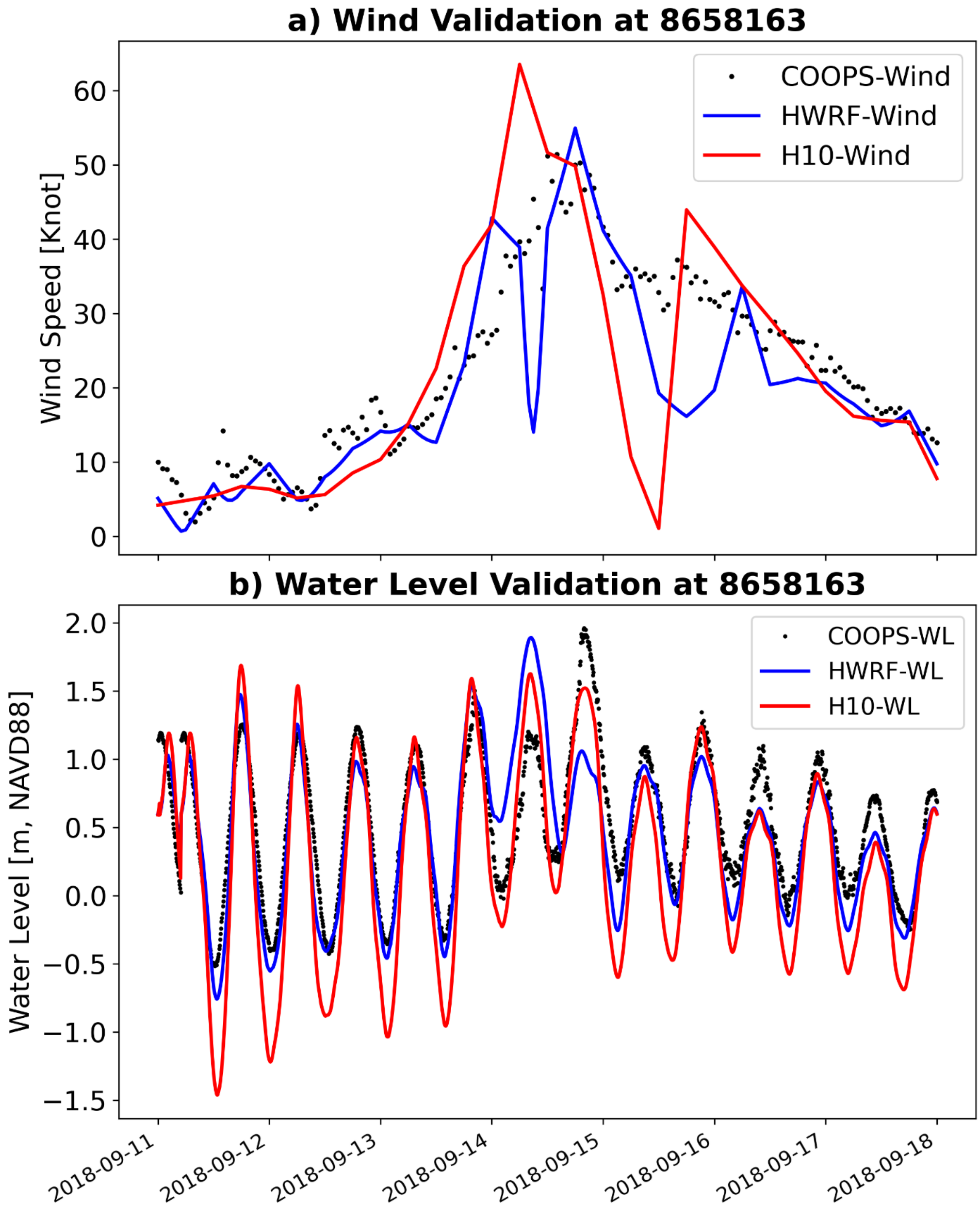

Fig. 2.10: Wind and water level times series at COOPS station 8658163 (Wrightsville Beach, NC) that is located close to the track: a) surface wind speed from H10, HWRF and surface station, and b) water levels produced by Delft-3D simulations driven by H10 and HWRF along with the observations.

Table 2.4: Validation statistics of hourly wind speed and water level at USGS station located near New Bern

Metrics	Wind Speed		Water Level	
	HWRF	H10	HWRF	H10
RMSE	4.20 (knot)	13.72 (knot)	0.21 (m)	0.40 (m)
R	0.89	0.79	0.96	0.90
Pbias	8	79	-6	-25

The summary validation statistics, including bias, correlation, and RMSE, all point to the broad outperformance of HWRF wind fields over both locations, but the impacts on water level vary (Tables 2.3 and 2.4). For the Wrightsville Beach station, H10 performs better in terms of correlation but worse, as indicated by RMSE (Table 2.3). This difference reflects the lower ebb levels seen in Fig. 2.10. For the New Bern station, HWRF-related wind and water series outperform by a wide margin (Table 2.4).

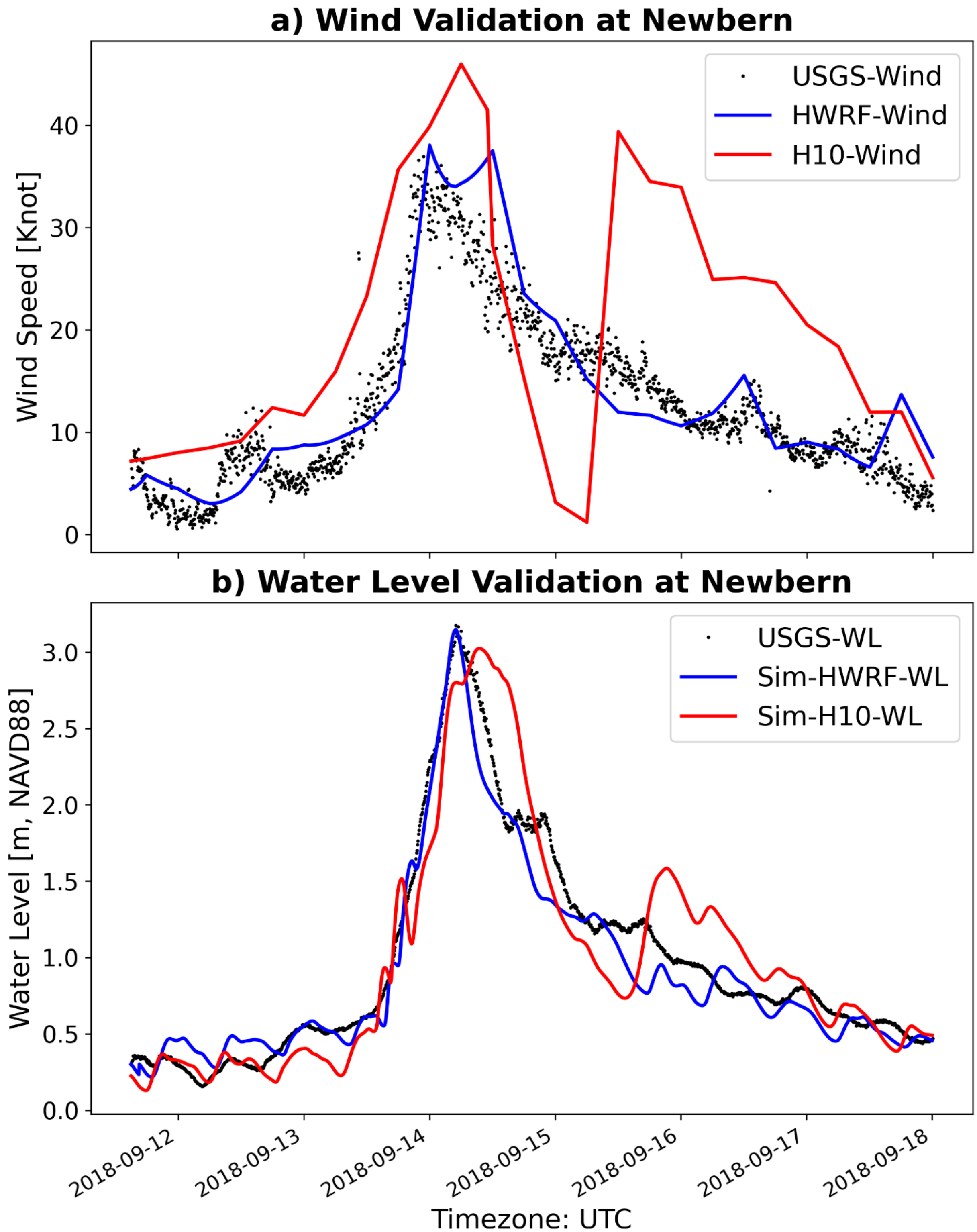

Fig. 2.11: As in Fig. 10, except at the USGS station near New Bern (USGS 02092576) that is located in the Neuse River at around 95 km from the shoreline.

Fig. 2.12 compares the maps of maximum inundation extents computed from the H10 and HWRF-driven simulations, and Fig. 2.13 shows the difference field. Broadly speaking, H10 produces higher surge inland and upstream of the Neuse and Pamlico Rivers, and along the NC coast extending from Wilmington (near the landfall) to Morehead City. HWRF, by contrast, produces a higher surge over an area stretching from the coast of Pamlico Sound to the lower reaches of the two major rivers. This contrast is clearly a product of the differing radial wind profiles as represented by the two models demonstrated earlier (see Fig. 2.4). Prior to and during landfall, H10 underestimates wind speed away from the storm center (> 100km), and this reduces the momentum for propelling the storm surge over the Northern portion of the domain. On the other hand, after landfall, H10 produces artificially high wind speed at closer range, apparently an indication that its current structural framework cannot realistically account for the reduction in wind speeds due to increased friction on land. H10's artificially high peak wind speeds close to the eye naturally translate into higher storm surges near the track and upstream of the estuaries.

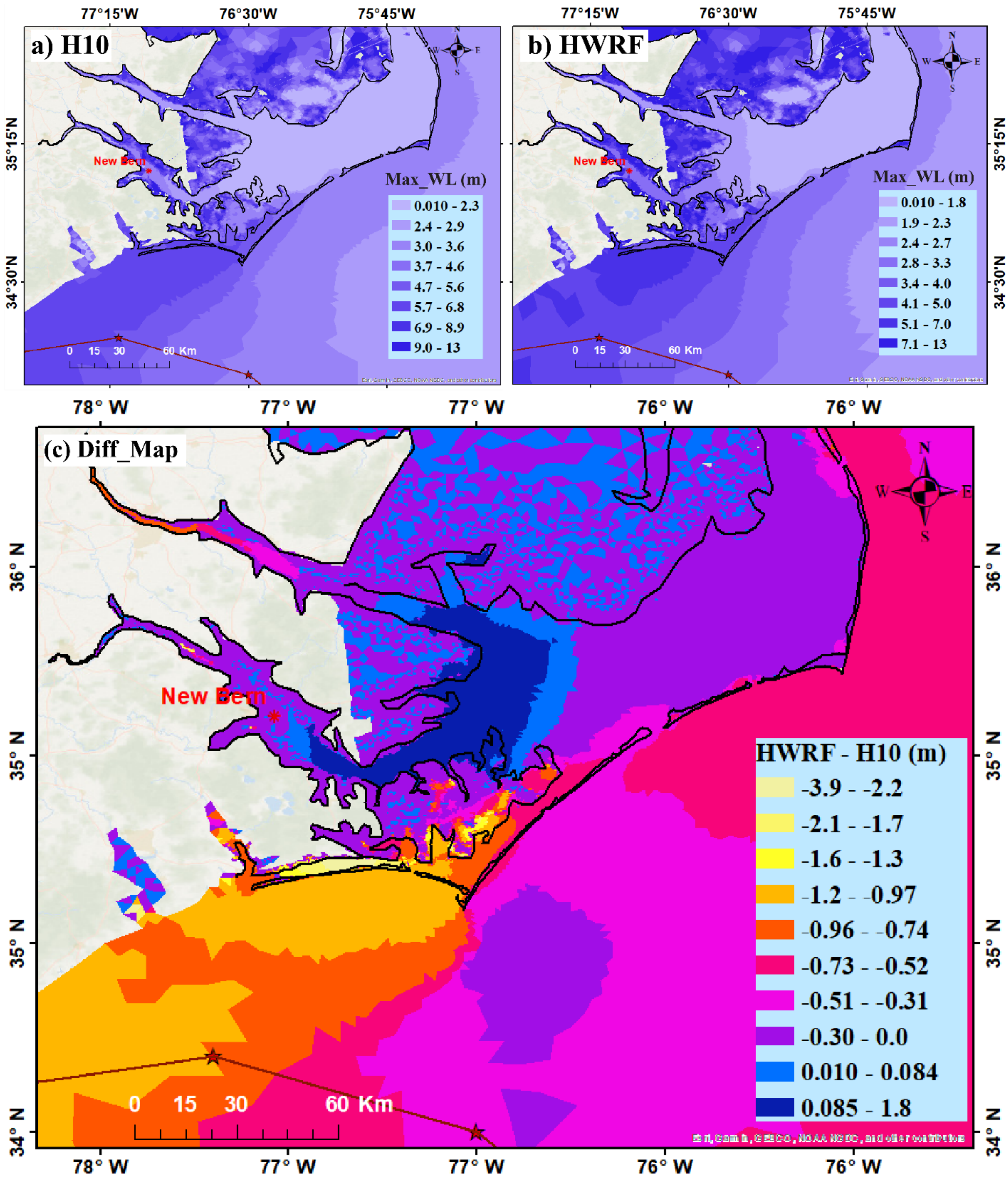

Fig. 2.12: Maps showing maximum flood extent, generated from 3-hourly output water level of Sep. 13 and 14, driven by wind and pressure fields produced by a) H10, and b) HWRF. (c) shows difference of simulated maximum water level (m) by Delft-3D forced by wind and pressure fields of HWRF and H10. The maximum water level is computed for each cell from 3-hourly series over 13-14 September (surrounding the landfall). Positive/negative values indicate higher maximum surge produced using HWRF/H10 product.

Fig. 2. 13 shows the validation of the simulated maximum surge produced by Delft3D-FM driven by H10-, and HWRF-driven against HWMs collected upstream and downstream of Neuse River and Pamlico Sounds (see Fig. 2.2 for locations). A total of 32 HWM stations were selected from more than 100 observations. The selection was based on the station's proximity to the Neuse River, especially the city of New Bern, as our model mesh was refined to focus on this region only. We also excluded some unrealistic HWMs based on the bed elevation of the locations. The simulated maximum water level was calculated for each location from the bed level to reasonably compare the observed HWMs and the simulated. From the figure, it is noticeable that both simulations are closely correlated with observations, but that driven by HWRF features lower RMSE and higher correlation. Regarding bias, the HWRF-driven maximum surges show a slightly positive overall bias, whereas those based on H10 are negatively biased. These results are consistent with the observations made in comparing the time series at New Bern (Fig. 2.11). They suggest that the HWRF reanalysis is likely a superior source forcing for the surge simulations, at least along the Neuse River and over the adjacent offshore locations.

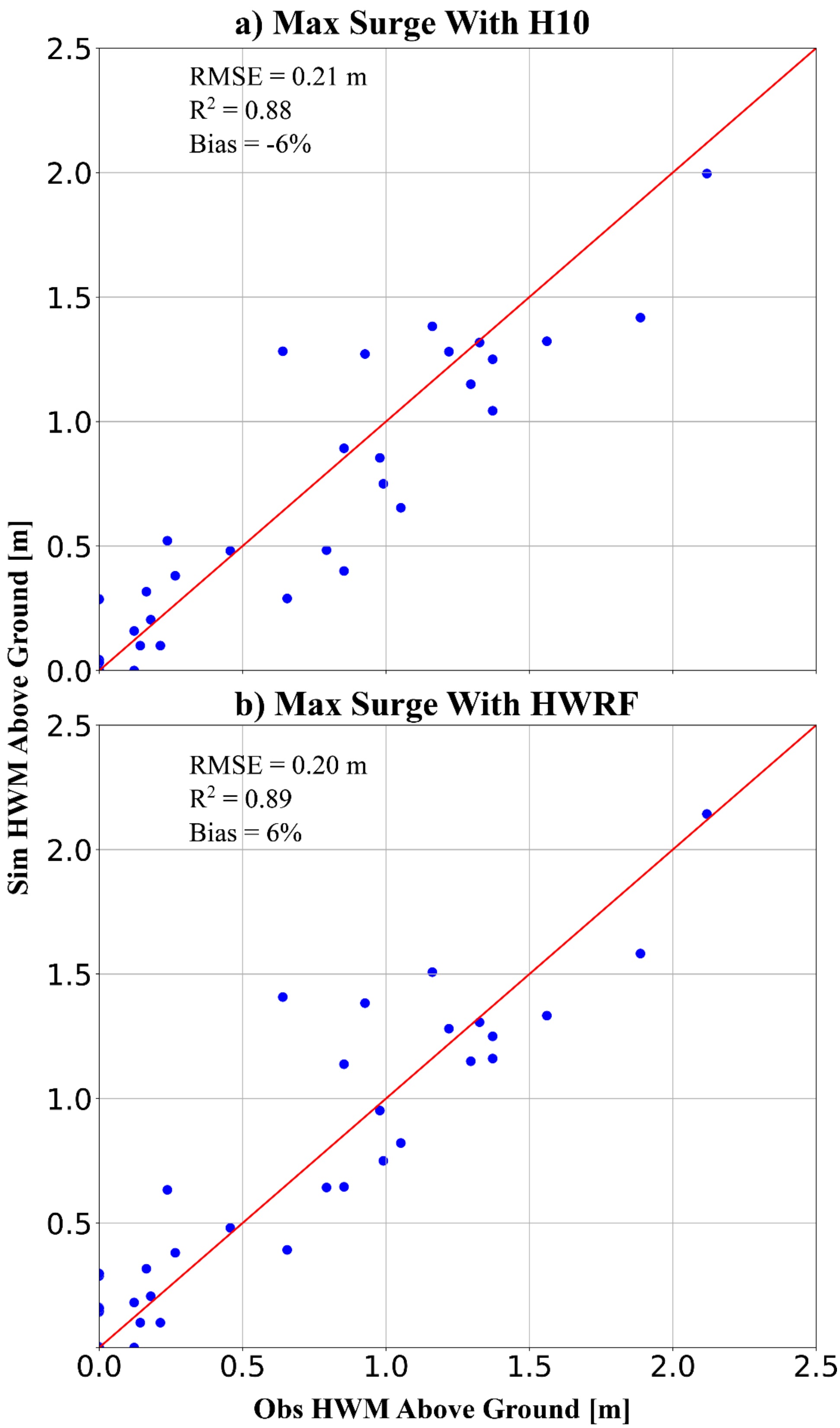
a) Max Surge With H10
RMSE = 0.21 m
R^2 = 0.88
Bias = -6%
b) Max Surge With HWRF
RMSE = 0.20 m
R^2 = 0.89
Bias = 6%
Sim HWM Above Ground [m]
Obs HWM Above Ground [m]
0.0
0.5
1.0
1.5
2.0
2.5

Fig. 2.13: Scatter plots of simulated maximum inundation depths vs. HWM observations along the Neuse River; (a) Maximum surge with H10, and (b) Maximum surge with HWRF.

2.4 DISCUSSIONS

Accurate meteorological forcing is crucial in analyzing and predicting coastal flooding caused by storm surges. For decades, parametric wind fields have been a major source of forcing input for storm surge prediction and analysis. Thus far, very few studies have touched upon the relative strengths of wind fields derived from parametric models vs. those based on the NWP model or the impacts of differential accuracy of wind fields on the fidelity of storm surge simulations. The present study addresses this gap by offering a detailed assessment of Hurricane Florence wind fields as represented by a parametric model (H10) and the HWRF reanalysis, and the storm surge simulations driven by the respective data set.

The comparisons underscore several fundamental shortcomings of the H10 model. These include its overly sharp decline with distance, its tendency to overpredict wind speeds on land, and its overall inability to resolve wind fields after the storm weakened into a depression. These shortcomings are apparent reflections of the structural limitations of the H10 model and the premises on which the model was formulated. Note that H10 improves upon the original H80 in major respects, such as relating pressure drops directly to wind at the surface rather than at the gradient level, relaxation of the cyclostrophic balance assumption for the inner core, and the use of new regression relations and parameter b_s. Nonetheless, it is evident that these improvements are inadequate for the model to reproduce the wind fields over the periphery of the storm or to capture the complex, rapid evolution of the vortex structure after landfall. Earlier studies, notably Hu et al. (2012), found positive bias in H80 wind fields and attempted to remedy this bias by incorporating canopy-based adjustment factors. Apparently, this bias remains an issue in H10 wind fields at least during the landfall of Florence, despite the aforementioned enhancements. Note that the bias is not entirely a result of structural inadequacy of H10: our analysis reveals suspiciously high Vmax in the best track data on which the model relies on to derive radial profile, and this can be a major contributor to the positive bias. In addition, H10's lack of representation of realistic ambient pressure, and more precisely, its inability to reproduce the sharp transition in a temperature gradient, may have played an essential role in rendering the negative bias in the farther range. Further, gradient wind or cyclostrophic assumptions may become increasingly poor approximations of the wind-pressure relationship as the storm weakens after landfall. Kepert (2001), for example, postulated the existence of a jet-like feature in the boundary layer of tropical storms, which later was verified by empirical observations (Hirth *et al.*, 2012). Moreover, in situ observations hint the presence of a secondary wind maximum at a farther range of Florence during and after landfall. Unfortunately, though H10 offers a mechanism for explicitly representing the secondary maximum, the implementation of this scheme is deemed impractical as it requires observational data to identify and define the secondary maximum - such data are hardly available a priori. How to leverage remotely sensed products such as brightness temperature from satellite imagers or sounders for this purpose will be a topic of future research.

While our analyses confirm the realism of HWRF wind and pressure reanalysis, these also uncover a few shortcomings of the product. Perhaps the most glaring is the sharp progression of the bias through landfall. Prior to, and even during the landfall, the radial profile of HWRF reanalysis exhibits a slightly positive bias over both NEQ and SWQ. After landfall, however, the bias became progressively negative. It should be noted that the bias calculations were not exactly rigorous in that the in-situ stations used for the comparisons over each quadrant are not situated precisely along the azimuth angle for which the HWRF wind profile was drawn. This caveat aside, this transition in bias after landfall is conspicuous enough to warrant close attention - it may well be reflective of potential mechanistic deficiencies in HWRF that inhibit its ability to resolve the dissipation phase of the Hurricane accurately. Possible mechanisms include inadequate representations of land surface conditions, over-smoothing of the wind profile of the 2-D vortex in creating the bogus vortex that results in discrepancies between model-simulated and observed maximum wind speed, and the lack of assimilation of surface observations after landfall. In particular, high soil moisture and inundation due to heavy rain are known to help sustain the intensity of tropical storms after landfall through the so-called "brown ocean effects" (Nair *et al.*, 2019; Yoo *et al.*, 2020). Florence produced torrential rain during its landfall, which may have helped slow down the storm's dissipation. The degree to which HWRF's coupling scheme resolves the interplay between the land surface and atmosphere is a topic that requires additional scrutiny.

The mixed results from the comparisons of Delft3D simulated storm water levels driven by the two sets of wind products are, in fact, illuminating. Using the H10 wind and pressure fields as input leads to higher storm surges in regions near the track, consistent with the observation that H10 tends to feature higher wind intensity close to the center of the storm. On the other hand, the H10-driven model simulation underpredicts the surge at New Bern even though the H10 features a higher peak wind speed locally. This seeming contradiction points to the fact that the magnitude of storm surge is not determined exclusively, or even strongly, by local wind speed and direction but by a complex aggregate of wind/pressure offshore as well as over land, geometries of coastline and estuaries, and the interplays between these factors. Comparisons of maximum surge level between H10 and HWRF clearly illustrate that the latter is able to induce higher surge over much of the lower Pamlico Sound stretching from the Barrier Island to New Bern, apparently a reflection of the ability of HWRF to resolve wind fields over further distance prior to the landfall. These findings collectively underscore the challenges in quantifying errors in storm surge simulations that arise from errors in simulated wind fields.

2.5 CONCLUSIONS

The wind validation was performed using data from 95 observing stations from both public and private sources. These include National Ocean Service (NOS) stations deployed nearshore, United States Geological Survey (USGS) temporary sensors along major rivers, Advanced Surface Observation System (ASOS) stations in airports, and sensors operated by Weather Flow Inc along the coast. In this study, a hydrodynamic model Delft3D was configured to simulate storm surges along the southeast using the Holland (2010), known as H10, and the Hurricane Weather Research and Forecasting (HWRF) wind/pressure fields. In order to minimize the complicating effects of model calibration, the model incorporates simple, spatially uniform roughness coefficients which underwent only light calibration. Key findings are summarized as follows:

1. The HWRF model captures the wind and pressure fields more accurately compared to the H10 model before the landfall of Hurricane Florence (2018). The latter features lower wind speeds away from the storm center, possibly an outcome of lacking representation of ambient wind.
2. During the landfall, H10 performs slightly better for stations within 100 km of the storm center, whereas HWRF tends to overpredict the peak wind. Yet, H10 wind speed drops sharply further away from the storm center, resulting in significant negative biases at those validation stations.
3. After landfall, Florence's strength declines rapidly. H10 is unable to reproduce the decline over the inner range (close to the storm center), resulting in large positive biases across stations. Over the outer range, however, H10's rapid drop-off in wind speed leads to broad negative

biases. Note that the positive bias near the storm center is partly a result of overly high maximum wind speed (Vmax) values in the best track data.

4. HWRF more accurately depicts the evolution of Florence's wind fields in time after landfall. Yet, it produces overly suppressed wind speeds across the southwest-northeast transect, and this suppression is particularly pronounced on the 15th.
5. After the weakening of Florence into a depression, the Radius of Maximum Wind Speed (RMV) expands drastically, and H10 is unable to produce realistic wind fields.
6. Storm surge simulations driven by HWRF and H10 yield mixed outcomes. HWRF-driven simulation accurately reproduces the surge near New Bern, NC, whereas H10-driven simulation features a slightly lower and delayed peak. In an offshore station near the storm track, using H10 as forcing leads to a slightly better depiction of the magnitude and timing of the surge.
7. Inundation depth produced by HWRF-driven simulation is conspicuously higher than that from the H10-forced simulation over the downstream portions of the Neuse and Pamlico Rivers. By contrast, it is broadly lower offshore, along the upper reaches of the two rivers, and over areas close to the track.

In broad terms, the study illustrates the strength of the HWRF model in reproducing the radial wind profile of Hurricane Florence, depicting the evolution of the wind fields during and after the landfall, and capturing the spatial patterns of wind during the weakening phase of the storm on the 15th. When compared against HWRF, the shortcomings of the H10 model are evident. These include its overly sharp decline with distance, its tendency to overpredict wind speeds on land, and its overall inability to resolve wind fields after the storm weakened into a depression. These shortcomings are apparent reflections of the structural limitations of the H10 model and the premises on which the model was formulated. It is clear that improvements in the structure and parameter estimation scheme introduced in H10, including the relaxation of the cyclostrophic balance assumption for the inner core, and the use of new regression relations and parameter b_s, are inadequate for the model to reproduce the wind profile on land.

Hu *et al.* (2012) noted a similar positive bias of the H80 wind field on land and attempted to remedy this bias by incorporating canopy-based adjustment factors. However, it is worth drawing the distinctions between H10 and H80, as the latter explicitly relies on the cyclostrophic balance and has a rather imprecise definition of elevation associated with its wind profile whereas the former does not. One major contributor to H10's positive bias in the inner range is the suspiciously high Vmax in the best track data on which the model relies on to derive radial profile. While in situ data used in this study was insufficiently dense near the RMV to directly appraise the validity of the Vmax, they point to a distinct possibility that the Vmax is biased high in the later part of the window. In addition, H10's lack of representation of realistic ambient pressure may have played an important role – it leads to an artificially suppressed pressure gradient which translates into lower wind speed. Further, the H10 wind profile structure is perhaps broadly unsuitable for modeling the wind field of tropical storms after landfall as these are strongly modulated by interactions of the storm with terrain features. It is worth pointing out that in situ observations hint the presence of a secondary wind maximum at a farther range of Florence during and after landfall. H10 does offer a mechanism for representing this maximum, but it was not implemented due to a lack of a priori information to establish the magnitude and location of this maximum, and the concern of barotropic instability.

Similar to many studies conducted earlier on retrospective analysis of storm surges, our investigation was constrained by data availability and computational demand. Owing to a shortage of in-situ observation and the focus on a single storm, we were unable to perform detailed, spatially distributed validation of storm surge simulations along the Pamlico sound and adjacent land or assess the ability of model calibration to compensate for errors in forcings. As a result, a number of questions concerning the fidelity of the two sets of surge simulations remain unanswered. In addition, some of the mechanisms that impact the surge were omitted for computational tractability. In this study, the impacts of wave setup were assumed negligible owing to the consideration of the unique geography of the study region, where such impacts were likely subdued due to the presence of the Barrier Islands. Extending the comparisons to cover additional landfalling tropical storms and surge cases over different geographic domains will offer further insights into the differential strengths of H10 and HWRF, their structural underpinnings, and manifestations of mechanistic deficiencies in wind fields in surge simulations and predictions. In particular, it is of great interest to assess the effects of errors in the parametric wind models associated with the lack of explicit representation of the ambient wind fields on surge in situations where wave setup likely plays a prominent role through coupled wave-surge simulations and to investigate potential mechanisms for alleviating such effects, e.g., the inclusion of additional velocity-range pairs and superposition of parametric wind fields on ambient winds from numerical weather model simulations.

Chapter 3 Land Surface Controls the Intensity and Locations of Compound Flooding by Hurricane Florence

ABSTRACT

As the intensity and frequency of landfalling tropical storms are likely on the rise in a warming climate, coastal communities are increasingly being exposed to flooding caused by storm surges compounded by heavy rainfall. Land surface attributes influence the intensity of compound flooding in coastal areas. This work reconstructs and examines the compound flooding processes during Hurricane Florence in 2018. A prominent feature of this event is that the storm penetrated more than 60 km inland through the Neuse River in North Carolina, causing more than a 3-m surge upstream outside the coastal zone. This surge most likely has magnified the fluvial flood peak that arrived subsequently by producing the backwater effects. The focus of the investigation is on the impacts of vegetation on the intensity of compound effects. To this end, an integrated ocean-riverine hydrodynamic model is developed using the Delft3D-FM suite, and the model ingests inflow from National Water Model 2.1 reanalysis. The model undergoes calibration to accurately capture the peak surge up to the surge-dominated and fluvial zones. Then the calibrated model is used for performing sensitivity runs to appraise the impacts of land surface control. The presence of marshland significantly impacts the compound zone, and the compound area was reduced by 35 % for the highest intensity of salt marsh.

Keywords: Delft3D-FM, Florence, compound flooding, storm surge, geomorphic control

3.1 INTRODUCTION

Coastal communities are increasingly being exposed to flooding caused by storm surges compounded by heavy rainfall because of the increasing trend in intensity and frequency of landfalling tropical storms due to climate change (Milly *et al.*, 2002; Moftakhari *et al.*, 2015; Bevacqua *et al.*, 2019). Besides, the number of people migrating to the bay areas has been increasing in recent years. Presently, about 60% of the world's population lives within 60 km of the coastline, and the number is expected to rise to 75% within a few decades (Rao *et al.*, 2008). By contrast, the number of severe storms with higher magnitudes is expected to increase in the foreseeable future - as a consequence of a moderate increase in greenhouse gases, the frequency of category 4 and 5 hurricanes in the Atlantic Basins will be increased by 45-87% by the end of 21st century (Knutson *et al.*, 2013).

Currently, coastal flooding has become one of the main natural disasters, occurring more frequently than ever before. It poses economic damages and losses of lives, as demonstrated by recent tropical cyclones, such as Katrina, Ike, Irene, Sandy, Harvey, Irma, Maria, and Florence along the U.S. coasts and other parts of the world (Jonkman, 2005; Chang *et al.*, 2009; Adelekan, 2011). Because of the combined effect of rainfall and storm surge from storm activity, an average economic loss caused by coastal flooding in 2005 was estimated to be approximately $6 billion annually in the biggest coastal cities in the world. Because flood exposure is increasing in coastal cities owing to growing populations and assets, the changing climate, and subsidence (Hallegatte *et al.*, 2013). Seawaters rise above the local astronomical tide level during a storm surge due to winds and low-pressure systems, where the wind is usually the primary source and atmospheric pressure the secondary (Jordi *et al.*, 2019). Therefore, a storm surge results in coastal flooding.

Furthermore, flooding in the coastal areas can emerge either from ocean surges, high river discharges, and extreme rainfalls in the upstream watersheds or a combination of all these flood drivers (Zheng *et al.*, 2013; Wahl *et al.*, 2015; Bilskie and Hagen, 2018). Most of the time, damages from the combined hazards during compound flooding are more severe than that of individual sources (Zscheischler *et al.*, 2018). For instance, Florence in 2018 caused major flooding in the vicinity of the Neuse River, especially at New Bern, because of the combined effect of heavy precipitation (i.e., 900 mm) and high surge (i.e., 3 m) from the Atlantic Ocean (Ye, Huang, *et al.*, 2020). Additionally, compound flooding can result from tropical and extratropical cyclones (Cho *et al.*, 2012; Li *et al.*, 2006; Valle-Levinson *et al.*, 2020). In addition, the intensity of compound flooding in the coastal areas is influenced by attributes of the land surface, such as the presence of salt marsh may control the intensity of compound flooding.

However, the definition of the compound zone is still debatable. We need an appropriate method to define the interaction among all processes to identify the compound zone. Ye, Huang, *et al.*, 2020 have recently introduced a dominance map to identify compound zones using an arbitrary compound ratio of 20% and 80%. They calculate the metric based on the departure of the water level from the initial state. The water surface elevation for the ocean (i.e., where depth > 0) and water depth for land (i.e., where depth <0) are used to calculate the disturbances. Using two different metrics, such as elevation and depth metrics, simultaneously to calculate disturbances introduces errors at the boundaries between land and ocean. Besides, the metric did not consider the time of the peak water level as it is the major contributing factor to determining the compound zones. We know the ocean is tide and surge-dominated, and high-elevation watersheds are rainfall-dominated. Therefore, judging the areas with shallow depths using the same metric used for the ocean is often misleading and may introduce false compound zones. Thus, this study presents a time- and storm-independent alternative metric based on the peak depth for all regions within the model domain and specifies a threshold value considering the time of the peak water levels from both ocean and riverine processes.

Hence, the present study is motivated by the need to define the alternative metric to identify the regions with consistently significant compounding effects across storms (i.e., Florence) and assess the impacts of land surface controls in determining the maximum impact caused by storm surges. The specific objectives of the present study are threefold. The first is to calibrate the hydrodynamic model extensively to capture the observed water levels at multiple upstream stations using the predefined most accurate wind forcing (i.e., HWRF). The second is to define an alternative metric to identify the regions with consistently large compounding effects based on the alternative metric. The third is to assess the impacts of land surface control on the intensity and location of compound flooding.

The remainder of this article is organized as follows. Section 2 provides descriptions of the material and methods, including but not limited to selecting appropriate wind forcing (i.e., HWRF) for the hydrodynamic model (i.e., Delft3D-FM), initial model parameters and inputs generation, criteria to define compound flooding, and validation matrices. The objectives of this study are discussed in Section 3 (i.e., Results), where the regions with consistently large compound flooding are identified based on an alternative metric that defines compound flooding. The impact of land surface controls on the intensity and locations of compound flooding is also discussed. Section 4 discusses the findings of the study in detail concerning the objectives, and Section 5 summarizes the findings and offers recommendations for future works.

3.2 MATERIALS AND METHODS

3.2.1 Study Area

The study area is located in North Carolina, along the Neuse River, especially at New Bern and upstream of it. A study area map is shown in Fig.3.1. We selected this location because a powerful Hurricane Florence caused catastrophic damage in the Carolinas in September 2018, primarily because of freshwater flooding due to torrential rain, causing a total fatality of 53. The total estimated damage was $24.23 billion (USD), which is why this area is very important for studying the risk of flooding. Hurricane Florence was chosen for the study as it is one of the costliest (i.e., 12th) hurricanes that hit the mid-Atlantic region in recent history, and it produced a storm surge that penetrated far upstream (>50 km). Wind speed may have intensified flooding along the Neuse River and major sounds. Hurricane Florence made its first landfall south of Wrightsville Beach, NC, on 14 September while retaining Category 1 strength, even though wind speed was mainly below 70 mph while approaching the coast of Carolinas.

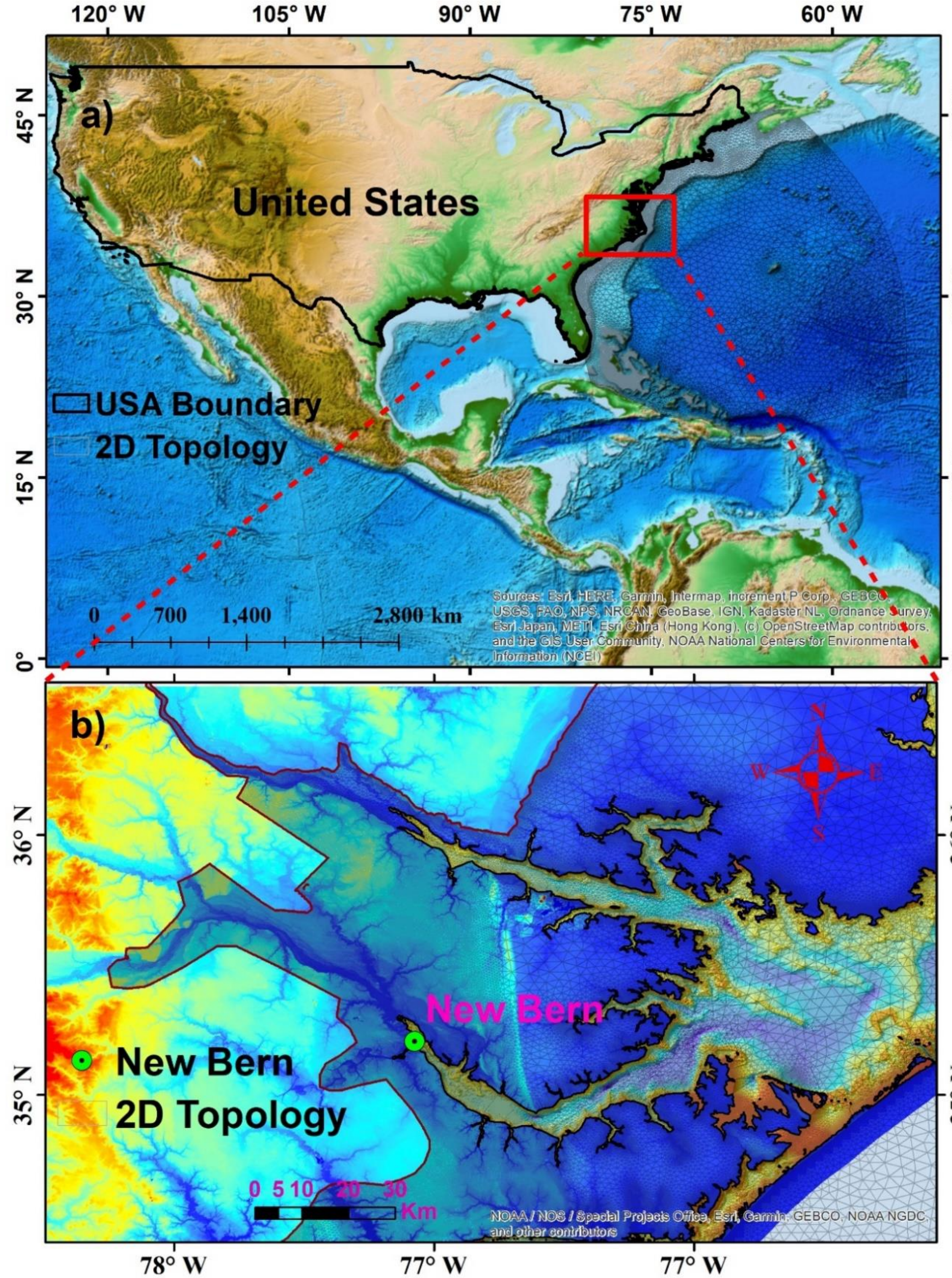

Fig. 3.1: Map showing the location of the study area; (a) Delft3D-FM model domain within U.S.A. boundary and North Atlantic Ocean, (b) a blow-up of the region that is the focus of the analysis on storm

surge. Superimposed are the 2D topology and New Bern in the vicinity of Neuse River which experienced severe flooding during the landfall of Florence.

3.2.2 Alternative metric for measuring compound effects

The baseline metric proposed by Ye et al. (2020) uses a ratio of event-wise maximum inundation depth/extent attributable to the act of a specific forcing alone to that resulting from the act of all forcings holistically. Without any consideration of lag, this ratio tends to obscure the interactions among forcings through the landfall of tropical cyclones (TCs).

In this study, we propose a new, modified metric for measuring the intensity of interactions among drivers of coastal flooding during major TC landfalls considering the present knowledge gaps on processes governing compound effects and responding to the need to measure such effects more precisely. The metric preserves the use of peak inundation as a measure of the magnitude of flooding. Still, it measures the changes of this magnitude within the time window where the maximum event peak was attained after excluding a specific forcing.

Here, we define the alternative metric as a ratio of the departure of peak water depth produced by a particular forcing to the peak water depth produced by combined forcing. Mathematically, we can express the alternative metric by the following formula:

$$\text{Alternative Metric } = \frac{(Max\_WD)_{CF} - (Max\_WD)_{F}}{(Max\_WD)_{CF}}$$

Where, $(Max\_WD)_{CF}$ and $(Max\_WD)_{F}$ are the peak water depth produced by the combined forcing (i.e., including tide, surge, riverine) and peak water depth produced by a particular forcing, respectively.

For example, suppose the peak water depth produced by only riverine flow is 2.5 m, and that produced by combined forcing (i.e., riverine, tides, and surges) is 2.6. In that case, the alternative metric is calculated as follows:

The alternative metric factor for riverine flow $= \frac{(Max\_WD)_{CF} - (Max\_WD)_{F}}{(Max\_WD)_{CF}} = \frac{2.6 - 2.5}{2.6} = 0.038$

As the difference in peak water depth between the combined forcing and riverine flow is 3.8 %, based on the 20%, 80% compound ratio, this particular location is river-dominated.

3.2.3 Description of Storm Surge Model

The Delft3D Flexible Mesh, also known as Delft3D-FM, is a fully integrated software suite by Deltares (2014), consisting of models that simulate a variety of processes in the ocean, estuarine, tidal, and inland streams, including those related to flow, sediment transport, morphodynamics, and water quality. Its hydrodynamic model, Delft3D-FLOW, is a finite-element model that uses an unstructured (triangular) grid mesh. Delft3D-FLOW allows for both 2- and 3-dimensional representations of flows. The 2-D version solves the shallow-water equations. In this study, we implemented a 2-D version of the model for its computational efficiency, and our region of focus spans the Pamlico Sound and the Neuse River, where severe flooding was reported.

3.2.3.1 Model Physics of FLOW Module

The FLOW module in the Delft3d-FM software suite is based on the Reynolds-Averaged Navier-Stokes (RANS) equations (Kim *et al.*, 2016; Díaz-Carrasco *et al.*, 2021), which is simplified for an incompressible fluid under the Boussinesq approach, and with the shallow-water assumptions. The momentum equations in both x- and y- directions (σ–coordinates) are given by (1) and (2), respectively, where h is the total water depth ($h = d + \eta$), d is the water depth according to a reference level and η is the variation of the water level (Broomans *et al.*, 2003). The governing equations are as follows:

$$\frac{\partial u}{\partial t} + u\frac{\partial u}{\partial x} + v\frac{\partial u}{\partial y} + \frac{\omega}{h}\frac{\partial u}{\partial \sigma} = -\frac{1}{\rho_0}\left(\frac{\partial p}{\partial x} + \frac{\partial \sigma}{\partial x}\frac{p}{\sigma}\right) + fv + F_x^v + \frac{1}{h^2}\frac{\partial}{\sigma}\left(V_v^t\frac{\partial u}{\partial \sigma}\right) \tag{1}$$

$$\frac{\partial u}{\partial t} + u\frac{\partial u}{\partial x} + v\frac{\partial u}{\partial y} + \frac{\omega}{h}\frac{\partial v}{\partial \sigma} = -\frac{1}{\rho_0}\left(\frac{\partial p}{\partial x} + \frac{\partial \sigma}{\partial x}\frac{\partial p}{\partial \sigma}\right) + fv + F_y^v + \frac{1}{h^2}\frac{\partial}{\partial \sigma}\left(V_v^t\frac{\partial u}{\partial \sigma}\right) \tag{2}$$

where F_x^v and F_y^v represent the horizontal viscosity terms:

$$F_x^v = \left(\frac{\partial}{\partial x} + \frac{\partial \sigma}{\partial x}\frac{\partial}{\partial \sigma}\right)\tau_{xx} + \left(\frac{\partial}{\partial y} + \frac{\partial \sigma}{\partial y}\frac{\partial}{\partial \sigma}\right)\tau_{xy} \tag{3}$$

$$F_y^v = \left(\frac{\partial}{\partial x} + \frac{\partial \sigma}{\partial x}\frac{\partial}{\partial \sigma}\right)\tau_{xy} + \left(\frac{\partial}{\partial y} + \frac{\partial \sigma}{\partial y}\frac{\partial}{\partial \sigma}\right)\tau_{yy} \tag{4}$$

and the Reynold stresses τ_{xx}, τ_{xy} and τ_{yy} satisfy (under the Boussinesq approach):

$$\tau_{xx} = 2V_h^t\left(\frac{\partial u}{\partial x} + \frac{\partial \sigma}{\partial x}\frac{\partial u}{\partial \sigma}\right) \tag{5}$$

$$\tau_{xy} = V_h^t\left(\frac{\partial u}{\partial y} + \frac{\partial \sigma}{\partial y}\frac{\partial u}{\partial \sigma} + \frac{\partial v}{\partial x} + \frac{\partial \sigma}{\partial x}\frac{\partial v}{\partial \sigma}\right) \tag{6}$$

$$\tau_{yy} = 2V_h^t\left(\frac{\partial v}{\partial y} + \frac{\partial \sigma}{\partial y}\frac{\partial v}{\partial \sigma}\right) \tag{7}$$

In the previous equations, u, v, and ω are the x-, y- and z- Reynolds' time-averaged components in σ-coordinates and V_h^t and V_v^t are the horizontal and vertical turbulent viscosity, respectively.

The vertical momentum equation is not presented here as it is reduced to the hydrostatic pressure distribution under the shallow-water assumption. Therefore, besides (1) and (2), one extra equation is needed to obtain the vertical velocity w. This may be achieved by computing the continuity equation in σ-coordinates:

$$\frac{\partial \eta}{\partial t} + \frac{\partial hu}{\partial x} + \frac{\partial hv}{\partial y} + \frac{\partial \omega}{\partial \sigma} = 0 \tag{8}$$

Many recent storm surge modeling efforts account for the impacts of nearshore waves, which have been shown to play major roles in amplifying the surge (Sheng *et al.*, 2010; Weaver and Slinn, 2005; Dietrich *et al.*, 2011; Abdolali et al., 2021). During the landfall of Hurricane Katrina, wave setup was shown to bring more than 0.5 m of additional surge along the lower Mississippi River Delta (Dietrich et al., 2010; Bunya et al., 2010). Over the study domain, however, we found the impacts of nearshore waves often muted due to the sheltering effects of the Barrier Island. As a result, we opted to exclude the modeling of nearshore waves (Ye, Huang, *et al.*, 2020). In this study, we excluded the wave module to avoid complexity due to limited access to computational facilities. This research team will use the wave model in future studies to test the impact of the wave during a storm surge event.

3.2.4 Model Configuration:

To configure the storm surge model using Delft3D-FM, we combined several high-quality bathymetric and topographic data for this study. The western North Atlantic Ocean was built using global SRTM15_PLUS bathymetry (Tozer *et al.*, 2019). The NCEI Bathymetric Digital Elevation Model (30-meter resolution) data was utilized to enhance the representation of the bathymetry of the barrier island and Pamlico sound (Mulligan *et al.*, 2019). These data are merged to create an unstructured grid mesh that spans much of the west Atlantic – the model domain extends from latitude 34.0° N and longitude 78.0° W to latitude 36.5° N and longitude 72.0° W (Fig. 3.1). We used a combination of triangular and rectangular meshes of various resolutions to resolve the deep ocean, estuaries, and narrow channels. The resolution ranges from 50 km in the ocean, 500-m nearshore, to 10-m for the upstream channels. The courant number was fixed at 0.70 with user time steps of 30 seconds and a maximum time step of 600 seconds. The nodal update interval was also set at 30 seconds. The initial water level was fixed at the mean sea level, and the water density was considered as 1025 kg/m^3 for saline water. Additionally, the uniform horizontal eddy viscosity and eddy diffusivity of 0.2 m^2/s and 20 m^2/s were used. However, space-varying friction coefficients for Manning's friction type were assigned based on the water depth. Manning's n values of 0.012, 0.015, 0.018, 0.023, and 0.025 were assigned for the deep ocean, nearshores, shallow waters, channels, and over lands, respectively. For the wind drag coefficient type, we implemented 2-break points based on Smith & Banks; the values are 0.000063 and 0.00723 for the break-points wind speed of 0 and 100 m/s, respectively. All default values were used for numerical parameters, and the dry cell threshold was fixed at 0.01 m.

3.2.5 Boundary Conditions

The storm model requires land, ocean, and atmospheric forcings to drive the model. Discharge time series at the land boundary, tidal water level at the ocean, and wind and pressure fields as atmospheric boundary conditions are used as usual practice for any storm surge model. In this study, we utilized observed discharge time series from USGS at the upstream land boundary, and output from TPXO 9.0 global tidal model (Egbert and Erofeeva, 2002) as open water boundary condition as the astronomical tide can be a crucial factor that contributes to coastal inundation during a storm event (Lai *et al.*, 2021). We used only 8 dominant tidal constituents, such as diurnal constituents (i.e., k_1, o_1, p_1, and q_1), and semi-diurnal constituents (i.e., m_2, s_2, n_2, and k_2) out of 37 to generate the tidal water level at the deep ocean. Additionally, we integrated the outputs from National Water Model (NWM) as lateral boundaries. However, we excluded the rainfall on the grids as we already integrated the flow from NWM to avoid complexity. For the atmospheric forcings, including surface wind and pressure, we employed HWRF reanalysis data as this dataset was found to be more accurate than a parametric wind model (i.e., Holland 2010) from a study conducted by this author (Rahman *et al.*, 2022). We interpolated the zonal and meridional wind speeds (u and v, respectively) and surface pressure onto the Delft3D-FM mesh using bilinear interpolation.

3.2.6 Data sets

To calibrate the storm surge model for the upstream of Neuse River, especially the upstream of New Bern, we collected water level time series from USGS stations. In this study, the hydrodynamic model calibration was extended to two upstream stations located within the model domain. As this study is a continuation of the previous research conducted by this author, and the model was calibrated downstream of New Bern (Fig.3.1) in the previous study conducted by this author against observed water levels and high-water marks using various wind forcing (Rahman *et al.*, 2022). For the lateral boundary condition, we processed NWM V2.1 data using python scripts written for this study.

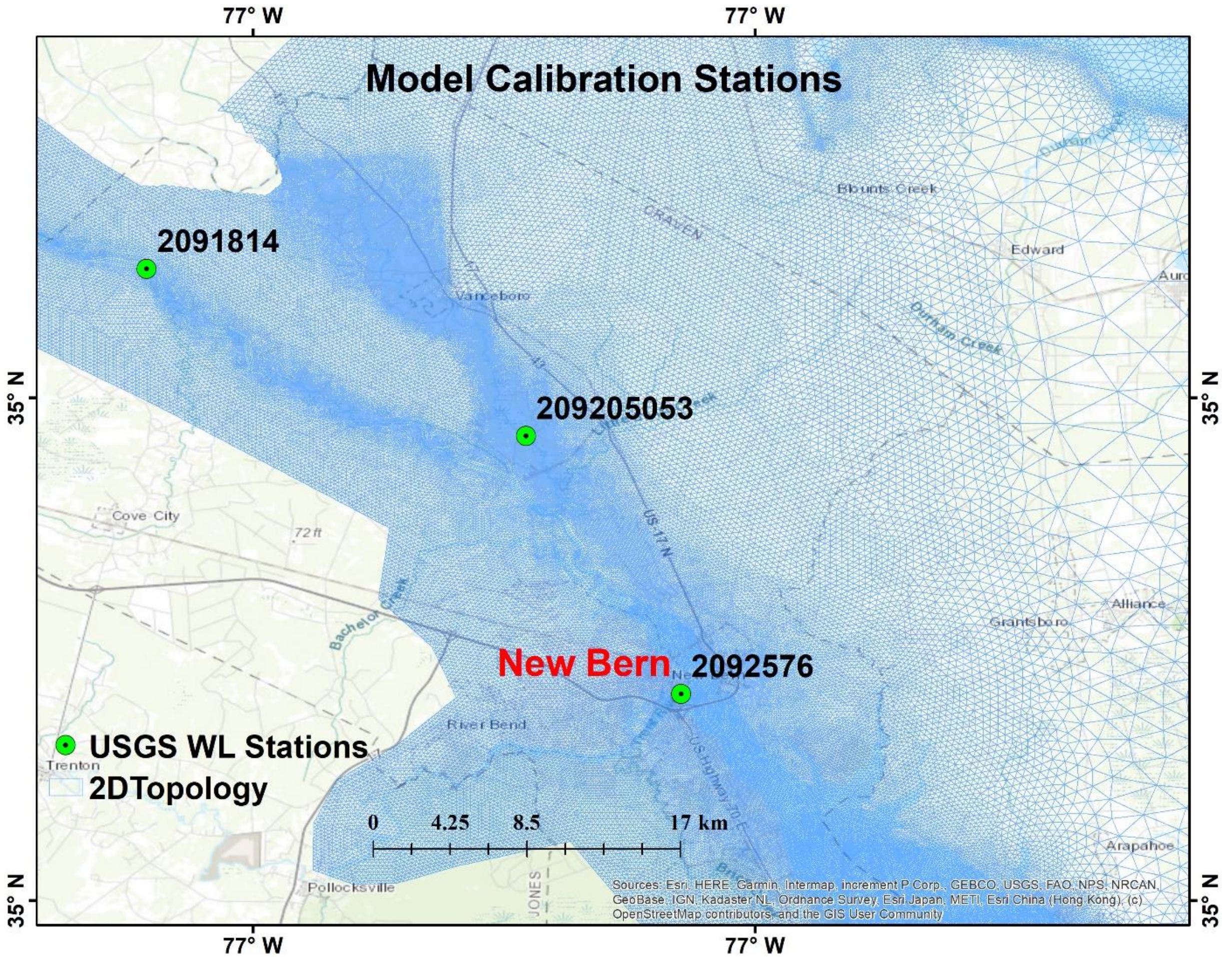

Fig. 3.2: Map showing USGS water level measuring stations; the model was calibrated at these stations against water level.

Conventional metrics were employed for judging model performance, including percentage bias (P.B.), Pearson's correlation (R), and root mean squared error (R.M.S.E.). These metrics are defined as follows:

$$PB = \frac{\sum_{i=1}^{n}(Q_{sim,\mathrm{i}} - Q_{obs,i})}{\sum_{i=1}^{n} Q_{obs,i}} \times 100 \tag{9}$$

$$\mathrm{R} = \frac{\sum_{i=1}^{n}(Q_{obs,i} - \bar{Q}_{obs,i})(Q_{sim,i} - \bar{Q}_{sim,i})}{\sqrt{\sum_{i=1}^{n}(Q_{obs,i} - \bar{Q}_{obs,i})^2}\sqrt{\sum_{i=1}^{n}(Q_{sim,i} - \bar{Q}_{sim,i})^2}} \tag{10}$$

$$\mathrm{RMSE} = \sqrt{\frac{\sum_{i=1}^{n}(Q_{sim,i} - Q_{obs,i})^2}{n}} \tag{11}$$

where $Q_{obs,i}$ and $Q_{sim,i}$ are observed and simulated datasets (i.e., wind speed, barometric pressure, or water level), respectively; and n is the number of records in the time series.

3.3 RESULTS

3.3.1 Model Calibration Against Water Level

We calibrate the model at three USGS stations, mainly upstream of Neuse River, to capture the flood extent better at the upstream watersheds. The comparison plots of observed and simulated water levels for calibration stations are shown in Fig.3.3. The locations are shown in Fig.3.2. The plots are arranged from upstream to downstream as shown in Fig.3.2. The most upstream calibration station (i.e., 02091814) is located at Fort Barnwell on Neuse River. The RMSE value at this calibration station is 0.19 m, Pearson's correlation coefficient is 0.99, and Nash-Sutcliffe efficiency is 0.98 with a negative bias of -0.50 % (Table 3.1). The model underestimates the flood peak at this location; however, the volumetric comparison is within the acceptable range. Fig.3.3 shows that the surge did not reach this station, so the water level is only from the upstream discharge boundary and lateral boundaries from NWM. The following calibration station (i.e., 0209205053) is located on Swift Creek at Swift Creek St Ferry, and the model performance statistics are also presented in Table 3.1. From Fig.3.3, it is noticeable that this station has a little bit of tidal influence and flow from the NWM. This station is within the compound flooding zones, where both tide, surge, and riverine flow contribute to the flood peaks. The third calibration station (i.e., 02092576), located on Neuse River at New Bern, is surge-dominated. Calibrating such stations is somewhat tricky without tuning the atmospheric forcing, as the surge mainly originates from wind speed and pressure. Hence, the calibration of this station was adopted directly from the previous study conducted by this author (Rahman *et al.*, 2022), and the statistics are presented in Table 3.1.

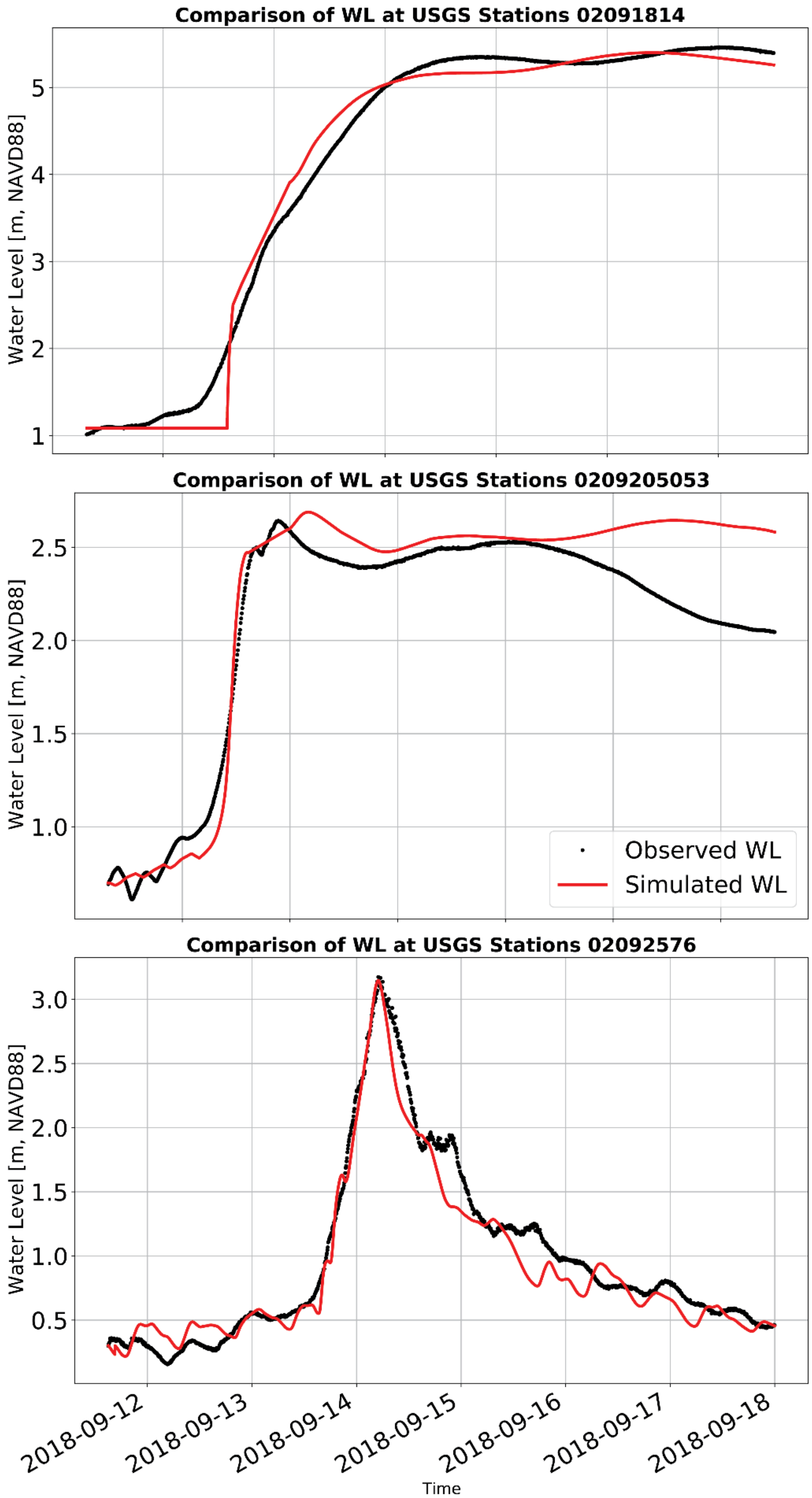
Comparison of WL at USGS Stations 02091814
Water Level [m, NAVD88]
1
2
3
4
5
Comparison of WL at USGS Stations 0209205053
Water Level [m, NAVD88]
1.0
1.5
2.0
2.5
Observed WL
Simulated WL
Comparison of WL at USGS Stations 02092576
Water Level [m, NAVD88]
0.5
1.0
1.5
2.0
2.5
3.0
2018-09-12
2018-09-13
2018-09-14
2018-09-15
2018-09-16
2018-09-17
2018-09-18
Time

Fig. 3.3: Calibration plots at three USGS water level observation stations.

Table 3.1: Model performance statistics for calibration stations

Station ID	Location	RMSE (m)	Correlation Coef. (R)	NSE	% Bias
02091814	Fort Barnwell	0.19	0.99	0.98	-0.50
0209205053	Swift Creek St Ferry	0.25	0.95	0.83	7
02092576	New Bern	0.21	0.96	0.90	-6

3.3.2 Sensitivity Analysis

We run the baseline model for four conditions: full forcing, riverine, tide, and surge. The list of sensitivity runs is presented in Table 3.2. the table below also includes the sensitivity runs for land surface controls.

Table 3.2: Run conditions of sensitivity analysis

Scenarios	Descriptions
Baseline	Full forcing, including forcing from tides, surges, and rivers
Tide only	Base model forced with tide only
Tide + Surge	Base model forced with the tide and surge
Riverine	Base model forced with river flow from NWM
Effect of land surface control	
Baseline	Full forcing with Manning’s n = 0.050, 0.075, 0.10
Tide only	Tide with Manning’s n = 0.050, 0.075, 0.10
Tide + Surge	Tide and surge with Manning’s n = 0.050, 0.075, 0.10
Riverine	River flow only with Manning’s n = 0.050, 0.075, 0.10

We calculated the contribution of each force compared to all forcings at every node within the computational domain. Then we generated the dominance map using the metric suggested by Ye, Huang, *et al.*, 2020 to identify the compound zone. We call this metric as baseline metric in this study. Fig. 3.4-a demonstrates the compound zone using the baseline metric. Then we generated the dominance map using the alternative metric introduced in this study but with the same threshold values as the baseline to compare their credibility. The map is presented in Fig. 3.4-b. From the comparison of Fig. 3.4-a and b, we notice that the compound zone defined by the baseline metric is overestimated compared to the alternative metric.

As the baseline metric does not account for the peak times of the individual contribution from riverine, tides, surges, and rainfall, it arbitrarily uses a compound ratio of 20% and 80% to identify the compound zone. However, the alternative metric account for the peak time to calculate the metric as a percentage of the total disturbances. This scenario is visible in the time series comparison shown in Fig.3.5 for two locations, one on the Neuse River and the other on Swift Creek. Station 35, located in the vicinity of the Neuse River, shows that the location has both tidal and riverine contributions almost similar to the total contribution. However, their peak time is different, meaning there is no interaction between the peaks to develop a compound effect at this location. Additionally, the compound ratio calculated for both riverine and surge is not within the limit of 20% and 80%; however, this location has been identified as compound flooding based on the baseline metric. In contrast, the alternative metric does not identify the location as a compound zone using the same thresholds. Station ID 65, located in the vicinity of Swift Creek, demonstrates river-dominant according to alternative metrics. Still, the location has been identified as a compound zone as per the baseline metric, which sometimes misrepresents the actual compound zone.

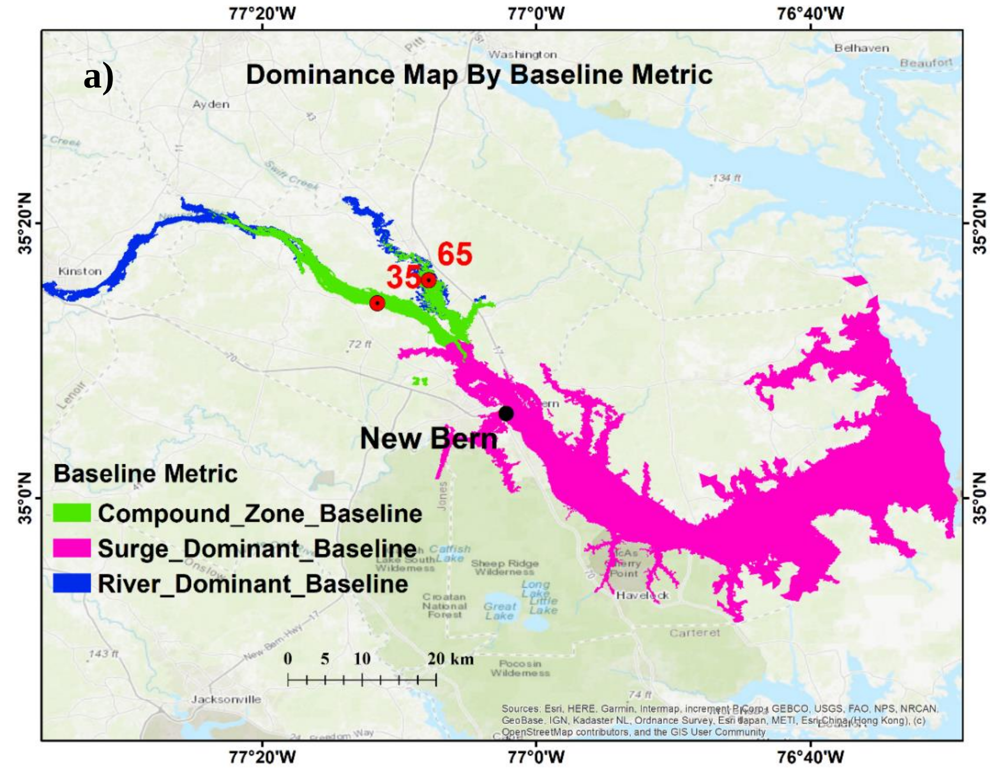

a)
Dominance Map By Baseline Metric
77°20'W
77°0'W
76°40'W
35°20'N
35°0'N
65
35
New Bern
Baseline Metric
Compound_Zone_Baseline
Surge_Dominant_Baseline
River_Dominant_Baseline
0 5 10 20 km
Kinston
Ayden
Washington
Belhaven
Jacksonville
Havelock
Carteret
Sources: Esri, HERE, Garmin, Intermap, increment P Corp., GEBCO, USGS, FAO, NPS, NRCAN, GeoBase, IGN, Kadaster NL, Ordnance Survey, Esri Japan, METI, Esri China (Hong Kong), (c) OpenStreetMap contributors, and the GIS User Community

b)

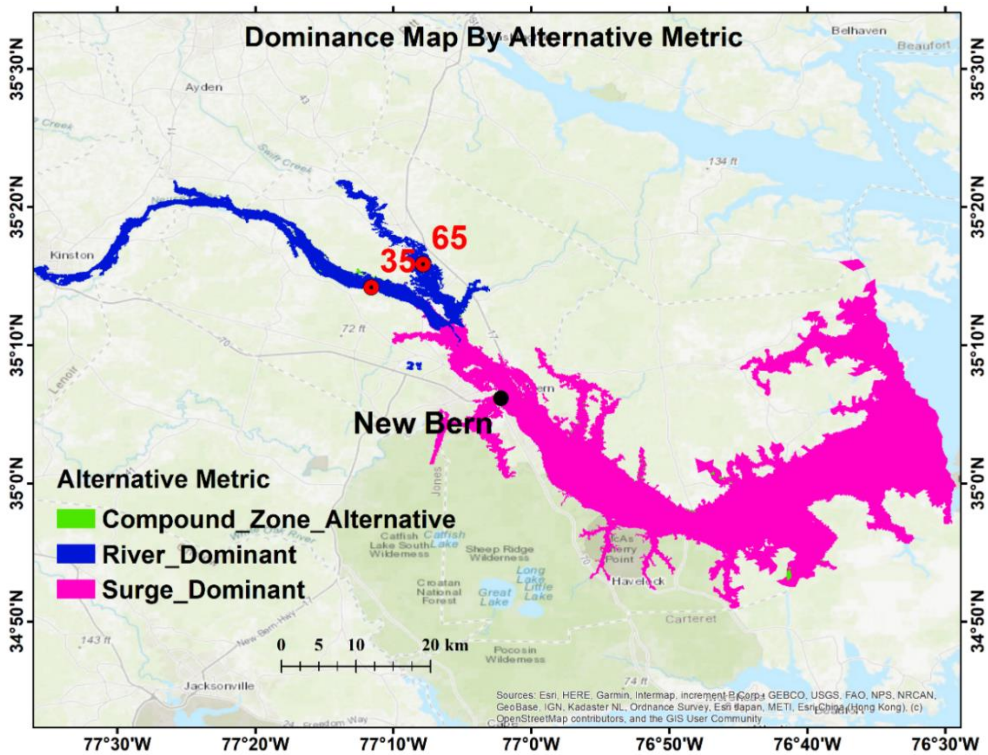

Fig. 3.4: Dominance map generated using baseline (a) and alternative metric (b)

To capture the compound zone more realistically, we readjusted the threshold values. We generated another dominance map using the alternative metric with the new threshold values of the compound ratio 5% and 95%. The dominance map is presented in Fig. 3.6 and shows that station ID 65 is riverine dominant, whereas ID 35 is in the compound zone. It is noticeable that if we consider the timing of the peak (Fig. 3.5), the compound zone varies, more logically identifying the compound location than the baseline metric with a 20% and 80 % compound ratio. The area calculated using the baseline metric is 78 km^2 for the compounding ratio of 20% and 80%. In contrast, the compound area calculated by the alternative metric is 85 km^2 for the compounding ratio of 5% and 95%.

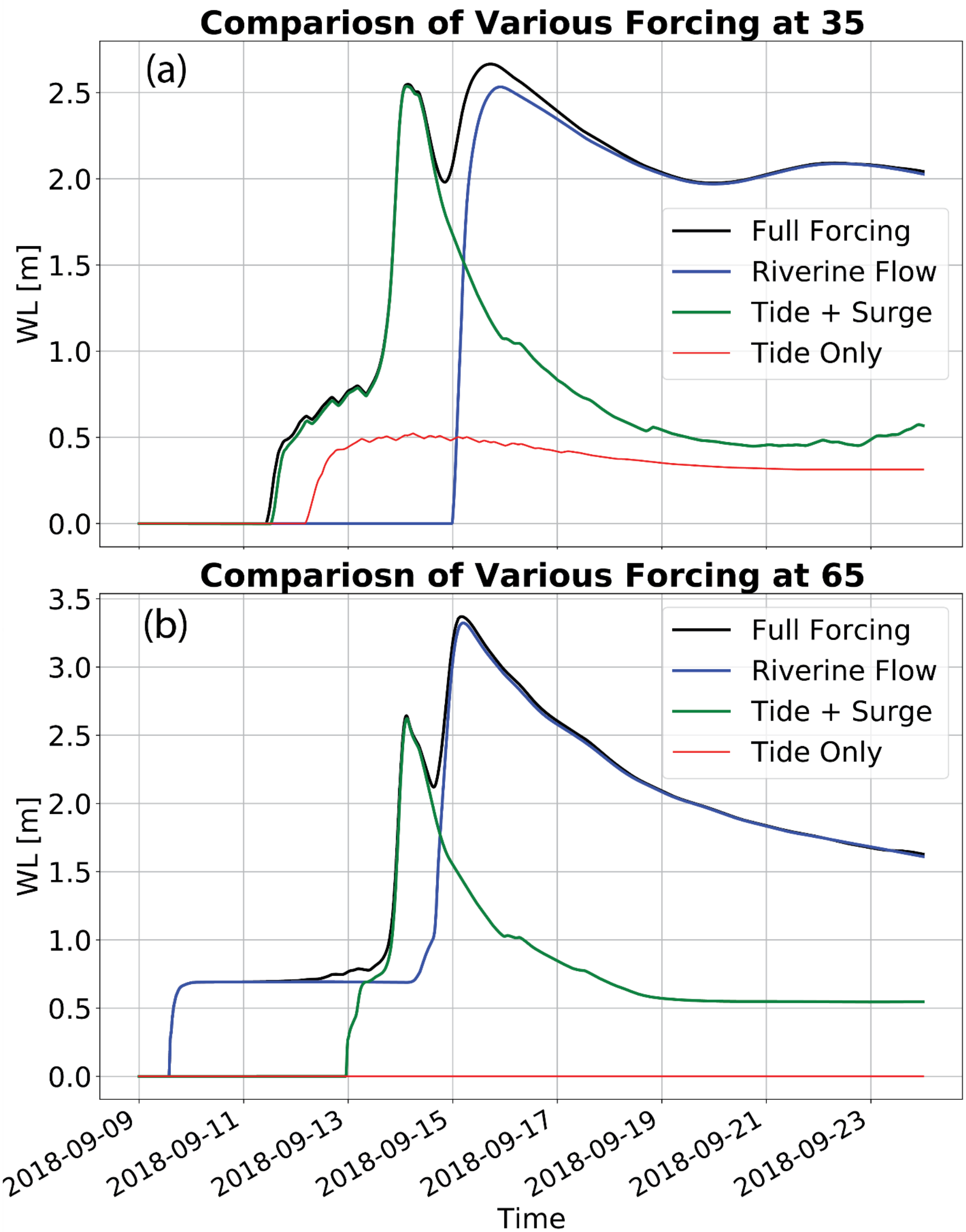

Fig. 3.5: Comparison of water level contributions from each forcing

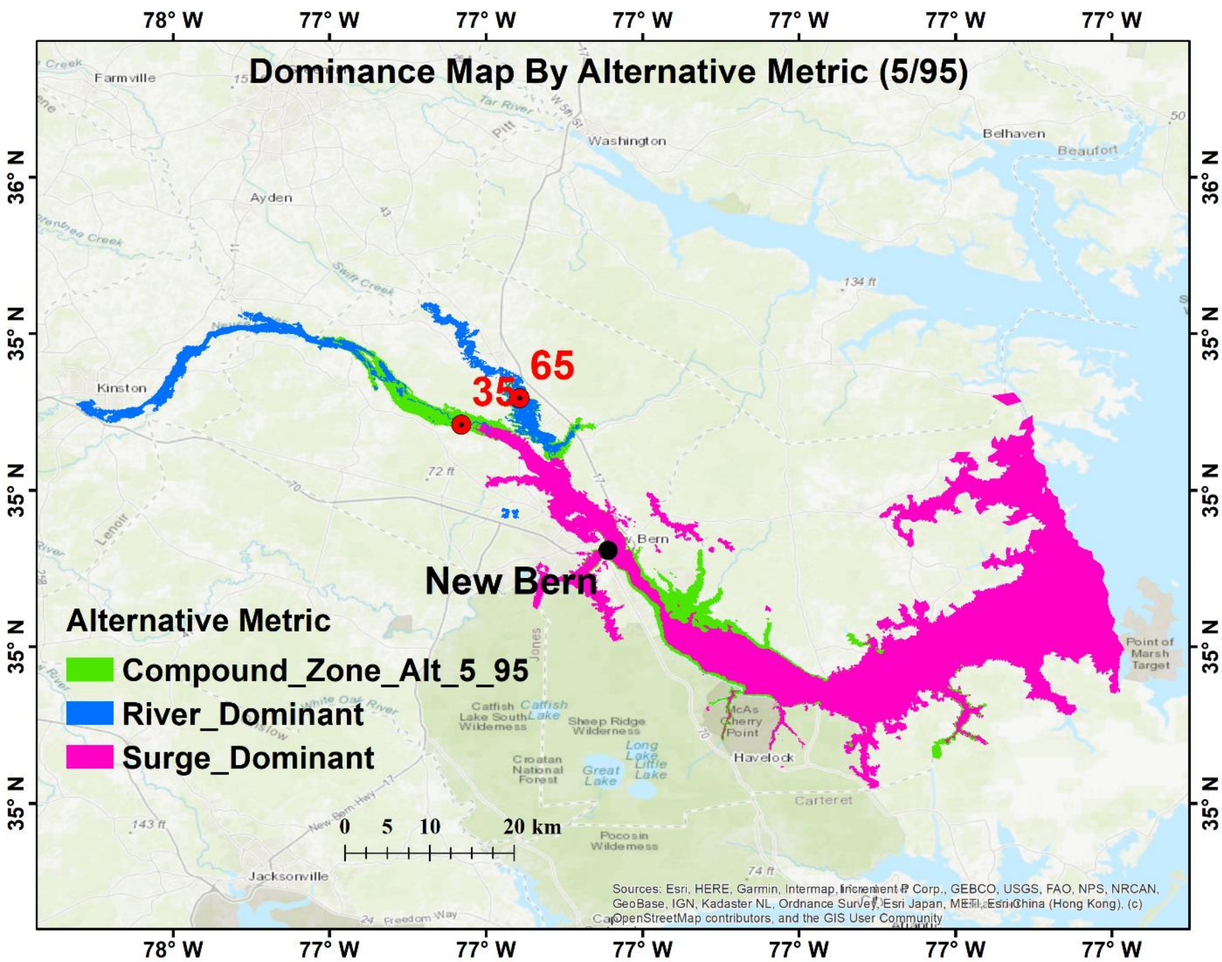

Fig. 3.6: Dominance map generated by alternative metric using a compound ratio of 5 % and 95%

Therefore, a change in the metric definition that determines the compound zone plays a vital role in the regions with consistent compound flooding. So, the alternative metric is more conservative than the baseline. Managing flood hazards using a more conservative estimation will reduce the risk of property damage and save lives. Hence, the compound zone defined by the alternative metric is recommended for coastal risk management.

3.3.3 Effect of Land Surface Control

In this study, we use the term "land surface control" to identify the potential locations for salt marsh along the flood plains of Neuse River and Swift Creeks and control their intensity by roughness coefficients to assess the impact on the compound flooding. We have used three different values of Manning's roughness, such as 0.050, 0.075, and 0.10 (Chow, 1959; George J. Arcement, JR., 1989), in place of the calibrated model roughness. We identify the presence of marshlands at 65 locations where the salt marsh and other vegetation are present. The calibrated roughness values are presented in Table 3.3. However, the actual values for marshland are much higher than this range (Al-Asadi and Duan, 2017). We gradually increase the intensities to learn the impact of the presence of marshlands as a land surface control on compound flooding. The location of marshlands along the Neuse River and Swift Creek is shown in Fig.3.7.

Table 3.3: Calibrated model roughness based on the land cover type

Land cover type	Calibrated Manning's n
Ocean	0.012
Shallow water	0.018
Shorelines	0.02
Flood plain	0.023
Overland	0.025

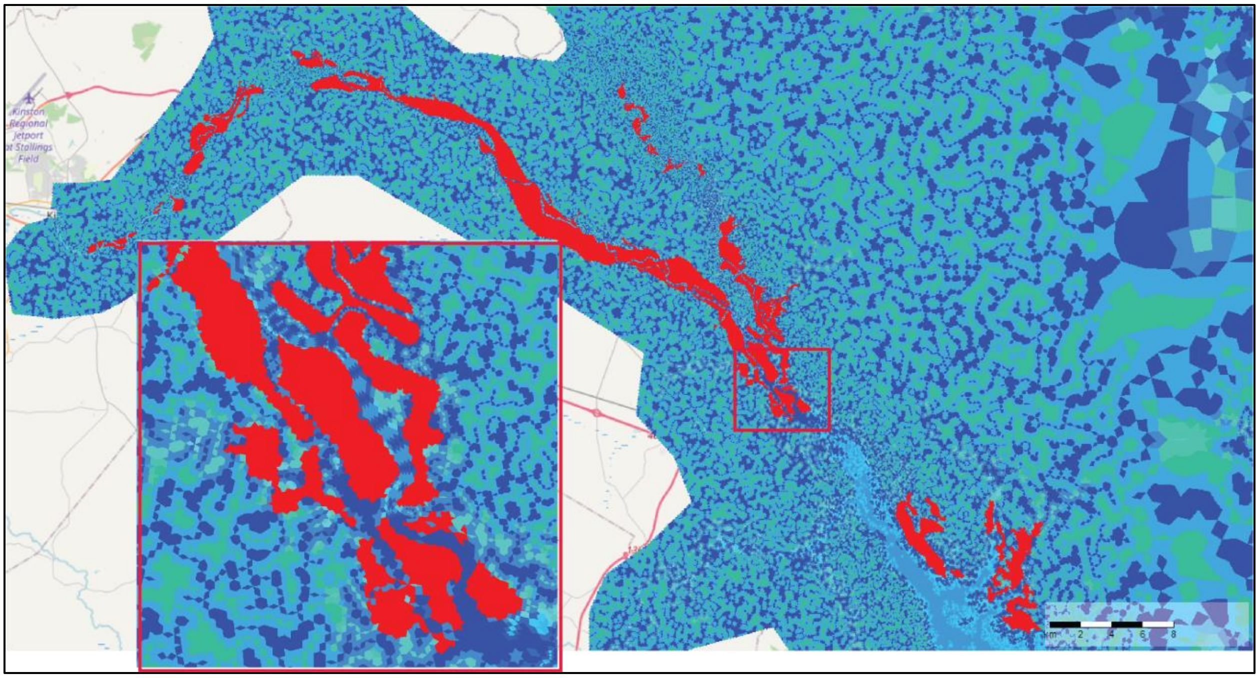

Fig. 3.7: Map showing the locations of the presence of marshlands along the Neuse River and Swift Creek

To estimate the impact of the presence of marshland as a land surface control, we represent the marshlands as a roughness ranging from 0.050 to 0.10 (Fig. 3.7). Using these roughness values, we conducted the sensitivity analysis for each condition. We generated the dominance map to identify the location with the significant compounding effect. The dominance maps for various roughness factors are shown in Fig. 3.8, along with the calibrated condition (Fig.3.8-a). It is noticeable that the compound zone has shifted downstream from the baseline location, as the marshlands are a hindrance to the flow. During the high flow, water flows over the flood plain, resulting in slow entry of the surging water from the ocean. Therefore, the total compound zone is reduced because of the presence of the marshlands. The calculated area of the marshlands using the roughness factor of 0.05 is 62 km^2 (Fig. 3.8-a), whereas the area from the baseline simulation is 85 km^2. 26% reduction in the compound zone, and the location shifted downstream. Likewise, we simulated the model using other roughness values of 0.075 and 0.10 to learn the reduction trend. The dominance maps for these two roughness conditions are shown in Fig. 3.8-c and Fig.3.8-

d. The maximum reduction in the compound zone is 35 % for the roughness value of 0.10. Table 3.4 presents the summary of the area reduction for each case of land surface controls.

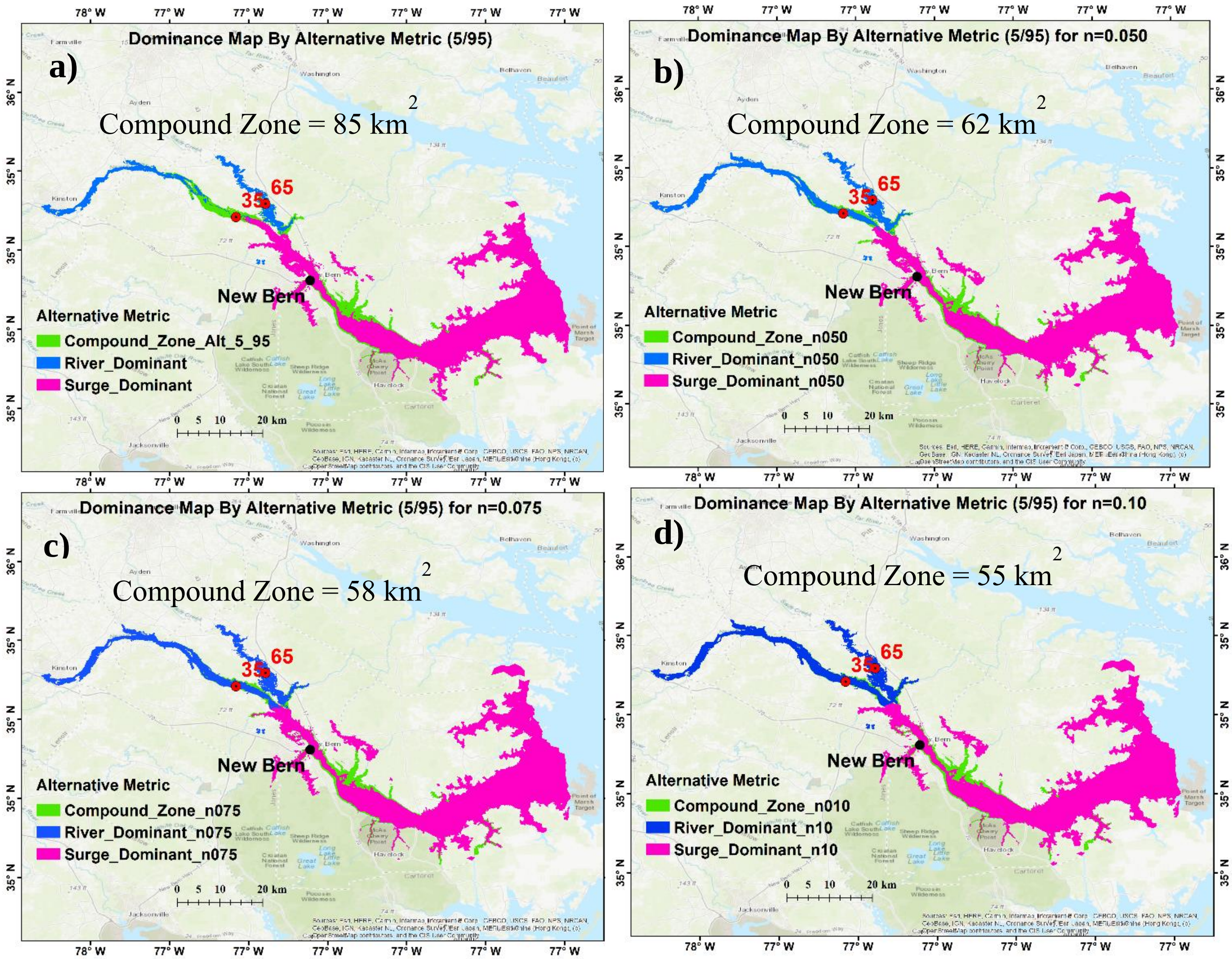

Fig. 3.8: Dominance map generated by alternative metric; (a) for calibrated condition (b) for n = 0.050, (c) for n = 0.075, and (d) for n = 0.10

Table 3.4: Calibrated model roughness based on the land cover type

Run Conditions	Area of Compound Zone(km^2)	Change in Area (%)
Baseline	85	-
LSC (n=0.050)	62	-26%
LSC (n=0.075)	58	-32%
LSC (n=0.10)	55	-35%

3.4 DISCUSSIONS

Coastal flooding during tropical storm landfalls often arises from a combination of flood drivers, including storm surges, heavy rainfall, and fluvial inflow. In some instances, the magnitude of flooding can be shaped by the compounding effects that are determined mainly by the dynamic interactions among the drivers. However, many conspicuous knowledge gaps remain in our understanding of the causes of compound effects as well as their impacts. These concern physical processes that give rise to the compound effects and metric for quantifying the effects of it that will faithfully capture the interactions among forcings. In this study, we propose an alternative metric for measuring the intensity of interactions among drivers of coastal flooding during major TC landfalls. And we re-assess the compound effects through a landfalling hurricane event, namely Hurricane Florence of 2018, over North Carolina.

The baseline metric ratio is not sufficient in terms of the dynamic interactions among the processes, such as rainfall-run, riverine, tide, and surge, resulting in minor impacts produced by the forcings. Hence the areal extent is lower than that estimated by alternative metric. Moreover, the threshold ratio (i.e., 20% and 80%) is also low enough to define the compound zone accurately. In contrast, the alternative metric measures changes to inundation depth within time windows surrounding the event maxima, thus accounting for timing differences among peaks driven by disparate forcings, resulting in conservatively assessing the compound zone and its distribution.

The sensitivity of the threshold ratio is low in the baseline metric; changing the ratio (from 20%, 80%) to 5% and 95% does not demonstrate a noticeable change in the compound zone as it does not account for the timing differences among peaks produced by individual forcing. However, the threshold in the alternative metric is very sensitive to the compound zone; changing the ratio to 5% and 95% produces more regions with consistently significant compound zones. As the alternative metric accounts for the timing differences among the peaks of the individual forcing, it can capture the dynamic interactions between processes. Hence, changing the threshold a little bit is reflected in the compound zone and makes this metric more robust to identify the regions with compound zone induced by tropical storms.

The application of alternative metric to assess the impact of marshlands' presence is trustworthy for the above-mentioned reasons. However, this assessment was conducted by generalizing the roughness of marshlands, meaning that we only assigned a single value for all locations where we found the presence of marshlands and other vegetation as well. For this reason, we used lower values than the representative values of roughness for marshlands. This may underestimate the impact, but it still can demonstrate the impact of an increase in the intensity of marshlands on compound flooding.

3.5 CONCLUSIONS

Currently, coastal flooding has become one of the main natural disasters, occurring more frequently than ever before, and storm surges, high tides, heavy rainfall, and high riverine flow cause flooding. While many attempts have been made to characterize and measure the compound effects during TC-driven floods, most relied on rather simplistic metrics that do not account for timing lag among forcings and, as a result, cannot discern dynamic interactions. Therefore, this study proposes and examines an alternative metric for identifying compound effects that focuses on the physical interactions among drivers. This alternative metric measures changes to inundation depth within time windows surrounding the event maxima, thus accounting for timing differences among peaks driven by disparate forcings. The alternative metric we introduced here in this study is important to characterize the drivers' dynamic interaction and identify the compound zone.

In addition to the alternative metric, we assess the impacts of land surface control on the intensity and location of compound flooding. To do so, we identified the locations where marshlands are present and assigned a range of roughness values to study the impact on compound flooding using the alternative metric. The specific outcomes are as follows:

i) The baseline metric is insufficient to dynamically interact with the processes, such as riverine flow, rainfall-runoff, and surge. Therefore the actual impact of forcing is minor. Besides, the threshold ratio of 20% and 80% are pretty low in terms of defining compound zone. However, the effect of threshold in baseline metric is not prominent in terms of areal extent but has an impact on the spatial distribution.

ii) The alternative metric measures change to inundation depth within time windows surrounding the event maxima, thus accounting for timing differences among peaks driven by disparate forcings. Therefore, this metric is important to characterize the dynamic interactions between forcing to identify the compound zone by using it.

iii) The presence of marshland impacts the compound zone, and the compound area was reduced by 35 % for the highest intensity of marshland. This reduction was estimated based on the alternative metric. In addition, the location of dynamic interaction translated to downstream sites, resulting in shifting the compound zone to a downstream location.

This study was limited to applying the alternative metric to one tropical storm (i.e., Florence). However, future research should include applying this metric to other tropical storms with various structures. In addition, we limited this study to the generalized marshland conditions; however, extending the marshland upstream and downstream locations and studying their impact on compound flooding is a topic for future research. Moreover, the realistic values of the salt marsh or marshlands for the 2D model are larger than those we used here. Therefore, the prospective study should include higher values with more specific locations of the marshlands, and more specific vegetation types should be assigned. Using the latest land use map will be more realistic in identifying the location of the vegetation cover along the banks of the Neuse River and Swift Creek.

Chapter 4 The Intensity and Location of Compound Flooding Vary with Storm Structures

ABSTRACT

Flooding in coastal regions originates either from surge-dominated, rainfall-dominated events, or a combination of them, causing massive compounding over the area, especially upstream watersheds. The intensity and location of compound flooding also vary with the storm structures. In this study, we have investigated three contrasting storm events over the Amite River watershed in Louisiana, including Lake Moureapeas and Lake Poncertrain, that contributed to compound flooding. This study aims to identify how different storm structures over the region contribute to compound flooding and how the intensity and location vary upstream and downstream of the Amite River. To this end, we extensively calibrate an integrated modeling framework in simulating compound flooding effects resulting from rainfall runoff, astronomical tides, storm surges, and atmospheric forcing within the Lakes Maurepas and Pontchartrain drainage basins. The calibration was performed on two contrasting events: a rainfall-dominated flood event in 2016 and a surge-dominated (i.e., Hurricane Isaac) event in 2012. Then the resulting model was utilized for Hurricane Ida in 2021 to ascertain the extent of the compound zone. Our intermediate results suggest that surge-dominated events only generate floods within the transition zones, whereas rainfall-dominated events contribute to watershed flooding. However, the study reveals that a surge event with heavy rainfall is the actual cause of compound flooding. The location and intensity of compound flooding vary upstream and downstream. This innovative study suggests that a coupled model can be used for operational use for predicting compound flooding in coastal areas as the model reduces computational time by avoiding the complexity of implementing different modeling frameworks separately with multiple parameter estimations. Hence, the outcome of this study will help policymakers take prompt and informed actions during storm events.

Keywords: Delft3D-FM, storm surge, NWM , compound flooding

4.1 INTRODUCTION

Flooding can range from a minor inconvenience to a catastrophic event. This is the case, particularly in low-lying, densely populated coastal regions and deltas that are subject to multiple flooding threats from various sources, including oceanic sources such as tropical storms, riverine flow, and rainfall. The frequency of nuisance level flooding along the coasts of the US has increased due to sea level rise (SLR) and is anticipated to continue this trend (Moftakhari *et al.*, 2015b), translating to a higher baseline rate of flooding when taking into account other contributing factors found in coastal environments. Hurricanes account for 7 of the top 10 most costly climate disasters in the United States, according to NOAA's National Climatic Data Center (NOAA/NCEI-2, 2021). Flooding represents the biggest threat contributing to the loss of life during a hurricane (Blake and Rappaport, 2001), which is further exacerbated by demographic shifts relocating into more storm-prone areas (Easterling *et al.*, 2000). The damage, duration, and extent of flooding can be further magnified by conditions that lead to compound flooding, such as those observed in tropical storms and hurricanes.

Compound flooding (CF) events are defined as a "combination of multiple drivers and hazards that contributes to societal or environmental risk" (Zscheischler *et al.*, 2018). The effects of compound flooding are most pronounced in the coastal transition zone, which varies for individual locations based on a myriad of factors including but not limited to local topography and bathymetry, human development and land use, and type of storm event. Driving characteristics of compound flooding events typically include storm surge (a combination of astronomical tidal effects and low-pressure atmospheric effects such as those from tropical storms), pluvial contributions (resulting rainfall from storms), and fluvial contributions (riverine flow from the watershed) (Ye, Zhang, *et al.*, 2020). These flood drivers may also include wind forcing that can extend the reach of storm surge further inland for longer durations than would otherwise be observed in the absence of wind effects, as well as magnify storm surge through the addition of wind setup in coasts with enough fetch for wind setup to develop. Moreover, wave contributions in the form of wave setup may also contribute to the magnification of storm surge as it approaches the coastline. Lastly, sea level rise is a long-term observed trend that is anticipated to exacerbate the frequency and duration of compound flooding events as storms become more frequent and "wetter" (increased rainfall contributions) (Bevacqua *et al.*, 2019; Hall and Kossin, 2019; Wahl *et al.*, 2015).

Accounting for the above is an ongoing challenge in coastal-inland hydrologic modeling. Developing a better understanding of the physics at work and the resulting interactions may significantly contribute to improved modeling and predictive analysis for events with the potential for compound flooding impacts on communities. To better understand compound flooding drivers and their impact on resulting inundation, this study aims to generate a calibrated model on one such event (Hurricane Isaac, 2012) that is complemented with various observational data points in the Amite River Basin. By applying this model and iteratively removing, shifting, and magnifying individual driver contributions (storm surge, rainfall, wind, and pressure) applied to the study site, this study seeks to quantify the drivers with the immense impact on inundation and recommend these and sensing and modeling priorities to the National Water Center (NWC) for improved predictive modeling for future application.

Multiple studies have implemented various numerical simulations programs and coupled systems of numerical simulations programs to represent observed and hypothetically generated events that generate compound flooding inundation to better understand and characterize the mechanisms and physics at work. An important building block towards this level of analysis is correctly modeling the propagation of tidal signal and storm surge into estuarine environments (Bilskie *et al.*, 2019; Herdman *et al.*, 2018; Lawler *et al.*, 2016; Spicer *et al.*, 2019). Bacopolous et al. (Bacopoulos *et al.*, 2017) demonstrated the importance of incorporating watershed runoff as a boundary condition to fully capture peak surge with integrated hydrologic-hydrodynamic modeling of compound flooding events. Several studies augment ADCIRC with a coupled hydrologic model to account for rainfall-runoff, simulate compound flooding events, and determine how storm surge and flood flows interact (Bakhtyar *et al.*, 2020; Bilskie and Hagen, 2018; Gori *et al.*, 2020; Loveland *et al.*, 2021). Bilskie and Hagen apply this method to a similar study domain as this study examines. Other studies use various model combinations, either omitting or parameterizing rainfall runoff, to describe the interactions between storm surge and river flood flows (Hasan Tanim and Goharian, 2021; Kumbier *et al.*, 2018; Valle-Levinson *et al.*, 2020). To this research team's knowledge, no studies have simulated the combined effects of rainfall runoff, riverine flow, tidal surge, spatially-varied wind, and spatially-varied pressure resolved within a single modeling program (D-Flow FM) for the Amite River basin. In this study, the respective contributions of each of the flood drivers were assessed and compared with the findings of Bilskie and Hagen to refine the understanding of compound flooding vulnerability in the Amite River basin to Lake Pontchartrain and its sensitivity to the various drivers.

The storm structure plays a vital role in demonstrating compounding effects. Because the behavior of a surge-dominated event is different from that of a rainfall-dominated event, both have separate dominant zones. Our hypothesis is the purely surge-dominated hurricane event is responsible for flooding in the low-lying coastal areas, whereas the rainfall-dominated flood event causes massive floods in the watersheds. However, when both contributions are present in an event, there is a high chance of developing compound zones, where flood is more severe as it added the peaks from both contributions (i.e., surges and riverine flows). Therefore, it is necessary to study the effect of storm structures on the intensity and location of compound flooding.

This study aims to identify the impacts of different storm structures on the intensity and location of compound flooding over the study region (i.e., Amite River Basin). To this end, we extensively calibrate an integrated modeling framework in simulating compound flooding effects resulting from rainfall runoff, astronomical tides, storm surges, and atmospheric forcing within the Lakes Maurepas and Pontchartrain drainage basins. The calibration was performed on two contrasting events: a rainfall-dominated flood event in 2016 and a surge-dominated (i.e., Hurricane Isaac) event in 2012. Then the resulting model was utilized for Hurricane Ida in 2021 to ascertain the extent of the compound zone.

The remainder of this article is structured as follows. Section 2 provides descriptions of the material and methods, including selecting appropriate storm events for the study region and calibration matrices. The objectives of this study are discussed in Section 3 (i.e., Results), where the impact of various storm structures on compound flooding is identified based. Section 4 discusses the findings of the study in detail concerning the objectives, and Section 5 summarizes the outcomes and offers recommendations for future works.

4.2 MATERIALS AND METHODS

4.2.1 Study Area

The study area, known as the Amite River basin, is located in Louisiana, draining into the Gulf of Mexico through Lake Maurepas and Lake Pontchartrain (Fig. 4.1). We extended the Amite watershed further downstream as it empties into Lakes Maurepas and Pontchartrain. Geographically, the study area is bounded on the south and southwest by the Mississippi River, tracing the levees and high ground of the banks so as to assume a "no-flow" boundary condition with the Mississippi River. The western boundary continues to follow the USGS-designated Amite watershed, including the Amite and Comite Rivers. The eastern boundary line traces the USGS-designated Tangipahoa watershed until it intersects with the periphery buffer around Lake Pontchartrain.

Hydrologically, the study area is comprised of a series of USGS-designated hydrologic units draining into Lake Maurepas and Lake Pontchartrain, including the Amite (i.e., HUC 08070202), Tickfaw (i.e., HUC 08070203), Tangipahoa (i.e., HUC 08070205), Lake Maurepas (i.e., HUC 08070204), and Lake Pontchartrain (i.e., HUC 08090202). An open boundary is included, generally spanning northeast to southwest through the Eastern Louisiana Coastal (i.e., HUC 08090203). Additionally, point sources from neighboring HUCs feeding into the domain of the model are included and represent the contributions from Liberty Bayou-Tchefuncta (i.e., HUC 08090201) and Lower Pearl (i.e., HUC 03180004) (USDA Forest Service Southern Research Station). Lake Maurepas drains into Lake Pontchartrain through a Pass Manchac, a 10-km long canal approximately 400 m wide and 12 m deep. Lake Pontchartrain flows into the Gulf of Mexico through the 15 km-long Rigolets tidal channel (Bilskie and Hagen, 2018), Chef Menteur, and an artificial Inner Harbor Navigation Canal. Lake Pontchartrain experiences a diurnal tide with a mean range of 11 cm through the three narrow tidal passes (Chao *et al.*, 2012). The northeastern periphery of Lake Pontchartrain is characterized as a marshland extending as far as 10 km inland. The land surrounding Lake Maurepas and the northwestern boundary of Lake Pontchartrain is primarily swamped with marshland interspersed. This swamp branches outward from Lake Maurepas, tracing the contributing waterways as far as 30 km inland (Keddy *et al.*, 2007). The southern half of the study area is predominantly low-lying flat lands comprised of alluvial deposits from the Mississippi River Delta. Further north up the study area, elevations gradually rise to values over 130 m (USGS).

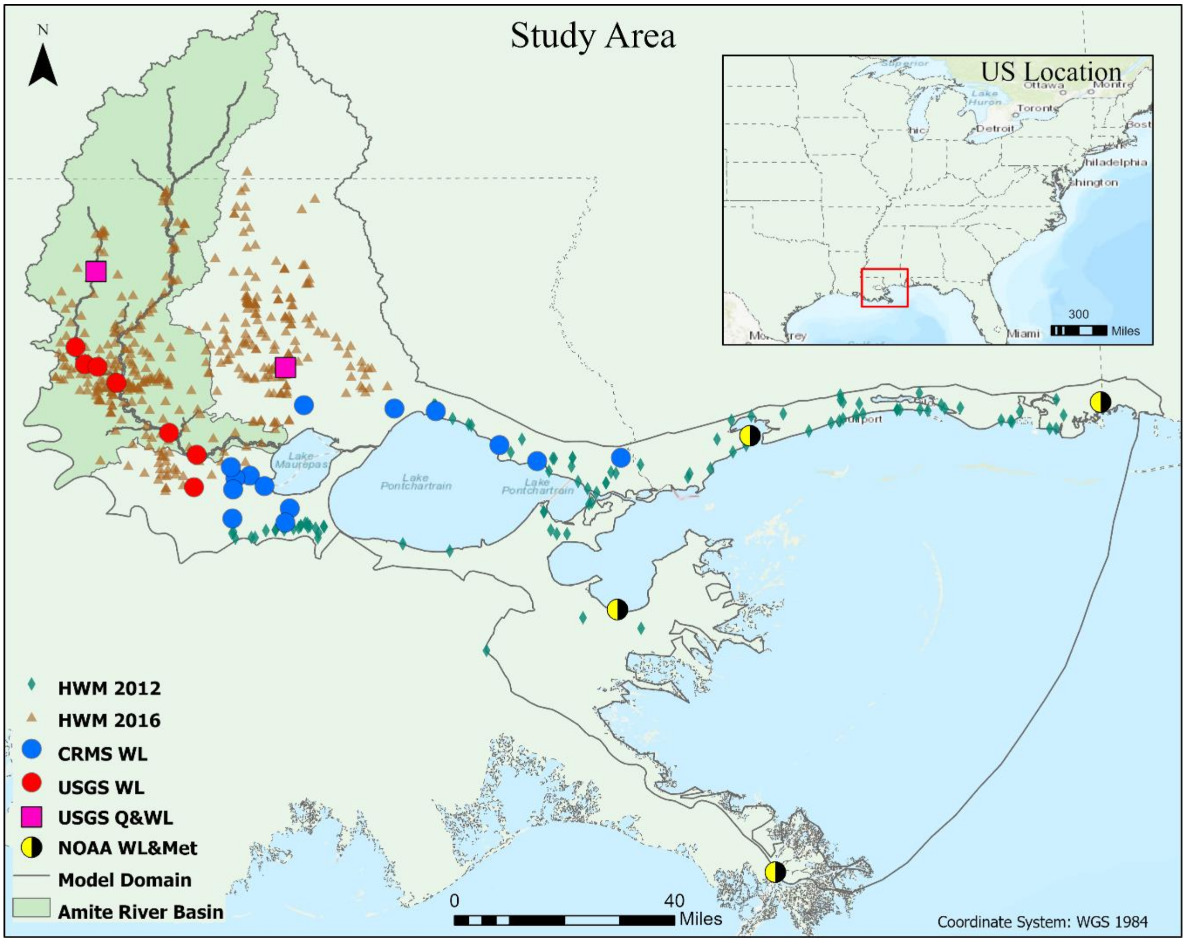

Fig. 4.1: Study area map of Amite River Basin, Louisiana, and Mississippi, USA

4.2.2 Selection of Historical Events

4.2.2.1 Event-A: Hurricane Isaac (2012)

Hurricane Isaac originated as a tropical wave moving off the coast of Africa on August 16th, 2012, tracking across the Atlantic until it entered the southeastern Gulf of Mexico early on August 27th. Isaac reached hurricane strength around 1200 UTC on August 28th, approximately 75 nautical miles southeast of the mouth of the Mississippi River, where it slowed down translation speed considerably and prolonged the Gulf coast's exposure to strong winds, storm surge, and heavy rains until it finally made landfall on the coast of Louisiana around 0000 UTC on August 29th with windspeeds of 70 knots. Isaac continued pushing further inland, reducing in strength to tropical depression around 0000 UTC on August 31st in southern Arkansas and dissipating after 0600 UTC on September 01st southwest of Jefferson City, Missouri (Berg, 2013).

Storm surge recorded from the event by a NOS tide gauge was 11.03 ft over normal tide at Shell Beach, Louisiana, with storm tide estimated to have inundated most coastward parishes by as much as 10-17 ft. The strong wind fields and storm surge even resulted in USGS observation of the Mississippi River flowing backward for almost 24 hours at Belle Chasse, Louisiana. Southeastern Louisiana also received more than 20 inches of rain (i.e., New Orleans, Louisiana), resulting in flash and river flooding. All told, five deaths were reported in the United States, and damages were estimated at $2.35 billion (Berg, 2013). Hurricane Isaac was chosen as a calibration event for the model because it featured characteristics of storm surge and pluvial flooding across the study area. Utilizing a wealth of USGS, CRMS, and NOAA gauge observations available throughout the aforementioned HUCs during this event, this case allowed leveraging the model's ability to resolve wind, pressure, and hydrologic forcing simulating the event. Accurately representing observations from observed forcing from the compound flooding event instills confidence that magnifying or removing the drivers in later research stages will accurately reflect the hypothetical results.

4.2.2.2 Event-B: 2016 Flood

A slow-moving area of low pressure with high atmospheric moisture released heavy rainfall over Louisiana and southwestern Mississippi throughout August 11-14, 2016. It resulted in at least 13 fatalities and an estimated $10 billion in damages due to flash flooding and record river flooding.

The heaviest rainfall was observed east of Baton Rouge. New record peaks for streamflow were encountered at 10 USGS streamflow-gaging stations as this storm recorded more than 31 inches of rain over 48 hours in several stream basins. According to NOAA, this event topped the 0.2% annual exceedance probability (Watson *et al.*, 2017). The flood event of 2016 was chosen as another calibration event for the model because it was virtually dominated by pluvial contributions (compared to storm surge contributions) across the study area. Utilizing a wealth of USGS gauge observations available throughout the aforementioned HUCs during this event, this case allowed calibrating for hydrologic losses through scaling rain input that would otherwise not be calculated by the processes within the model.

4.2.2.3 Event-C: Hurricane Ida (2021)

Hurricane Ida (2021), a category-4 Atlantic hurricane with a 1-minute sustained highest wind speed of 240 km/h and more than 3 inches of rain an hour, made landfall in Louisiana on 29th August 2021, causing massive damage to lives and properties (Beven *et al.*, 2021). In addition, due to the presence of marshlands and the flat topography of southern Louisiana, hurricane Ida retained its intensity for a more extended period, exacerbating the flooding caused by the combined effect of rainfall and surges in that region. Mainly two factors contributed to Ida's ample rain. First, tropical moisture interacted with developing warm and cold fronts. Second, heavy precipitation increases as the climate become warmer, especially in the central and eastern US. Therefore, this storm event is advantageous in studying the compound effect. In this study, we utilized the wind and pressure fields of Hurricane Ida to understand the impact of storm structures on the intensity of compound flooding.

4.2.3 Data Collection

We collected data from national and regional sources to drive the Delft3D-FM model for various storm events. The input data requirements and source information are listed in Table 4.1.

Table 4.1: List data and sources

Type	Dataset Source	Resolution	Unit	Datum
Rainfall	Radar, QPE	1 hour, 1 km	mm	N/A
Water Level	USGS, CRMS, NOAA, HWM	15/60 min	m	NAVD 88
Discharge	USGS	30 min	cms	N/A
Topobathy	CoNED, USGS DEM	30 m	m	NAVD 88
Wind	NCAR, NOAA, HWRF	40 km, 6 & 1/6 hour	m/s	10 m abv. ground
Pressure	NCAR, NOAA, HWRF	40 km, 6 & 1/6 hour	Pa	PRMSL
Open coastal boundary	Regional Ocean Model	1 hour	m	NAVD 88
Boundary Inflow	USGS	30 min	m^3/s	N/A
Roughness	ADCIRC	Varies	-	N/A

4.2.4 Description of Model Physics: Hydrodynamic Model

The Delft3D-FM suite of models is a fully integrated software suite for 2-dimensional (2D) and 3-dimensional (3D) computations for the coastal, river, and estuarine areas. It is a depth-averaging model developed by Deltares (2014). In this study, we adopted the 2D version of Delft3D-FM, where we implemented the model as the barotropic condition. The hydrodynamic module (i.e., Delft3D-FLOW) and the wave module (i.e., Delft3D- WAVE) are responsible for the short-wave generation and propagation in the nearshore areas. The two-way coupling between both modules allows for taking the effect of waves on currents into account (Delft Hydraulics, 1999). In this study, we excluded the wave module to avoid complexity due to limited access to computational facilities and the restricted duration of the study period. Sometimes, the impacts of nearshore waves often muted due to the sheltering effects of the Barrier Island (Ye, Huang, *et al.*, 2020). This research team will use the wave model in future studies to test the impact of the wave during a storm surge event.

4.2.5 Model Configuration

We merged several datasets to create good-quality bathymetric and topographic data for this study. The Coastal National Elevation Database (CoNED), a combination of bel level and DEM, has been used to provide the bathymetric data of the open oceans. In contrast, LiDAR data has been utilized to enhance the representation of the bathymetry of the Amite River and the upstream watersheds. Fig. 4.2 presents the merged topobathy, whereas Fig. 4.3 shows the unstructured grid of the hydrodynamic model extending from about latitude 28.0° N and longitude 92.0° W to latitude 32° N and longitude 87.0° W. The total elements and nodes are around 0.48 million and 0.26 million, respectively. Since many narrow, meandering rivers cover the study area, we utilize the flexibility of the model mesh known as flexible mesh. To optimize the computational time, we employed the finer resolution for the streams, whereas the coarse one for large water bodies. We resolve the Amite River and its tributaries by rectangular mesh ranging from 50 m in the vicinity of the Amite River to 5 m in other streams. However, the overland, lakes, and bay are resolved by triangular meshes ranging from 3000 m, at the very downstream of the model domain, to 250 m at the lakes.

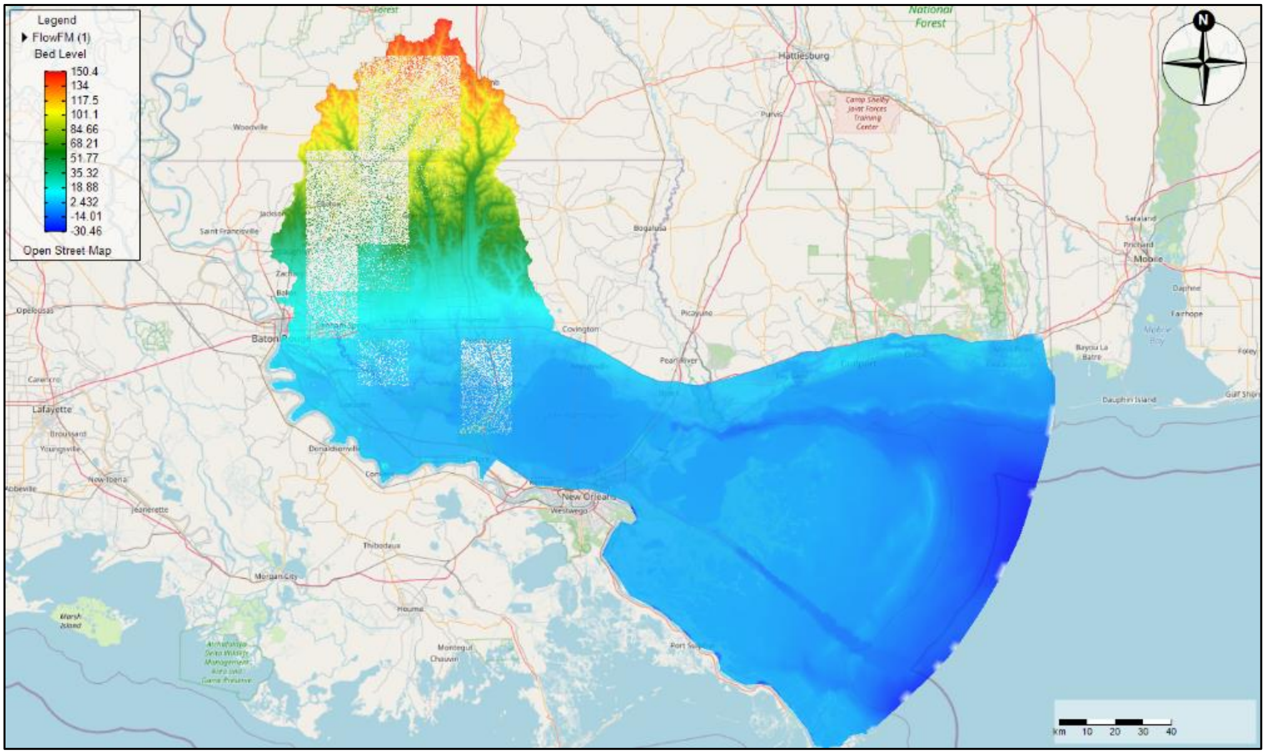

Fig. 4.2: Topobathy of the Model

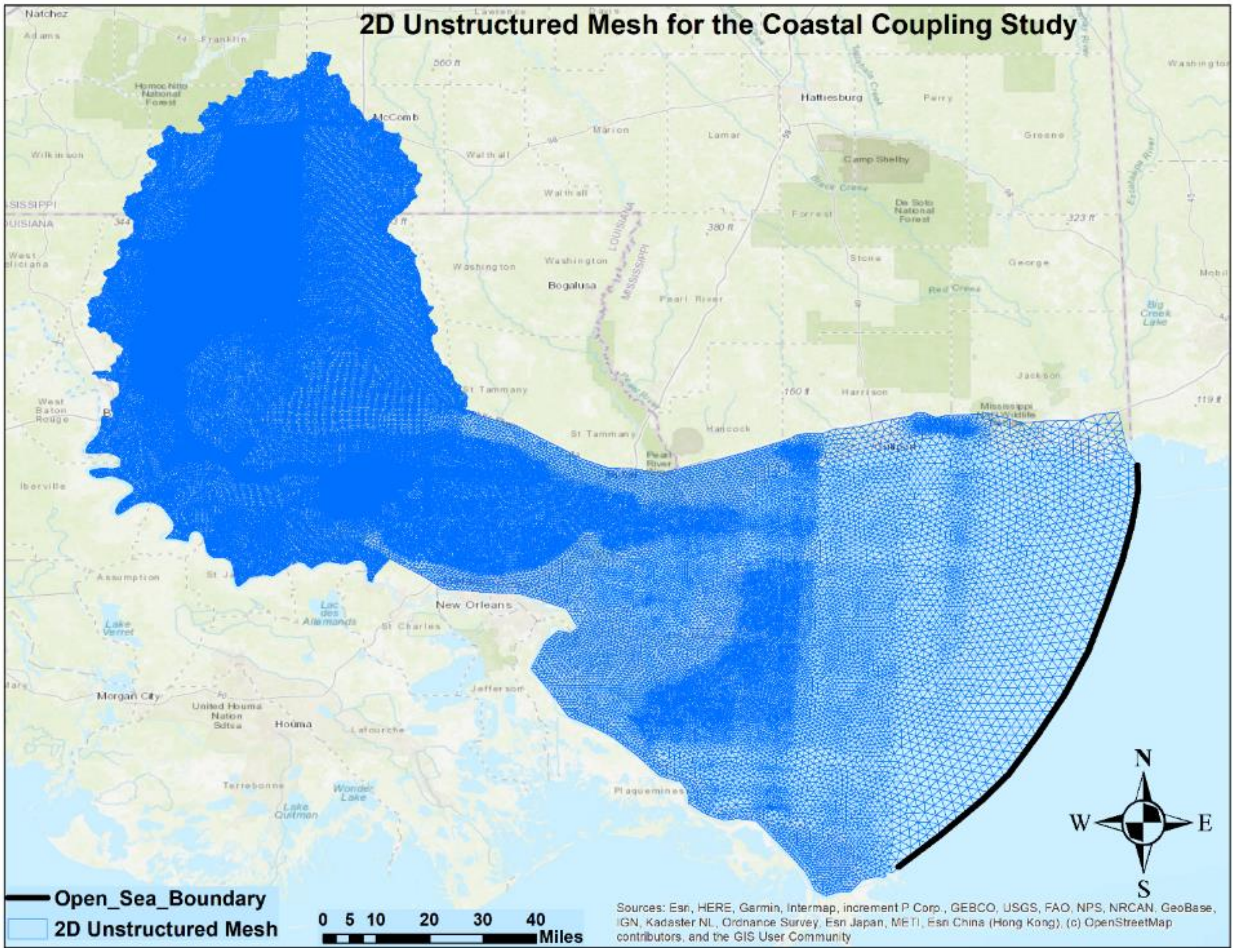

Fig. 4.3: 2D-Unstructured Mesh for Delft3D-FM model

As we know, precipitation is one of the main drivers for most hydrologic models, and this one is no exception, particularly for the rainfall-dominated 2016 Flood event. We generated space-varying rainfall fields, known as rain-on-grid, for each event to account for the spatially-variant nature of precipitation during storm events. We adopted the space-varying roughness from an ADCIRC model, and the rest was generated using the land use data. The mesh resolution ranges from 3 km in the nearshore to 10-m for the upstream channels. The courant number was fixed at 0.70 with user time steps of 30 seconds and a maximum time step of 600 seconds. The nodal update interval was also set at 30 seconds. The initial water level was fixed at mean sea level, and the water density was considered 1025 kg/m^3 for saline water. Additionally, the uniform horizontal eddy viscosity and diffusivity of 1.0 m^2/s and 1.0 m^2/s were used. For the wind drag coefficient type, we implemented 2-break points based on Smith & Banks; the values are 0.000063 and 0.00723 for the break-points wind speed of 0 and 100 m/s, respectively. The dry cell threshold was fixed at 0.01 m. The default values were used for all other parameters.

4.2.6 Boundary Conditions

The integrated hydrodynamic model requires hydrological boundaries on the land, tidal boundaries on the ocean, and atmospheric and meteorological boundary conditions to drive the model. In this study, we adopted riverine flow from USGS at the land boundary, the tidal water level at the ocean extracted from a larger coastal Delft3D model (Hu *et al.*, 2015), wind and pressure fields as atmospheric forcing, and precipitation from multiple sources as meteorological boundary conditions.

The discharges from the upstream of the model domain and surface runoff due to the heavy rainfall caused by a storm event need to be considered in the hydrodynamic simulation process to improve the accuracy of the estimation of overland flooding. Because the torrential rain partially contributed to the flooding process (Lee *et al.*, 2019). The available flows have been incorporated into the model as point sources, and there are 8-point sources with varying magnitudes. Ocean tides result from the sun's and moon's gravitational attraction on the Earth's oceans (Sumich, 1996). So, the water level change due to the astronomical tide is a crucial factor contributing to coastal inundation during a storm. Coastal flooding depends on the superimposition of tidal water with the surging water. If the storm surge occurs during low tide, the damage can be relatively small, whereas catastrophic damage will occur if the surge comes during high tide. We selected three different storms, and one was rainfall-dominated in 2016. This flood event was mainly driven by heavy torrential rainfall. Hence, we implement the rain-on-grid scheme using a rectangular 1000 m x 1000 m structured grid. Moreover, space-varying wind and pressure fields at the nodes of the model mesh are also used.

4.2.7 Sensitivity Analysis

The sensitivity analysis of consists of three conditions: full forcing, riverine, and tide plus surge. The list of sensitivity runs is presented in Table 4.2.

Table 4.2: Run conditions of sensitivity analysis

Scenarios	**Descriptions**
Baseline	Full forcing, including forcing from tides, surges, and rivers
Tide + Surge	Base model forced with the tide and surge
Rainfall	Base model forced with rainfall on the grids

We performed a series of sensitivity simulations for each of the three storms, such as Isaac (2012), 2016 Flood, and Ida (2021), to assess the compounding effect caused by each event using the alternative metric defined in the second element of this dissertation.

4.2.8 Calibration Datasets

We extensively calibrated the model for two contrasting events, such as hurricane Issac of 2012, which was a purely surge-dominated storm event, and the 2016 flood, which was driven by heavy rainfall. We calibrated the model for three data sources: USGS water level (Durango Field Office, 2021), the Coastwide Reference Monitoring System (CRMS, 2010), and NOAA stations (NOAA, 2021). For each calibration event, 1-hour time step data was collected, and the datum was corrected from MSL to NAVD88 using the correction factors unique to each station. Out of all of those collected, the data from the NOAA stations exhibit the most tidal effects in both fairweather conditions and during storm events, which is one calibration factor to consider when comparing simulated results. Finally, High Water Marks (HWM) are available through the USGS (USGS, 2021) for both events, at which post-event point observations represent the peak water level. Fig.4.1 shows that the HWMs for the 2012 event are located in the coastal area along the northern bank. In contrast, HWMs are situated in the inland area within the Amite River Basin for the 2016 flood, indicating the type of inundation that likely occurred with each event. This data comes with information such as data quality, reference datum, date of measurement, and notes. To assess and calibrate the model accurately, HWMs with reference datums other than NAVD88 or data quality of "Poor: +/- 0.40 ft" or "VP: > 0.40 ft" were excluded.

4.2.9 Calibration Performance Assessment Criteria

We calibrate the model using a manual method for a rainfall-dominated flood event for the year 2016. In addition, the hydrological module is calibrated for discharge at the Amite Watershed. To calibrate the model, we adjusted the loss factor (i.e., infiltration) by reducing the rainfall inputs by a certain percentage and adjusting the roughness only for the main channels. Whereas the hydrodynamic module is calibrated for observed water levels at USGS and CRMS, and NOAA stations near the Amite River, Lake Maurepas, and Lake Pontchartrain. For calibrating the model, we adjusted the space-varying roughness adopted from the ADCIRC model and checked the numerical simulation's stability by preserving the Courant–Friedrichs–Lewy (CFL) condition, and we set the value as 0.70.

We adopted the conventional metrics employed for judging model performance, including percentage bias (pBias), coefficient of determination (R^2), root mean squared error (RMSE), and Nash–Sutcliffe efficiency (NSE). These metrics are defined as follows:

$$pBias = \frac{\sum_{i=1}^{n}(y_{sim,\mathrm{i}} - y_{obs,i})}{\sum_{i=1}^{n} y_{obs,i}} \times 100 \tag{1}$$

$$\mathrm{R}^2 = [\frac{\sum_{i=1}^{n}(\mathrm{y}_{obs,i} - \bar{y}_{obs,i})(\mathrm{y}_{sim,i} - \bar{y}_{sim,i})}{\sqrt{\sum_{i=1}^{n}(y_{obs,i} - \bar{y}_{obs,i})^2}\ \sqrt{\sum_{i=1}^{n}(y_{sim,i} - \bar{y}_{sim,i})^2}}]^2 \tag{2}$$

$$\mathrm{RMSE} = \sqrt{\frac{\sum_{i=1}^{n}(y_{sim,i} - y_{obs,i})^2}{n}} \tag{3}$$

$$\mathrm{NSE} = 1 - \frac{\sum_{i=1}^{n}(y_{sim,i} - y_{obs,i})^2}{\sum_{i=1}^{n}(y_{obs,i} - \bar{y}_{obs})^2} \tag{4}$$

Where $y_{obs,i}$ and $y_{sim,i}$ denote observation and simulation, respectively, and n is the number of records in the time series.

4.3 RESULTS

4.3.1 Model calibration for surge-dominated Event: Hurricane Isaac (2012)

4.3.1.1 Comparison of Water Level

An important starting point when calibrating for a surge-dominated model is the open boundary in the deep ocean. This should closely reflect the astronomical and storm surge observations if there is any chance of accurately representing its effects further within the domain. Figure 12 below demonstrates the model performance at two NOAA stations within the model domain (Fig. 1) that reflect the storm surge water level elevation during Hurricane Isaac (2012). We see that the model closely represents the timing and magnitude of the peak water level elevation, though slightly underestimates the magnitude. This may be due to lack of account for contributions by waves.

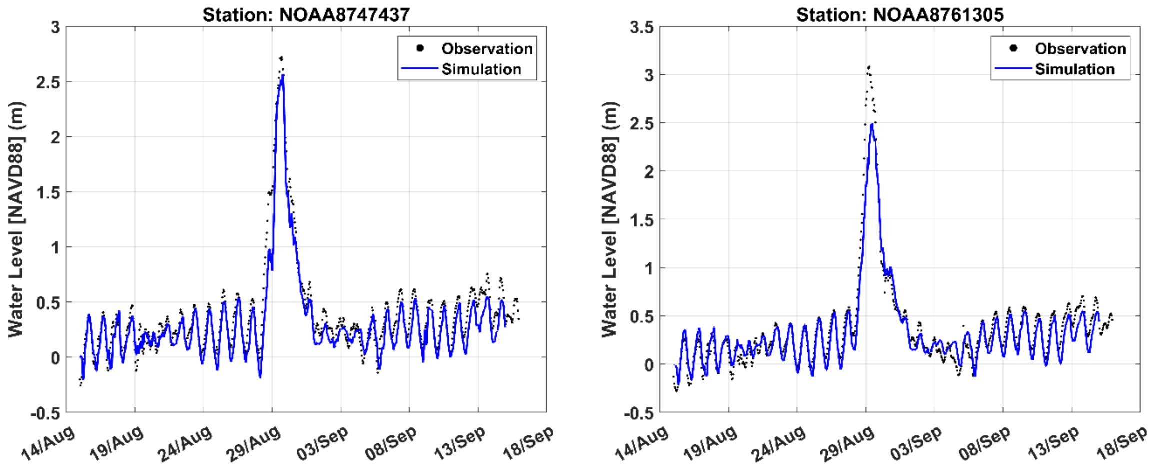

Fig. 4.4: Comparison of observed and simulated water levels at NOAA stations during Hurricane Isaac (2012)

Next, we direct our attention to the various CRMS gauges near Lakes Maurepas and Pontchartrain, where we anticipate observing signs of both surge response alone and compound flooding to locations where rainfall runoff eventually reaches. When comparing water levels in these locations, we have grouped gauges into two categories below. Fig.4.5 represents CRMS gauges where a surge response alone is recorded. This is indicated by a sharp peak in water level followed by a quick recession. The simulation accurately resolves the magnitude and timing of the peak values observed at these locations, and the water level recession towards the end of the event. The discrepancy in the observation periods' beginning and end may result from a coarser resolution mesh or lack of friction calibration.

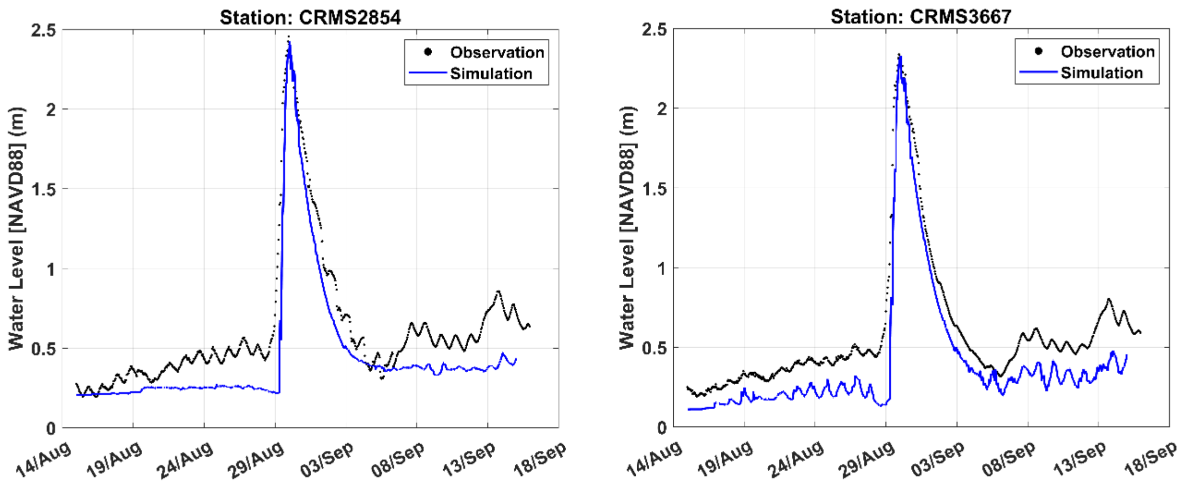

Fig. 4.5: Comparison of observed and simulated water levels at CRMS stations during Hurricane Isaac (2012) indicative of storm surge response only.

The second grouping of gauges reflects more of a compound flooding response, shown in Fig. 4.6. The CRMS gauges listed are located around Lake Maurepas's upstream area (marsh). The characteristics of these observations also closely capture the peak represented by the storm surge but are followed by a much slower recession in water level. The peak is likely due to the rainfall-runoff contribution, reaching these locations and increasing the duration of the inundation observed there. The CRMS gauges at the bottom of Fig. 4.6 demonstrate a slightly quicker water level recession than the observations. The recession may be due to the coarser resolution that cannot accurately represent the fine channels in the marshland. Once more, the slight offset in water level at the beginning and end of the simulation may indicate friction that may require further calibration to capture the tidal signal correctly.

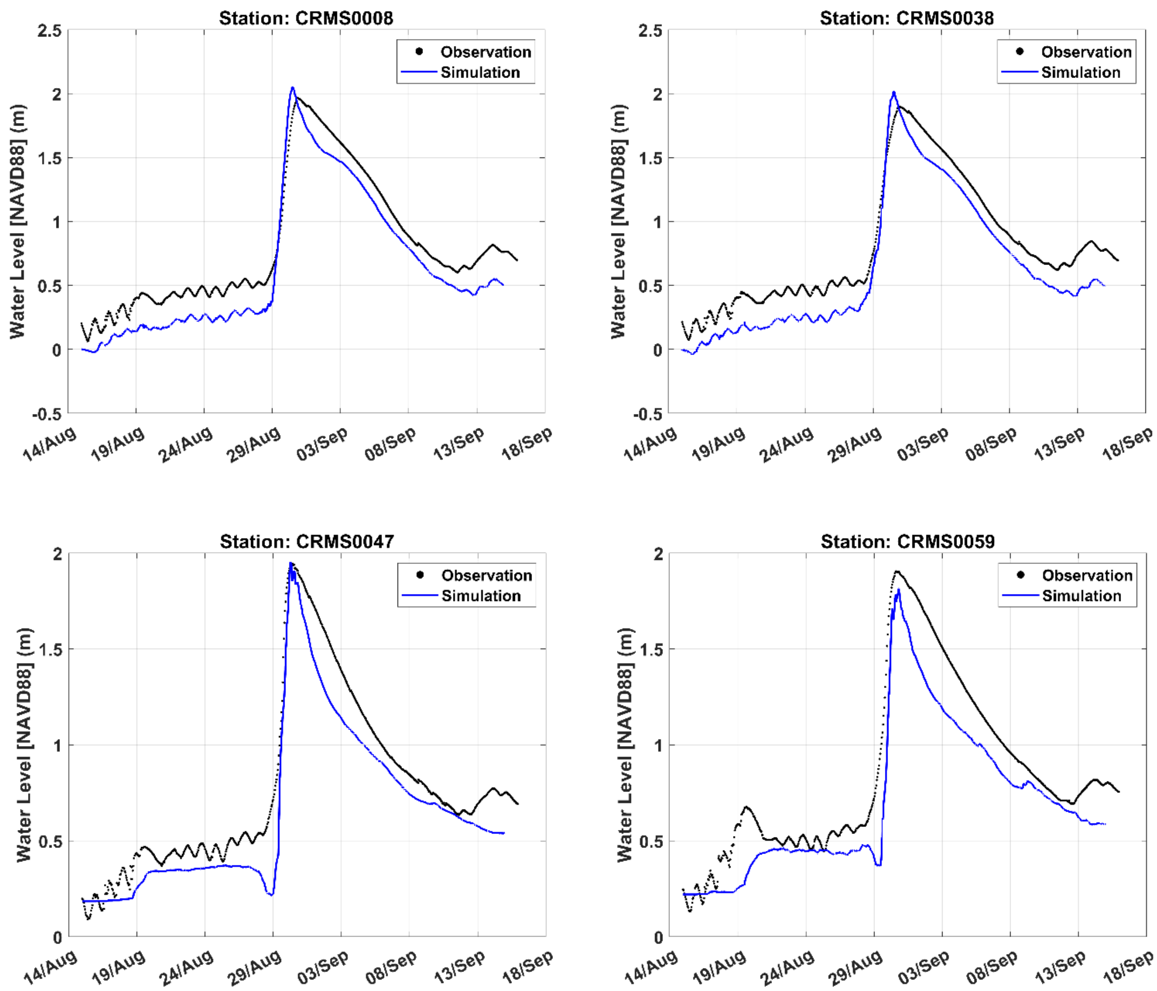

Fig. 4.6: Comparison of observed and simulated water levels at CRMS stations during Hurricane Isaac (2012) indicative of compound flooding response.

Lastly, a comparison of commonly reported error statistics is included for the various observation points throughout the model to communicate a general performance shown in Table 4.3 below. Generally speaking, the model performs reasonably well compared to our observational data for the 2012 event.

Table 4.3: Error Statistics for Surge-dominated 2012 Hurricane Isaac

Stations IDs	RMSE	R-Squared	NSE	pBias
CRMS0008	0.44	0.94	0.24	-36
CRMS0038	0.32	0.94	0.55	-27

CRMS0039	0.41	0.89	-0.25	70
CRMS0046	0.27	0.9	0.73	-16
CRMS0047	0.27	0.92	0.64	-23
CRMS0059	0.18	0.9	0.84	-9
CRMS0061	0.22	0.93	0.78	-14
CRMS0103	0.45	0.75	0.28	-37
CRMS2854	0.37	0.92	0.29	-40
CRMS3667	0.13	0.95	0.91	-5
CRMS5255	0.27	0.92	0.67	-22
USGS7380120	0.44	0.95	0.66	-11
USGS7380200	0.24	0.97	0.81	-13
USGS7380215	0.41	0.93	0.27	-35
USGS73802282	0.21	0.93	0.82	19
NOAA8747437	0.13	0.95	0.92	-17
NOAA8761305	0.12	0.95	0.95	-00

4.3.1.2 Highwater Marks Accuracy

The end state of the calibration run is compared across HWMs to ascertain the model's performance in simulating actual water elevation at points throughout the computational domain. Fig. 4.7. shows a comparison of the observed peak water level with the simulated peak as a scatter plot. This may be due to the fact that many of the USGS-recorded HWMs for Hurricane Isaac fall along the Gulf Coast but outside the finder resolution mesh focused on the Amite River Basin. Figure 1 shows that many of the HWMs for this event are along the southern coast of Mississippi, a location of much coarser resolution in our computational domain when compared with Fig. 4.7. Previous findings of Ye et al. demonstrate that simulated elevation is particularly sensitive to grid resolution (Ye, Huang, *et al.*, 2020).

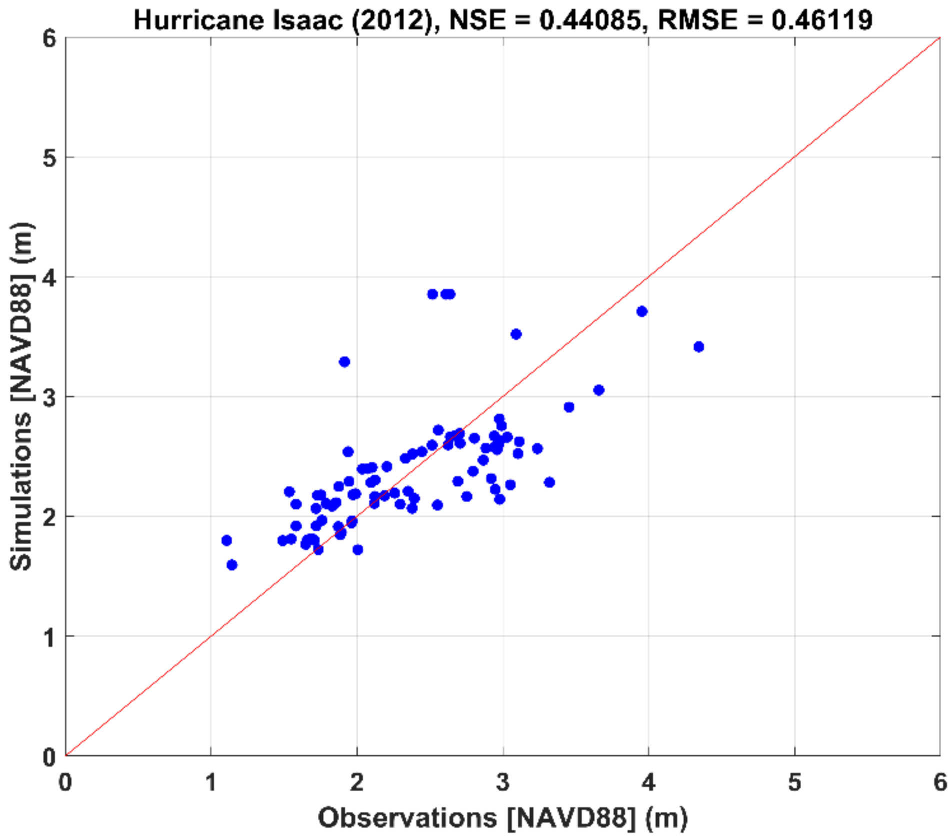

Fig. 4.7: Comparison of observed and simulated HWM elevation for Hurricane Isaac (2012)

4.3.2 Model Calibration for Rainfall-Dominated Event: 2016 flood

4.3.2.1 Comparison of Riverine Flow

We calibrated the model for a rainfall-dominated event, known as the 2016 flood), to enhance its performance. We started the calibration to capture the riverine flow accurately, as the Amite watershed is included in the model. Two comparisons are included in Fig. 4.8 and Fig. 4.9, with accompanying maps denoting the respective gauge's location within the study area. The USGS gauge 7376500 lies in the eastern half of the computational domain, approximately 10 miles north of Lake Maurepas. The simulation results peak timing rises closely with that of the observation, though not quite reaching the observed peak value. It also demonstrates a slighter decrease in flow rate with residual values higher than the observation for the remainder of the event. This decrease can likely be attributed to the coarse resolution of the mesh in this area (Fig. 4.3), which probably does not most accurately reflect the topobathy and finer channels in the area. Additionally, roughness may be a factor to consider adjusting upon review of the local area.

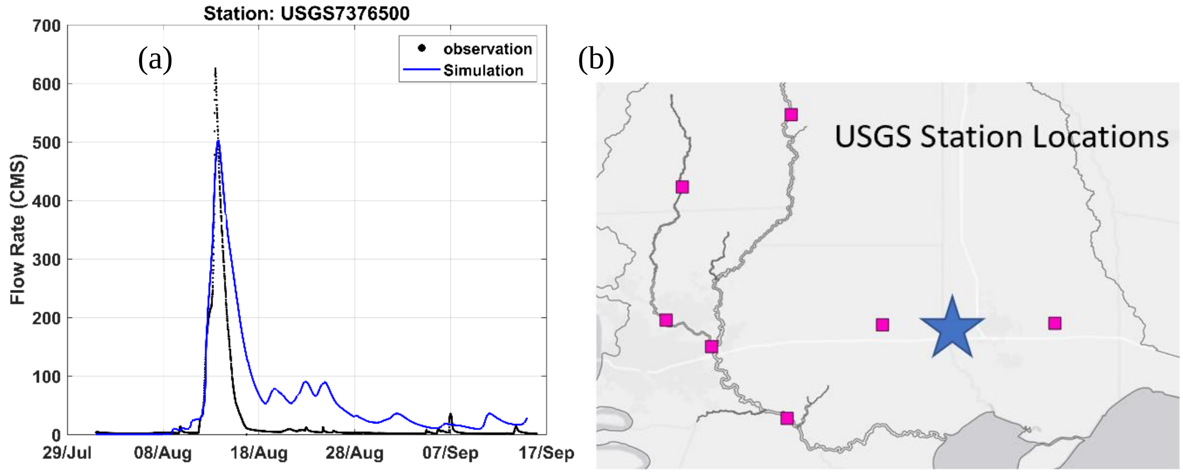

Fig. 4.8: Comparison of flow rate at USGS Gauge 7376500; (a) time-series observation and simulation results and (b) reference map of the location.

The other calibration USGS gauge 7377500 lies high in the Comite River, a tributary to the Amite River, shown in Fig. 4.9. Once more, the simulation peak value does not quite reach the observed peak value and exhibits a slight delay in the reduction of flow rate. However, this simulation curve does achieve a closer flow rate for the remainder of the event (i.e., August 28th and thereafter). The delay and shortfall of peak value can likely be attributed to the coarser resolution of the neighboring topography that contributes runoff to this river. Again, friction factors may also play a role and should be considered for calibration. However, the recession in the flow hydrograph nearly matches the slope of the observed flow hydrograph, potentially a testament to the high resolution of the waterway reflecting appropriate topobathy.

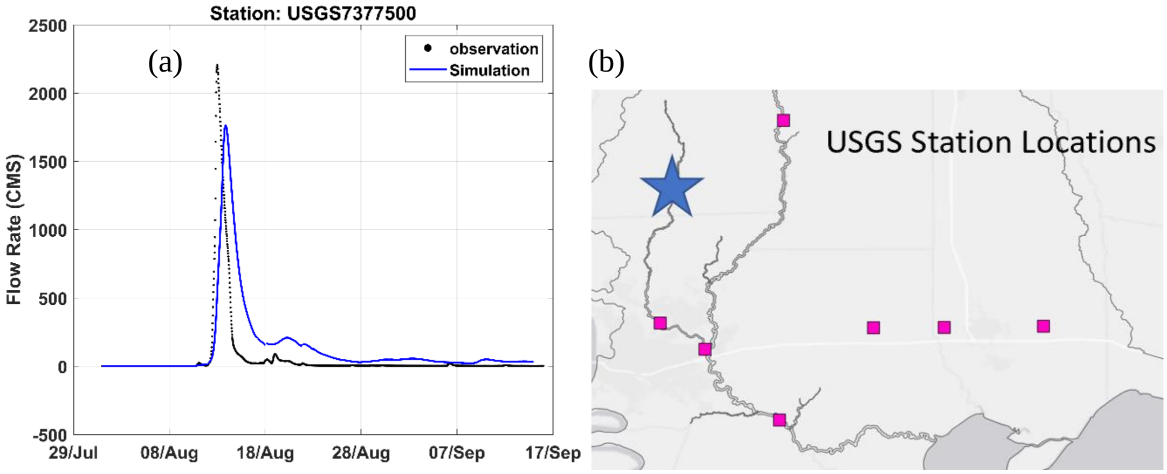

Fig. 4.9: Comparison of riverine flow at USGS Gauge 7377500 (a) time-series observation and simulation results and (b) reference map of the location.

4.3.2.2 Comparison of Water Level

In comparing water levels, we have grouped gauges into figures representing a type of reach within the computational domain. Fig. 4.10 depicts a CRMS gauge and a downstream USGS gauge, which lie in the marshlands near Lake Maurepas. Fig.4.11 represents a collection of USGS gauges that lie upstream along the rivers.

The peak values shown in Fig.4.10 are reasonably simulated in timing. The CRMS location simulation overshoots the observed value, an expected reflection, given that the current run of this model does not account for hydrologic losses through calculations or scaling. The CRMS gauge simulation also demonstrates an elevated water level thereafter, likely due to similar causes. Alternatively, the simulation at the USGS gauge demonstrates an underestimation of the water level but closely follows the reduction trend. This underestimation is likely because USGS gauges are situated near waterways, whereas CRMS are positioned in marshes. Therefore, the USGS gauge positions within the model fall where special attention was given to the resolution of the mesh and likely more accurately represents the topobathy.

The peak values shown in Fig. 4.11 very reasonably reflect the timing of the peak value but once more overshoot or undershoot to varying degrees. We also find that the residual water level on the three plots does not recede as quickly as the observations reflect. This recession is again likely due to the lack of accounting for hydrologic losses in this model. However, applying a scale factor to account for this shortcoming may result in a larger difference between peak values and a consistent underestimation of the maximum peak water level.

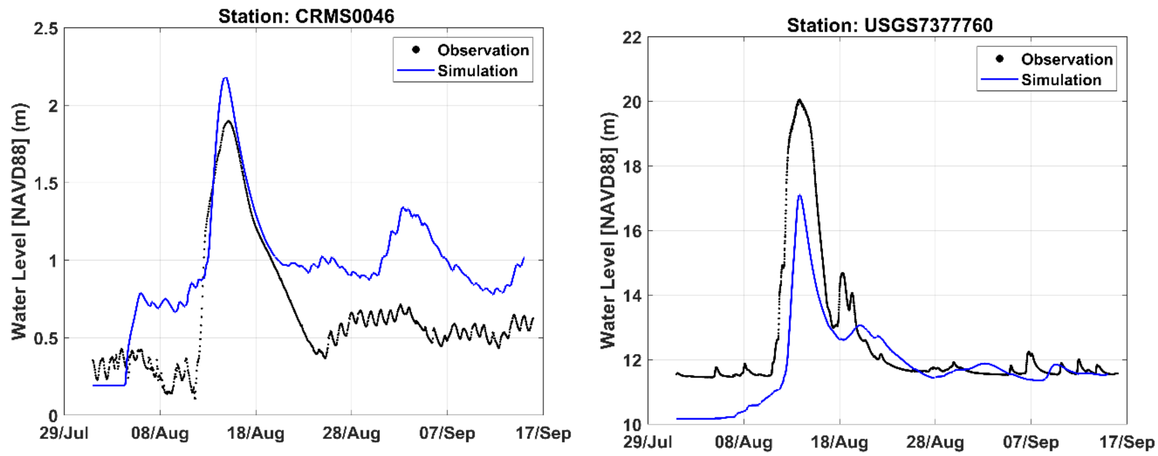

Fig. 4.10: Comparison of observed and simulated water levels at CRMS, and USGS stations, downstream gauge located within marshland immediately west of Lake Maurepas for the 2016 Flood Event.

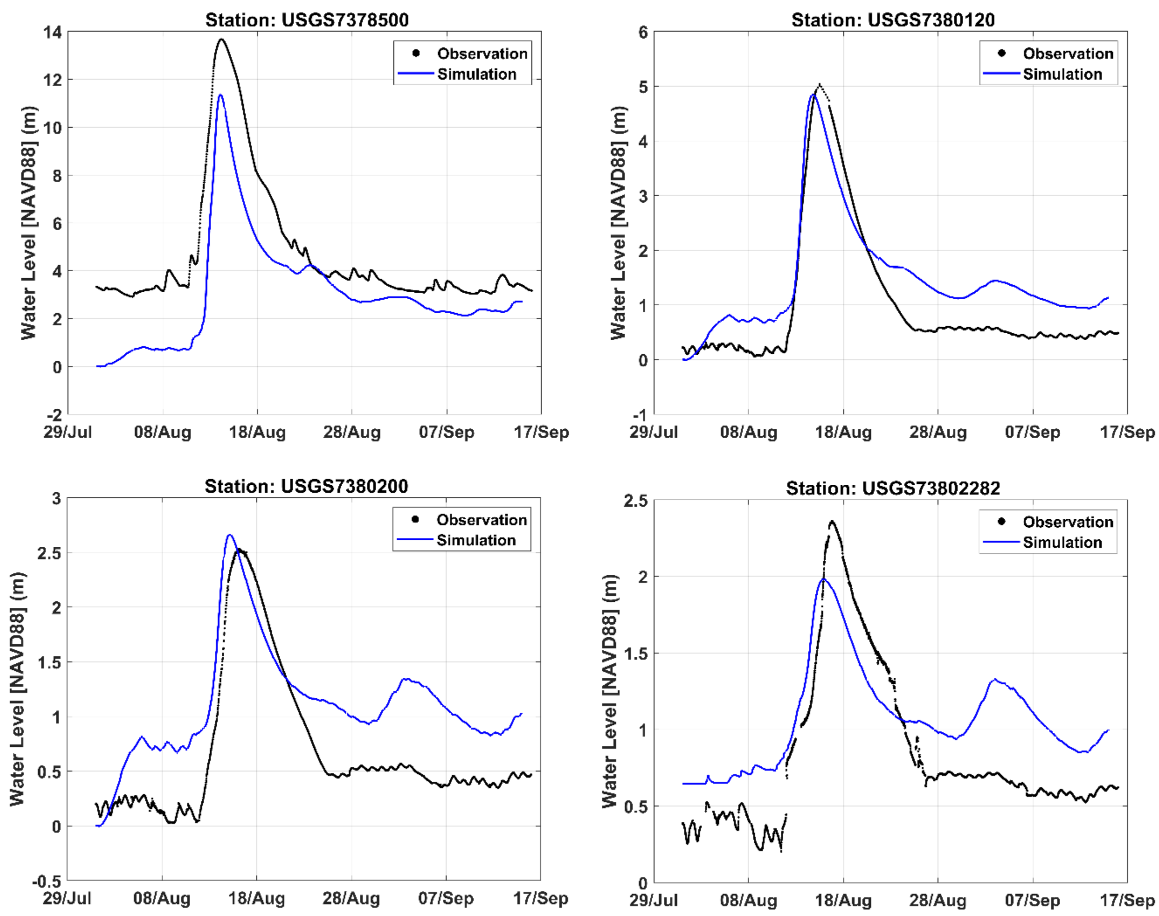

Fig. 4.11: Comparison of observed and simulated water levels along Amite and Comite Rivers for the 2016 Flood Event.

Lastly, a comparison of commonly reported error statistics is included for the various observation points throughout the model to communicate a general performance presented in Table 4.4. The model performance for the rainfall-dominated event still needs to be improved by further calibrating the model. However, at some stations, the performance is relatively well.

Table 4.4: Error Statistics for Rainfall-dominated 2016 Flood Event

2016 Stations	**RMSE**	**R-Squared**	**NSE**	**pBias**
CRMS0008	0.44	0.58	0.5	51
CRMS0046	0.39	0.68	0.51	49
CRMS5845	0.41	0.6	0.50	50
USGS7377760	1.4	0.68	0.53	-5
USGS7378000	1.68	0.77	0.67	-4
USGS7380120	0.61	0.89	0.69	52

4.3.3 Compound Flooding Across Storms

To determine the compound zone by distinguishing the contributions from rainfall and surge for the entire model domain, we run the calibrated hydrodynamic model by turning on and off the rain-on-grid scheme for all three events, such as Isaac (2012), 2016 Flood, and Ida (2021). Then we generated the dominance map using the alternative metric defined in the second element of this study. Besides dominance maps, we selected three stations located in three regions to compare the water level time series from each force. The water level comparison locations are shown in Fig.4.12. The comparison of observed and simulated water levels with the rainfall and surge contribution for Hurricane Isaac (2012) are shown in Fig. 4.13, whose locations are presented in Fig. 4.12. The figure shows that the upstream stream (i.e., USGS 7378500) demonstrates only the rainfall contribution. However, the surge did not reach this point, confirming that the location is rainfall-dominated.

Similarly, the subsequent CRMS and NOAA staions are located downstream of Amite River Basin and have minor rainfall contributions, ensuring the surge-dominated zones. However, there is little contribution from rainfall for CRMS stations situated in the middle of the zone, which is lake Poncertrain. The rainfall contribution at this station mainly comes from the upstream riverine flows, coming from outside the model domain.

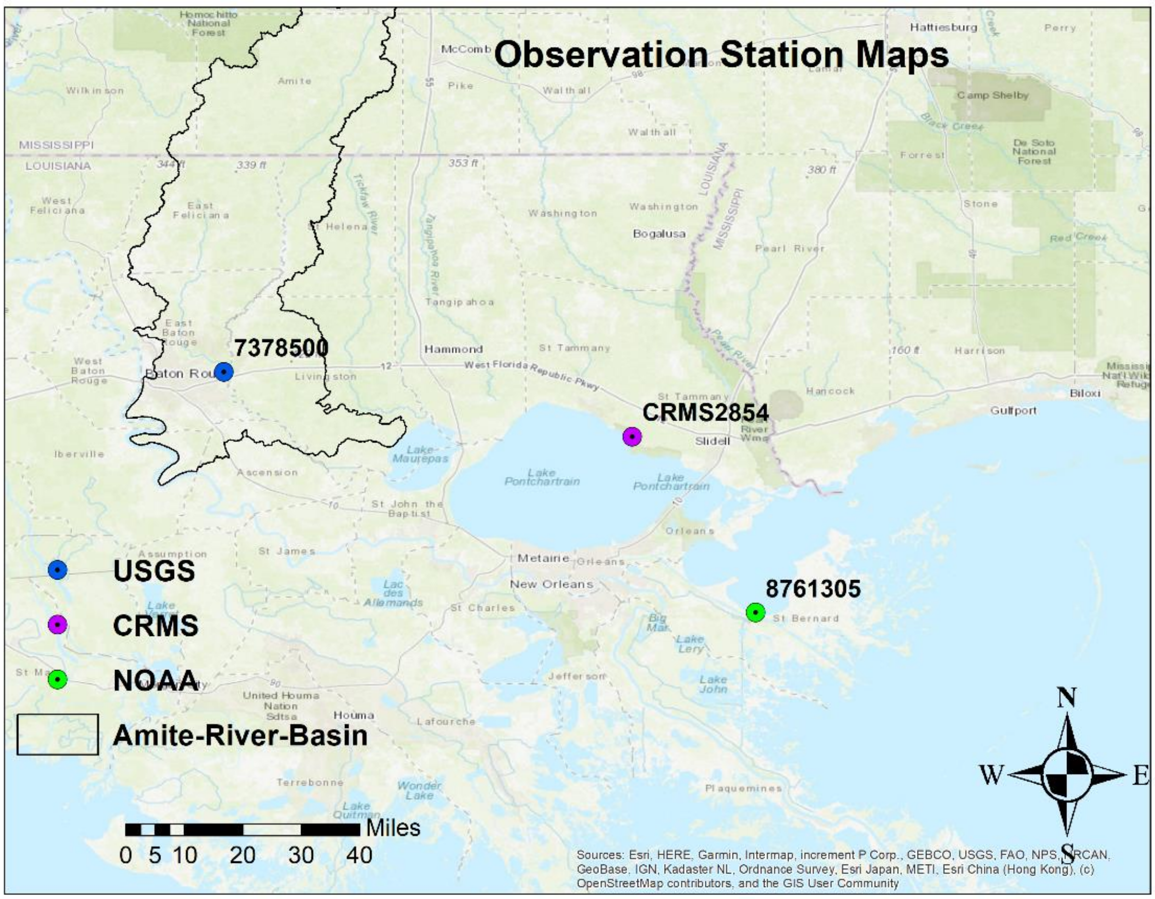

Fig. 4.12: Location map for water level comparison for all three events

Moreover, the storm peaks at these locations were formed at different times. Gradually delayed peaks were observed as they moved to the upstream areas, resulting in fewer chances of developing compound flooding. So, from this result analysis, it can be concluded that Hurricane Isaac (2012) did not demonstrate significant compound flooding in the Amite River Basin; as a surge-dominated event, major flooding was mainly due to storm surges.

Fig. 4.14 shows the water level comparison at three locations for the flood event of 2016. The figure shows that the event is rainfall-dominated, showing a very high peak only at the upstream USGS stations and negligible surges for CRMS and NOAA stations. The little surges at the downstream stations are due to the local rainfall and contribution from the riverine land boundary conditions. As the event was rainfall-dominated, no observable peaks are visible for the downstream areas, nearby Lake Maurepas and Lake Pontchartrain. So, being a rainfall-dominated storm, it caused massive flooding in the upstream watersheds with no compounding effect.

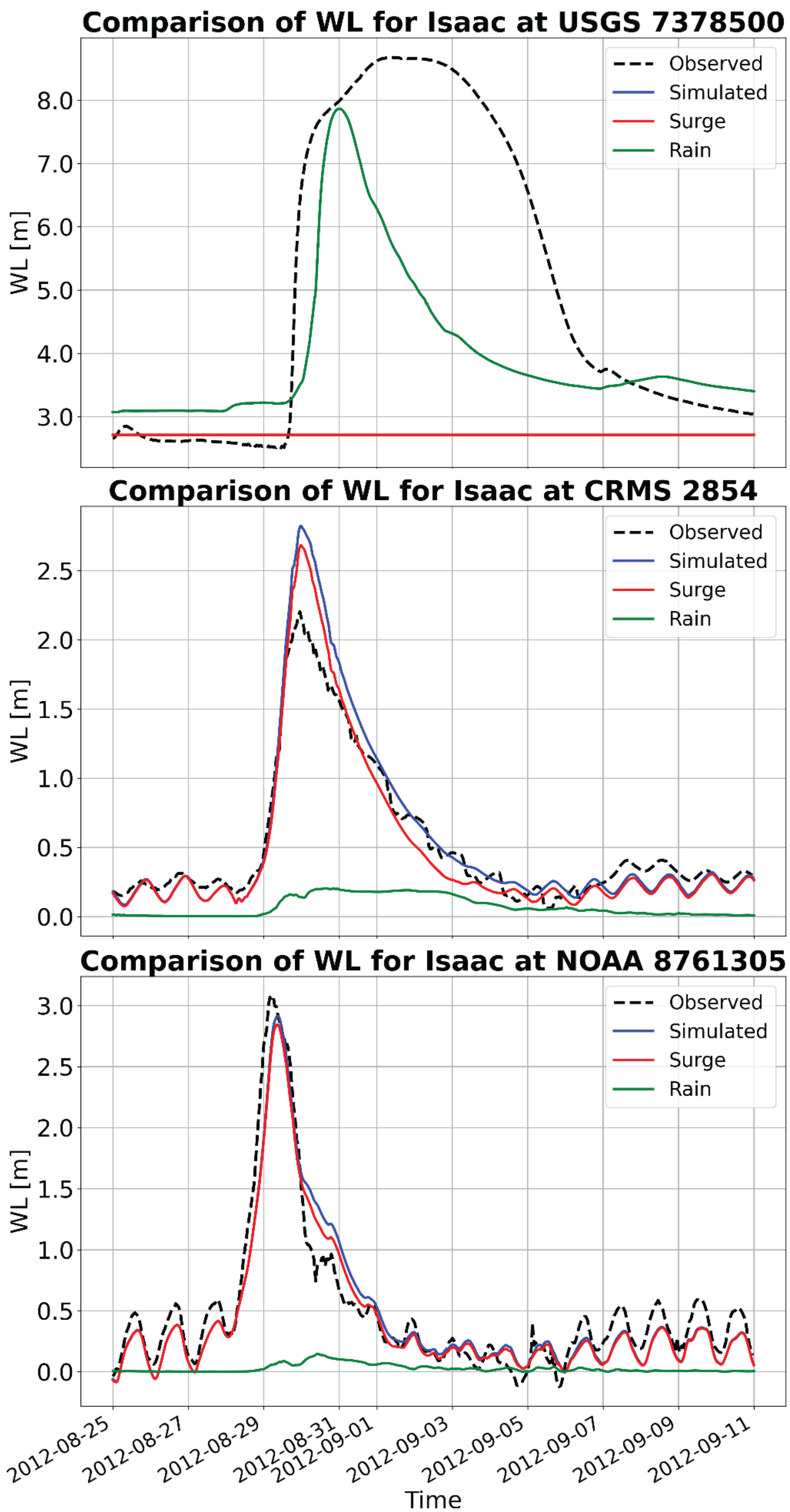

Fig. 4.13: Water level comparison at three locations for Hurricane Isaac (2012)

The comparison of stormwater levels, rainfall, and surge contributions is shown in Fig. 4.15 for Hurricane Ida (2021). Here we simulated the stormwater level using the calibrated model for the Isaac and 2016 flood events. Therefore, we did not restrict the analysis to water level time series; instead, we generated the dominance map to identify the locations where surge and rainfall dominate. Also, we have identified the significant compound zones using an alternative metric we introduced in the second element of this study. This event is different from the other two (i.e., Isaac and the 2016 flood). Ida has a more intense surge because of the very high wind speed (i.e., 240 km/h), which is why the compound zone moves further upstream. as we can see from the figure, the storm peak at the upstream USGS station is so prolonged that it intercepts the surges and rainfall together. Hence, there is a possibility of demonstrating compound flooding. But, still, we can notice that the rainfall-dominated zones are free of surge contribution and vice-versa.

A dominance map is shown in Fig.4 .16, where we calculated the contribution of surges and rainfall separately compared to the full forcing conditions. The dominance map shows some compound zones demoted by green (Fig. 4.16). The entire Amite River Basin is rainfall dominant, whereas lake Maurepas and Pontchartrain are surge-dominant. These low-lying areas are directly connected to the Gulf of Mexico, and the topography is so flat compared to the Amite River Basin, allowing easy access to surges during any hurricane event.

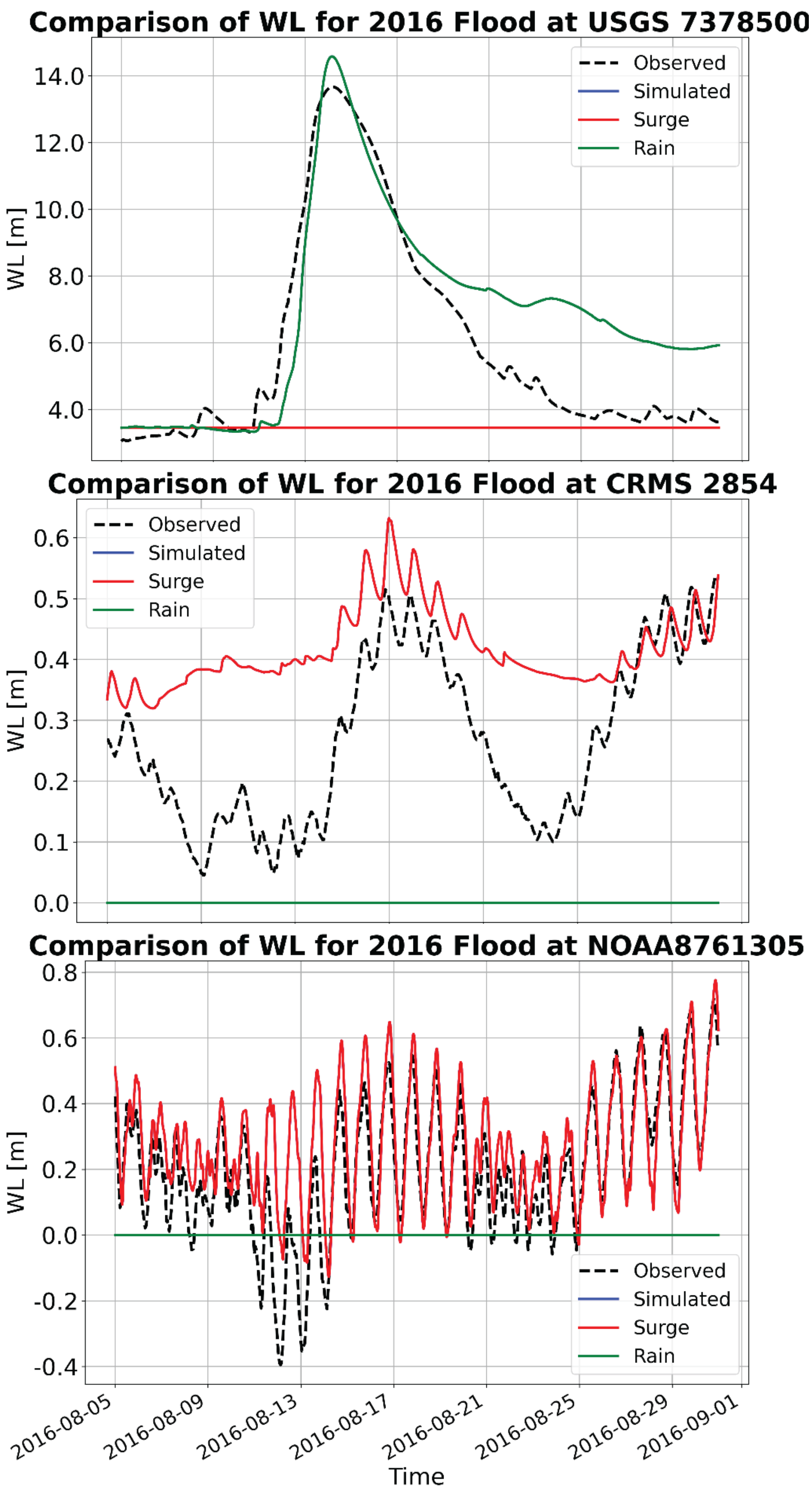

Fig. 4.14: Water level comparison at three locations for the 2016 Flood

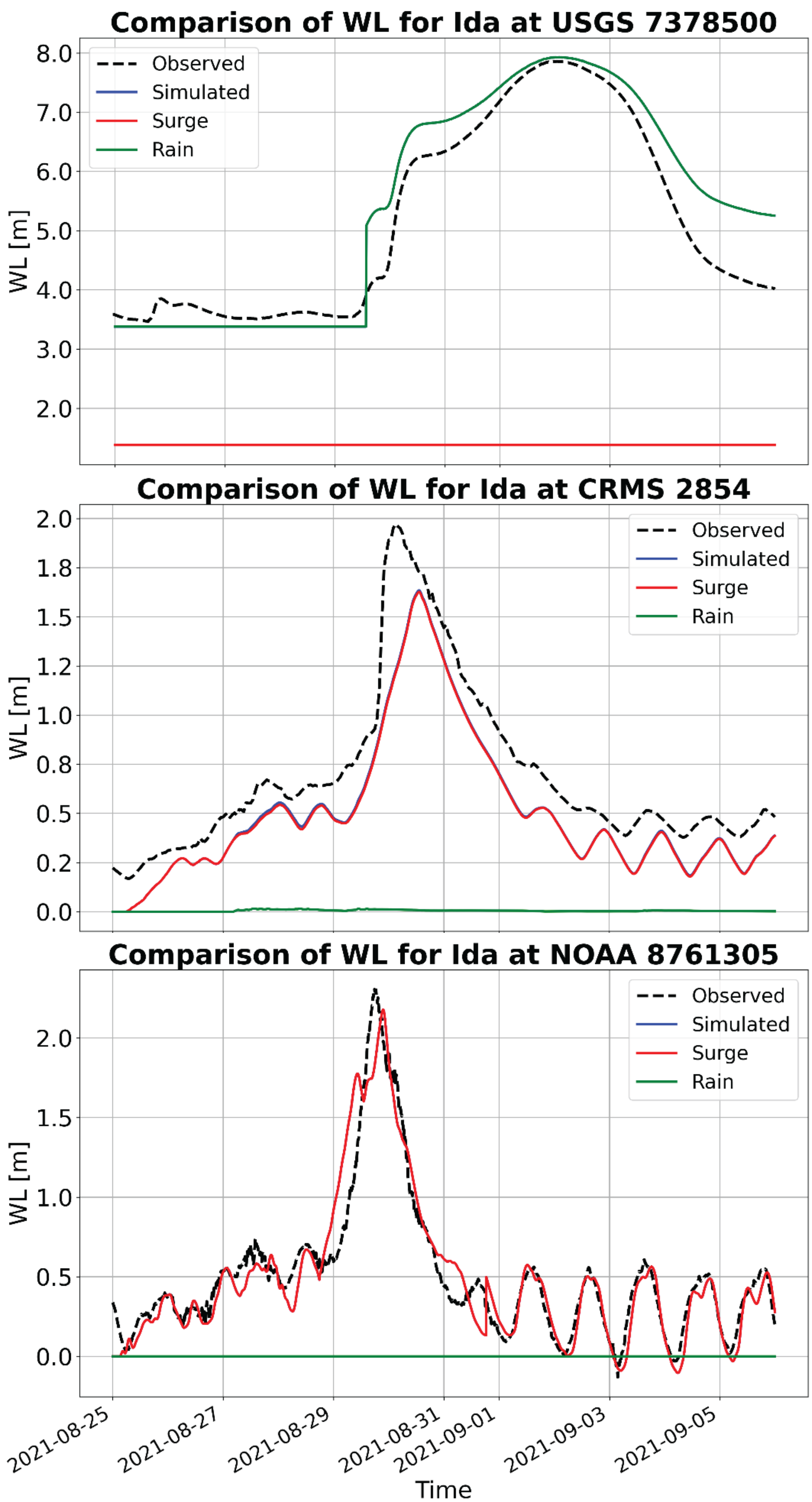
Comparison of WL for Ida at USGS 7378500
WL [m]
Observed
Simulated
Surge
Rain
Comparison of WL for Ida at CRMS 2854
WL [m]
Observed
Simulated
Surge
Rain
Comparison of WL for Ida at NOAA 8761305
WL [m]
Observed
Simulated
Surge
Rain
2021-08-25
2021-08-27
2021-08-29
2021-08-31
2021-09-01
2021-09-03
2021-09-05
Time

Fig. 4.15: Water level comparison at three locations for Hurricane Ida (2021)

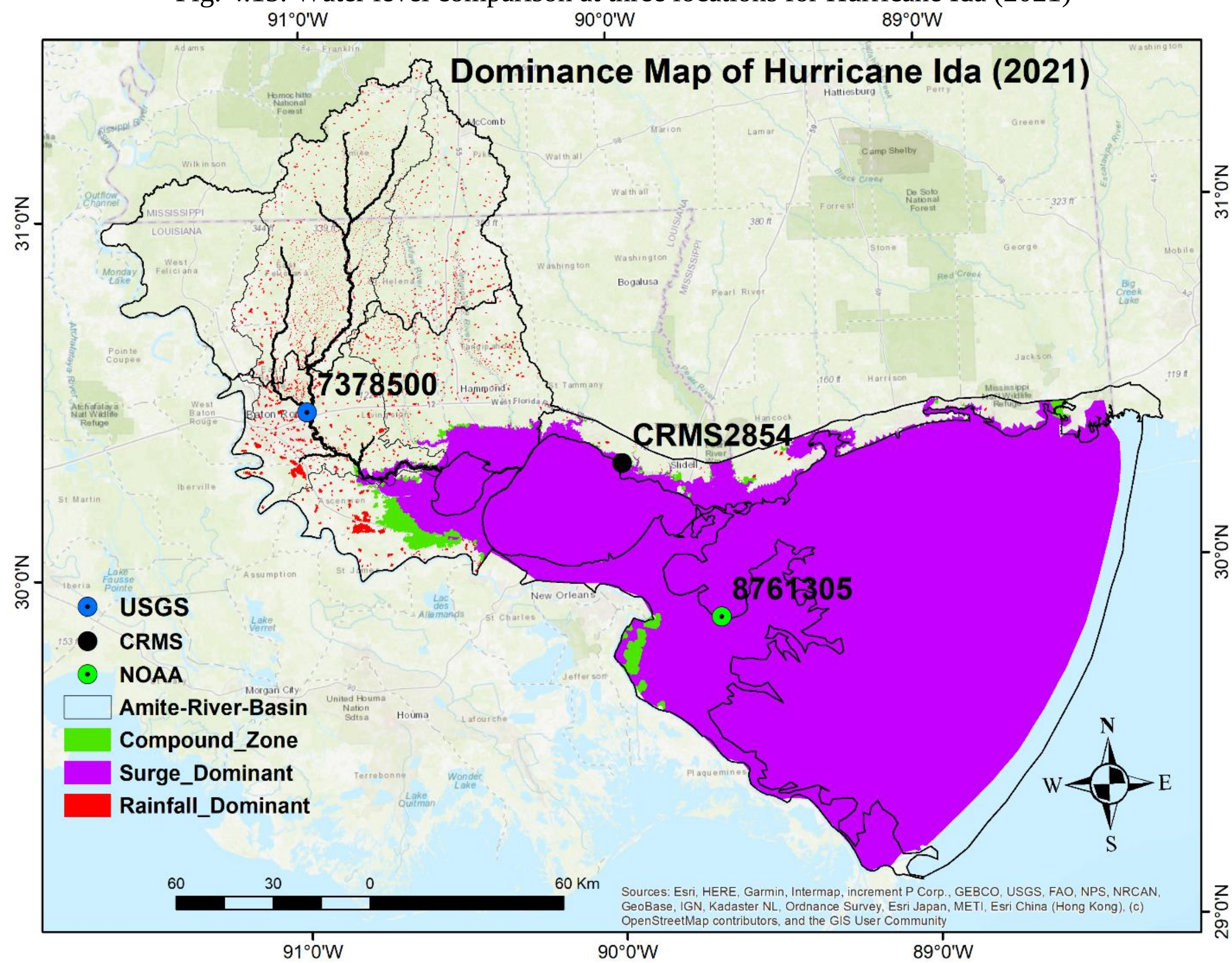

Fig. 4.16: Dominance map showing compound zones for Hurricane Ida (2021)

4.4 DISCUSSIONS

The storm structure plays a vital role in demonstrating compounding effects. Because the behavior of a surge-dominated event differs from that of a rainfall-dominated event, both have separate dominant zones. Our hypothesis is the purely surge-dominated hurricane event is responsible for flooding in the low-lying coastal areas. In contrast, rainfall-dominated flood event causes massive floods in the watersheds. However, when both contributions are present in an event, there is a high chance of developing compound zones, where flood is more severe as it added the peaks from both contributions (i.e., surges and riverine flows). Therefore, it is necessary to study the effect of storm structures on the intensity and location of compound flooding. Moreover, uncertainty in the transition zones exists, contributing to the inaccuracy of assessing the compound zones. This study aims to identify the impacts of different storm structures on the intensity and location of compound flooding over the study region (i.e., Amite River Basin).

The pure rainfall dominant event (i.e., the 2016 flood) demonstrates very high rainfall contribution at the upstream watershed, causing watershed flooding. It is clearly noticeable from the observation time series. Besides, the surge is rarely present at the downstream sites, so there is no dynamic interaction between the rainfall and surge during a rainfall-dominated event. Therefore, there is less chance of developing a compound zone. The flood will be termed as a riverine flood. However, the case of Isaac (2012) demonstrates a high surge along with upstream rainfall. As a result, both upstream and downstream sites were flooded. But the intensity and location of the dynamic interaction between the surge and rainfall were less pronounced than that of Hurricane Ida (2021). Because Hurricane Ida landed with a very high wind speed, causing the compound zone to move upstream location.

The extent of the compound zone produced by Ida is significant only in the middle of the model domain, just upstream of Lake Maurepas. However, from the time series comparison, while calibrating the model for the case of Isacc, these regions were not identified as compound zones because of the less intense surge effects. Instead, they demonstrated individual surges and rainfall effects more intensely. Therefore, the intensity and locations of the dynamic interactions between flood drivers vary with storm intensity.

4.5 CONCLUSIONS

This study has explored the feasibility of modeling compound flooding for various storm structures for the Amite River basin within the framework of a single program to simulate the combined effects of astronomical tide, storm surge, and riverine flow from rainfall runoff. The model was extensively calibrated based on two contrasting events: one dominated by rainfall (i.e., 2016 Flood) and the other dominated by storm surge (i.e., 2012 Hurricane Isaac). The resulting model is anticipated to reasonably simulate events that demonstrate compound flooding aspects. Identifying the effect of storm structures on the intensity and location of compound flooding is the main focus of this study. After successfully developing and calibrating the hydrodynamic model extensively, we conducted a set of numerical experiments for three different storm structures: surge-dominated, rainfall-dominated, and surge with heavy rainfall to study the effects at the upstream watershed in terms of the intensity of surge and rainfall. The specific outcomes are listed below:

i). Compound zones vary among landfalling tropical storms due to the variations in the strengths and evolution of these systems during and after landfall. For instance, Hurricane Ida has a more intense surge due to its high wind speed. As a result, the compound zone moves farther upstream.

ii). The intensity and extent of compound flooding vary upstream and downstream of coastal transition zones, depending on the dynamic interactions between surge, rainfall, and riverine flow.

iii). The rainfall-dominated event causes flooding in the upstream watersheds, whereas the coastal flooding is more pronounced in downstream regions produced by a surge-dominant event. To develop a compound zone, the dynamic interaction among flood drivers is a must, and those interactions can be identified by the alternative metric defined in this study.

The compound zone can be identified by water level comparison contributed by each flood driver, such as surge, tide, rainfall, riverine flow, and lateral flow at different locations, and by generating a dominance map using appropriate metrics. The observation points throughout the model can provide insight into the extent of the transition zone. Identifying the extent of the transition zone inland can ascertain the ideal coupling boundary of this type of model with the outputs from the National Water Model (NWM). Understanding the transition boundary for different storm structures can inform efforts in modeling wholly coastal physical processes, such as waves and setup. Additionally, redefining the model domain from the transition zone to an appropriate ocean boundary location can better complement the efforts of the National Water Center to accurately represent the impacts of storm surges and storm effects on compound flooding in coastal areas.

One of the shortcomings of this model is that it does not account for hydrologic losses within the program's calculations. Defining specific areas of concern by cross-referencing land use with topographic characteristics of areas prone to compound flooding before developing a model can better inform the mesh resolution required to find the appropriate balance of accuracy in results and computational demand. Future work that would complement this effort is a focus on modeling from the transition zone boundary to various extents into the ocean boundary to determine the ideal resolution and extent of the computational domain that reasonably accounts for the critical coastal processes that contribute to compound flooding. These models should be able to provide a more accurate contribution of coastal processes towards storm surges and other effects contributing to coastal flooding and compound flooding in the transition zone.

Chapter 5 General Conclusions and Future Research Recommendations

The dissertation features investigations that explore potential mechanisms to improve the prediction and analysis of coastal flooding, particularly compound flooding produced by a combination of rainfall, surge, and riverine flow. It consists of three elements. The first one focuses on the errors associated with meteorological forcing inputs to coastal models for predicting coastal compound flooding, wherein we examine potential improvements to storm surge simulations through the introduction of numerical weather model analysis in place of conventional parametric model-based wind fields. The second one explores the use of alternative metric to identify coastal zones where intensive interactions among forcings occurred and resulted in significant changes to the magnitude of flooding. The third one analyzes variations in the interactions of forcings that underlie extreme flooding during major tropical storm landfalls that were driven by the evolution and propagation of storm systems through landfall.

The first study, documented in Chapter 2, highlights the challenges of producing accurate forcings for coastal flood simulations. The experiment reveals key deficiencies in a current, widely used parametric wind model that are most likely shared by other contemporary parametric models. These deficiencies, including a lack of representation of background wind and an inability to resolve the evolution of storm structure after landfall, translate into large biases and errors in storm surge simulations. These deficiencies can be addressed through the introduction of numerical weather model analysis and forecasts, whose physical realism may substantially improve the analysis of surges. However, even the state-of-art numerical model reanalysis still exhibits shortcomings after landfall, and the associated errors require further analysis and quantifications.

The alternative metric introduced in Chapter 3 provides the ability to identify zones where dynamic interactions occur among flood drivers. This addresses important gaps in current literature where a compound zone is defined simply using maximum inundation levels without accounting for the timing lags among drivers. Applying this metric to Hurricane Florence demonstrates that dynamic interactions were the most intense over the upstream end of the compound zone. In the remaining portion of the compound zone, the flooding process can be reproduced by the superposition of impacts of individual forcing, e.g., wind and precipitation. Using the metric will allow for refined mapping of zones where compound effects need to be fully accounted for to accurately determine the flooding risks as measured by the probability of inundation depths.

Chapter 4 illustrates the variations in the compound zones among landfalling tropical storms due to the variations in the strengths and evolution of these systems during and after landfall. In addition, it highlights the difficulty in identifying the contributions from each driver over the intermediate zones where both wind and precipitation could contribute to fast rises in water level. This limitation is especially acuate over regions with a complex distribution of inland water bodies that may produce localized surges, such as coastal Louisiana. Currently, the observational networks for wind and water levels in many coastal regions are insufficiently dense data to identify the contributions from various drivers. Establishing more extensive observational systems will be an important first step towards better understanding the interactions and building more robust modeling frameworks to predict better and reconstruct coastal flooding and more accurately assess their risks.

This dissertation illustrates challenges and also highlights opportunities to address these challenges. Improving observational networks to better capture forcings as well as the inundation process through landfall will contribute to enhancements of numerical weather and coastal hydrodynamic models. It will help more precisely define compound zones and compound effects. When combined, these will lead to better prediction and risk assessment systems that will improve the resilience of coastal communities against future flooding events.

Bibliography

Abdolali, A., A. van der Westhuysen, Z. Ma, A. Mehra, A. Roland, and S. Moghimi, 2021. Evaluating the Accuracy and Uncertainty of Atmospheric and Wave Model Hindcasts during Severe Events Using Model Ensembles. Ocean Dynamics 71:217–235.

Acosta-Morel, M., V.P. McNulty, M.W. Beck, N. Lummen, and S.R. Schill, 2021. Shoreline Solutions: Guiding Efficient Data Selection for Coastal Risk Modeling and the Design of Adaptation Interventions. Water (Switzerland) 13:1–22.

Adelekan, I.O., 2011. Vulnerability Assessment of an Urban Flood in Nigeria: Abeokuta Flood 2007. Natural Hazards 56:215–231.

Al-Asadi, K. and J.G. Duan, 2017. Assessing Methods for Estimating Roughness Coefficient in a Vegetated Marsh Area Using Delft3D. Journal of Hydroinformatics 19:766–783.

Annane, B., B. Mcnoldy, S.M. Leidner, R. Hoffman, R. Atlas, and S.J. Majumdar, 2018. A Study of the HWRF Analysis and Forecast Impact of Realistically Simulated CYGNSS Observations Assimilated as Scalar Wind Speeds and as VAM Wind Vectors. Monthly Weather Review 146:2221–2236.

Asher, T.G., R.A. Luettich, J.G. Fleming, and B.O. Blanton, 2019. Low Frequency Water Level Correction in Storm Surge Models Using Data Assimilation. Ocean Modelling 144:101483.

Bacopoulos, P., Y. Tang, D. Wang, and S.C. Hagen, 2017. Integrated Hydrologic-Hydrodynamic Modeling of Estuarine-Riverine Flooding: 2008 Tropical Storm Fay. Journal of Hydrologic Engineering 22:04017022.

Bakhtyar, R., K. Maitaria, P. Velissariou, B. Trimble, H. Mashriqui, S. Moghimi, A. Abdolali, A.J. Van der Westhuysen, Z. Ma, E.P. Clark, and T. Flowers, 2020. A New 1D/2D Coupled Modeling Approach for a Riverine-Estuarine System Under Storm Events: Application to Delaware River Basin. Journal of Geophysical Research: Oceans 125. doi:10.1029/2019JC015822.

Berg, R., 2013. Hurricane Isaac 2012. National Hurricane Center Report:1–78.

Bevacqua, E., D. Maraun, M.I. Vousdoukas, E. Voukouvalas, M. Vrac, L. Mentaschi, and M. Widmann, 2019. Higher Probability of Compound Flooding from Precipitation and Storm Surge in Europe under Anthropogenic Climate Change. Science Advances 5:1–8.

Beven, J.L., A. Hagen, and R. Berg, 2021. NATIONAL HURRICANE CENTER TROPICAL CYCLONE REPORT. Image Courtesy of Noaa/Nesdis/Star:1–163.

Bilskie, M. V. and S.C. Hagen, 2018. Defining Flood Zone Transitions in Low-Gradient Coastal Regions. Geophysical Research Letters 45:2761–2770.

Bilskie, M. V., P. Bacopoulos, and S.C. Hagen, 2019. Astronomic Tides and Nonlinear Tidal Dispersion for a Tropical Coastal Estuary with Engineered Features (Causeways): Indian River Lagoon System. Estuarine, Coastal and Shelf Science 216:54–70.

Biswas, M.K., S. Abarca, L. Bernardet, I. Ginis, E. Grell, M. Iacono, E. Kalina, B. Liu, Q. Liu, T.P. Marchok, A. Mehra, K. Newman, J. Sippel, V. Tallapragada, B. Thomas, W. Wang, H.R. Winterbottom, and Z. Zhang, 2018. Hurricane Weather Research and Forecasting (HWRF) Model: 2018 Scientific Documentation. :1–112.

Blake, E.S. and E.N. Rappaport, 2001. The Deadliest, Costliest, and Most Intense United States Tropical Cyclones from 1851 to 2006 (and Other Frequently Requested Hurricane Facts). NOAATechnical Memorandum NWS TPC-5 2006:1–45.

Broomans, P., S. Blanes, F. Casas, J. a. Oteo, J. Ros, a.I. Delis, T. Katsaounis, A. Bátkai, E. Sikolya, A.H. Al-Mohy, N.J. Higham, A. Bátkai, E. Sikolya, P. Broomans, a. I. Delis, T. Katsaounis, D.L. George, I. An, R. Obert, H. Ath, C. González, a. Ostermann, M. Thalhammer, M. Hochbruck, C. Lubich, a. Iserles, S.P. Nørsett, a. F. Rasmussen, J. Jakeman, W. To, E. Of, I. Faragó, Á. Havasi, R. Horváth, J. Hudson, P. Crowhurst, J.G. Zhou, D.M. Causon, D.M. Ingram, C.G. Mingham, S.L. Belousov, L.V.B.I.G. Sitnikov, and V. a Shnaidman, 2003. In Solutions of The. Applied Mathematical Modelling 29:754–783.

Bucci, L.R., S.J. Majumdar, R. Atlas, G.D. Emmitt, and S. Greco, 2021. Understanding the Response of Tropical Cyclone Structure to the Assimilation of Synthetic Wind Profiles. Monthly Weather Review 149:2031–2047.

Bunya, S., J.C. Dietrich, J.J. Westerink, B.A. Ebersole, J.M. Smith, J.H. Atkinson, R. Jensen, D.T. Resio, R.A. Luettich, C. Dawson, V.J. Cardone, A.T. Cox, M.D. Powell, H.J. Westerink, and H.J. Roberts, 2010. A High-Resolution Coupled Riverine Flow, Tide, Wind, Wind Wave, and Storm Surge Model for Southern Louisiana and Mississippi. Part I: Model Development and Validation. Monthly Weather Review 138:345–377.

Cardone, V.J. and A.T. Cox, 2009. Tropical Cyclone Wind Field Forcing for Surge Models: Critical Issues and Sensitivities. Natural Hazards., pp. 29–47.

Chang, H., J. Franczyk, and C. Kim, 2009. What Is Responsible for Increasing Flood Risks? The Case of Gangwon Province, Korea. Natural Hazards 48:339–354.

Chao, X., Y. Jia, S.S.Y. Wang, and A.K.M.A. Hossain, 2012. Numerical Modeling of Surface Flow and Transport Phenomena with Applications to Lake Pontchartrain. Lake and Reservoir Management 28:31–45.

Chavas, D.R., N. Lin, and K. Emanuel, 2015. A Model for the Complete Radial Structure of the Tropical Cyclone Wind Field. Part I: Comparison with Observed Structure. Journal of the Atmospheric Sciences 72:3647–3662.

Chen, W.B., W.C. Liu, and M.H. Hsu, 2012. Predicting Typhoon-Induced Storm Surge Tide with a Two-Dimensional Hydrodynamic Model and Artificial Neural Network Model. Natural Hazards and Earth System Science 12:3799–3809.

Chen, X.M., S.H. Chen, J.S. Haase, B.J. Murphy, K.N. Wang, J.L. Garrison, S.Y. Chen, C.Y. Huang, L. Adhikari, and F. Xie, 2018. The Impact of Airborne Radio Occultation Observations on the Simulation of Hurricane Karl (2010). Monthly Weather Review 146:329–350.

Cho, K.H., H. V. Wang, J. Shen, A. Valle-Levinson, and Y. cheng Teng, 2012. A Modeling Study on the Response of Chesapeake Bay to Hurricane Events of Floyd and Isabel. Ocean Modelling 49–50:22–46.

Chow, V.T., 1959. Open Channel Hydraulics. McGraw-Hill Education – Europe, New York, USA.

CRMS, 2010. Coastwide Reference Monitoring System (CRMS). Fact Sheet.

Davis, B., X. Wang, and X. Lu, 2021. A Comparison of HWRF Six-Hourly 4DEnVar and Hourly 3DEnVar Assimilation of Inner Core Tail Dopper Radar Observations for the Prediction of Hurricane Edouard (2014). Atmosphere 12. doi:10.3390/atmos12080942.

Deltares, 2014. Simulationnof Multi-Dimensional Hydrodynamics Flows and Transport Phenomena, Including Sediments. Delft3D-FLOW. User Manual, Hydro-Morphodynamics.

Demaria, M., S.D. Aberson, K. V. Ooyama, and S.J. Lord, 1992. A Nested Spectral Model for Hurricane Track Forecasting. Monthly Weather Review 120. doi:10.1175/1520-0493(1992)120<1628:ANSMFH>2.0.CO;2.

Díaz-Carrasco, P., S. Croquer, V. Tamimi, J. Lacey, and S. Poncet, 2021. Advances in Numerical Reynolds-Averaged Navier–Stokes Modelling of Wave-Structure-Seabed Interactions and Scour. Journal of Marine Science and Engineering 9. doi:10.3390/jmse9060611.

Dietrich, J.C., A. Muhammad, M. Curcic, A. Fathi, C.N. Dawson, S.S. Chen, and R.A. Luettich, 2018. Sensitivity of Storm Surge Predictions to Atmospheric Forcing during Hurricane Isaac. Journal of Waterway, Port, Coastal, and Ocean Engineering 144:04017035.

Dietrich, J.C., M. Zijlema, J.J. Westerink, L.H. Holthuijsen, C. Dawson, R.A. Luettich, R.E. Jensen, J.M. Smith, G.S. Stelling, and G.W. Stone, 2011. Modeling Hurricane Waves and Storm Surge Using Integrally-Coupled, Scalable Computations. Coastal Engineering 58:45–65.

Dietrich, J.C., S. Bunya, J.J. Westerink, B.A. Ebersole, J.M. Smith, J.H. Atkinson, R. Jensen, D.T. Resio, R.A. Luettich, C. Dawson, V.J. Cardone, A.T. Cox, M.D. Powell, H.J. Westerink, and H.J. Roberts, 2010. A High-Resolution Coupled Riverine Flow, Tide, Wind, Wind Wave, and Storm Surge Model for Southern Louisiana and Mississippi. Part II: Synoptic Description and Analysis of Hurricanes Katrina and Rita. Monthly Weather Review 138:378–404.

Durango Field Office, 2021. USGS National Water Information System: Web Interface. Usgs.

Easterling, D.R., G.A. Meehl, C. Parmesan, S.A. Changnon, T.R. Karl, and L.O. Mearns, 2000. Climate Extremes: Observations, Modeling, and Impacts. 289:2068–2075.

Egbert, G.D. and S.Y. Erofeeva, 2002. Efficient Inverse Modeling of Barotropic Ocean Tides. Journal of Atmospheric and Oceanic Technology 19:183–204.

Emanuel, K. and R. Rotunno, 2011. Self-Stratification of Tropical Cyclone Outflow. Part I: Implications for Storm Structure. Journal of the Atmospheric Sciences 68:2236–2249.

Emanuel, K., 2010. Tropical Cyclone Energetics and Structure. Atmospheric Turbulence and Mesoscale Meteorology:165–192.

Fang, P., G. Ye, and H. Yu, 2020. A Parametric Wind Field Model and Its Application in Simulating Historical Typhoons in the Western North Pacific Ocean. Journal of Wind Engineering and Industrial Aerodynamics 199:104131.

Ferreira, C.M., J.L. Irish, and F. Olivera, 2014. Uncertainty in Hurricane Surge Simulation Due to Land Cover Specification. Journal of Geophysical Research: Oceans:3868–3882.

Forbes, C., R.A. Luettich, C.A. Mattocks, and J.J. Westerink, 2010. A Retrospective Evaluation of the Storm Surge Produced by Hurricane Gustav (2008): Forecast and Hindcast Results. Weather and Forecasting 25:1577–1602.

Franklin, J.L., M.L. Black, and K. Valde, 2003. GPS Dropwindsonde Wind Profiles in Hurricanes and Their Operational Implications. Weather and Forecasting 18:32–44.

George J. Arcement, JR., V.R.S., 1989. Guide for Selecting Manning ’ s Roughness Coefficients for Natural Channels and Flood Plains United States Geological Survey Water-Supply Paper 2339. Area 2339:39.

Gori, A., N. Lin, and J. Smith, 2020. Assessing Compound Flooding From Landfalling Tropical Cyclones on the North Carolina Coast. Water Resources Research 56. doi:10.1029/2019WR026788.

Hall, T.M. and J.P. Kossin, 2019. Hurricane Stalling along the North American Coast and Implications for Rainfall. Npj Climate and Atmospheric Science 2:1–9.

Hallegatte, S., C. Green, R.J. Nicholls, and J. Corfee-Morlot, 2013. Future Flood Losses in Major Coastal Cities. Nature Climate Change 3:802–806.

Hasan Tanim, A. and E. Goharian, 2021. Developing a Hybrid Modeling and Multivariate Analysis Framework for Storm Surge and Runoff Interactions in Urban Coastal Flooding. Journal of Hydrology 595:125670.

Hell, B., B. Broman, L. Jakobsson, M. Jakobsson, Å. Magnusson, and P. Wiberg, 2012. The Use of Bathymetric Data in Society and Science: A Review from the Baltic Sea. Ambio 41:138–150.

Herdman, L., L. Erikson, and P. Barnard, 2018. Storm Surge Propagation and Flooding in Small Tidal Rivers during Events of Mixed Coastal and Fluvial Influence. Journal of Marine Science and Engineering 6. doi:10.3390/JMSE6040158.

Hirth, B.D., J.L. Schroeder, C.C. Weiss, D.A. Smith, and M.I. Biggerstaff, 2012. Research Radar Analyses of the Internal Boundary Layer over Cape Canaveral, Florida, during the Landfall of Hurricane Frances (2004). Weather and Forecasting 27:1349–1372.

Holland, G., 2008. A Revised Hurricane Pressure-Wind Model. Monthly Weather Review 136:3432–3445.

Holland, G.J., 1980. An Analytic Model of the Wind and Pressure Profiles in Hurricanes. Monthly Weather Review 108. doi:10.1175/1520-0493(1980)108<1212:AAMOTW>2.0.CO;2.

Holland, G.J., J.I. Belanger, and A. Fritz, 2010. A Revised Model for Radial Profiles of Hurricane Winds. Monthly Weather Review 138:4393–4401.

Houston, S.H. and M.D. Powell, 1994. Observed and Modeled Wind and Water-Level Response from Tropical Storm Marco (1990). Weather and Forecasting 9. doi:10.1175/1520-0434(1994)009<0427:oamwaw>2.0.co;2.

Hu, K., Q. Chen, and H. Wang, 2015. A Numerical Study of Vegetation Impact on Reducing Storm Surge by Wetlands in a Semi-Enclosed Estuary. Coastal Engineering 95:66–76.

Hu, K., Q. Chen, and S.K. Kimball, 2012. Consistency in Hurricane Surface Wind Forecasting: An Improved Parametric Model. Natural Hazards 61:1029–1050.

Jacob, B. and E. V. Stanev, 2021. Understanding the Impact of Bathymetric Changes in the German Bight on Coastal Hydrodynamics: One Step Toward Realistic Morphodynamic Modeling. Frontiers in Marine Science 8:1–18.

Janjic, Z.I., 2004. The NCEP WRF Core. Bulletin of the American Meteorological Society:2093–2113.

Jonkman, S.N., 2005. Global Perspectives on Loss of Human Life Caused by Floods. Natural Hazards 34:151–175.

Jordi, A., N. Georgas, A. Blumberg, L. Yin, Z. Chen, Y. Wang, J. Schulte, V. Ramaswamy, D. Runnels, and F. Saleh, 2019. A Next-Generation Coastal Ocean Operational System. Bulletin of the American Meteorological Society 100:41–53.

Kaiser, G., L. Scheele, A. Kortenhaus, F. Løvholt, H. Römer, and S. Leschka, 2011. The Influence of Land Cover Roughness on the Results of High Resolution Tsunami Inundation Modeling. Natural Hazards and Earth System Science 11:2521–2540.

Keddy, P.A., D. Campbell, T. McFalls, G.P. Shaffer, R. Moreau, C. Dranguet, and R. Heleniak, 2007. The Wetlands of Lakes Pontchartrain and Maurepas: Past, Present and Future. Environmental Reviews 15:43–77.

Kepert, J., 2001. The Dynamics of Boundary Layer Jets within the Tropical Cyclone Core. Part I: Linear Theory. Journal of the Atmospheric Sciences 58:2469–2484.

Kepert, J.D., J. Schwendike, and H. Ramsay, 2016. Why Is the Tropical Cyclone Boundary Layer Not "Well Mixed"? Journal of the Atmospheric Sciences 73:957–973.

Kim, S.J., J.S. Jung, and S. Kang, 2016. Fully Three-Dimensional Reynolds-Averaged Navier–Stokes Modeling for Solving Free Surface Flows around Coastal Drainage Gates. Journal of Hydro-Environment Research 13:121–133.

Kim, Y. joong, T. woo Kim, and J. sung Yoon, 2020. Study on Storm Surge Using Parametric Model with Geographical Characteristics. Water (Switzerland) 12. doi:10.3390/w12082251.

Kloetzke, T., 2019. Simulation and Analysis of Surface Wind Fields during Landfalling Tropical Cyclones.

Knutson, T.R., J.J. Sirutis, G.A. Vecchi, S. Garner, M. Zhao, H.S. Kim, M. Bender, R.E. Tuleya, I.M. Held, and G. Villarini, 2013. Dynamical Downscaling Projections of Twenty-First-Century Atlantic Hurricane Activity: CMIP3 and CMIP5 Model-Based Scenarios. Journal of Climate 26:6591–6617.

Kumbier, K., R.C. Carvalho, A.T. Vafeidis, and C.D. Woodroffe, 2018. Investigating Compound Flooding in an Estuary Using Hydrodynamic Modelling: A Case Study from the Shoalhaven River, Australia. Natural Hazards and Earth System Sciences 18:463–477.

Kwon, I.H. and H. Bin Cheong, 2010. Tropical Cyclone Initialization with a Spherical High-Order Filter and an Idealized Three-Dimensional Bogus Vortex. Monthly Weather Review 138:1344–1367.

Lai, Y., J. Li, X. Gu, C. Liu, and Y.D. Chen, 2021. Global Compound Floods from Precipitation and Storm Surge: Hazards and the Roles of Cyclones. Journal of Climate 34. doi:10.1175/JCLI-D-21-0050.1.

Landsea, C. W., C. Anderson, N. Charles, G. Clark, J. Dunion, J. Fernandez-Partagas, P. Hungerford, C. Neumann, and M. Zimmer, 2004. The Atlantic hurricane database re-analysis project: Documentation for the 1851-1910 alterations and additions to the HURDAT database. Hurricanes

Lawler, S., J. Haddad, and C.M. Ferreira, 2016. Sensitivity Considerations and the Impact of Spatial Scaling for Storm Surge Modeling in Wetlands of the Mid-Atlantic Region. Ocean and Coastal Management 134:226–238.

Lee, C., S. Hwang, K. Do, and S. Son, 2019. Increasing Flood Risk Due to River Runoff in the Estuarine Area during a Storm Landfall. Estuarine, Coastal and Shelf Science 221:104–118.

Leroux, M.D., K. Wood, R.L. Elsberry, E.O. Cayanan, E. Hendricks, M. Kucas, P. Otto, R. Rogers, B. Sampson, and Z. Yu, 2018. Recent Advances in Research and Forecasting of Tropical Cyclone Track, Intensity, and Structure at Landfall. Tropical Cyclone Research and Review 7:85–105.

Leslie, L.M. and G.J. Holland, 1995. On the Bogussing of Tropical Cyclones in Numerical Models : A Comparison of Vortex Profiles. 110:101–110.

Li, M., L. Zhong, W.C. Boicourt, S. Zhang, and D.L. Zhang, 2006. Hurricane-Induced Storm Surges, Currents and Destratification in a Semi-Enclosed Bay. Geophysical Research Letters 33:2–5.

Lin, N. and D. Chavas, 2012. On Hurricane Parametric Wind and Applications in Storm Surge Modeling. Journal of Geophysical Research Atmospheres 117:1–19.

Loveland, M., A. Kiaghadi, C.N. Dawson, H.S. Rifai, S. Misra, H. Mosser, and A. Parola, 2021. Developing a Modeling Framework to Simulate Compound Flooding: When Storm Surge Interacts With Riverine Flow. Frontiers in Climate 2. doi:10.3389/fclim.2020.609610.

Loveland, M., A. Kiaghadi, C.N. Dawson, H.S. Rifai, S. Misra, H. Mosser, and A. Parola, 2021. Developing a Modeling Framework to Simulate Compound Flooding: When Storm Surge Interacts With Riverine Flow. Frontiers in Climate 2. doi:10.3389/fclim.2020.609610.

Lu, P., N. Lin, K. Emanuel, D. Chavas, and J. Smith, 2018. Assessing Hurricane Rainfall Mechanisms Using a Physics-Based Model: Hurricanes Isabel (2003) and Irene (2011). Journal of the Atmospheric Sciences 75. doi:10.1175/JAS-D-17-0264.1.

Lu, X. and X. Wang, 2020. Improving Hurricane Analyses and Predictions with TCI, IFEX Field Campaign Observations, and CIMSS AMVs Using the Advanced Hybrid Data Assimilation System for HWRF. Part II: Observation Impacts on the Analysis and Prediction of Patricia (2015). Monthly Weather Review 148:1407–1430.

Luettich, R.A., J.J. Westerink, and N.W. Scheffner, 1992. ADCIRC: An Advanced Three-Dimensional Circulation Model for Shelves Coasts and Estuaries, Report 1: Theory and Methodology of ADCIRC-2DDI and ADCIRC-3DL, Dredging Research Program Technical Report DRP-92-6.

Ma, Z., B. Liu, A. Mehra, A. Abdolali, A. van der Westhuysen, S. Moghimi, S. Vinogradov, Z. Zhang, L. Zhu, K. Wu, R. Shrestha, A. Kumar, V. Tallapragada, and N. Kurkowski, 2020. Investigating the Impact of High-Resolution Land-Sea Masks on Hurricane Forecasts in HWRF. Atmosphere 11. doi:10.3390/ATMOS11090888.

MacAfee, A.W. and G.M. Pearson, 2006. Development and Testing of Tropical Cyclone Parametric Wind Models Tailored for Midlatitude Application - Preliminary Results. Journal of Applied Meteorology and Climatology 45:1244–1260.

Mattocks, C. and C. Forbes, 2008. A Real-Time, Event-Triggered Storm Surge Forecasting System for the State of North Carolina. Ocean Modelling. doi:10.1016/j.ocemod.2008.06.008.

Mayo, T. and N. Lin, 2019. The Effect of the Surface Wind Field Representation in the Operational Storm Surge Model of the National Hurricane Center. Atmosphere 10:13–16.

Milly, P.C.D., R.T. Wetherald, K.A. Dunne, and T.L. Delworth, 2002. Increasing Risk of Great Floods in a Changing Climate. Nature 415. doi:10.1038/415514a.

Moftakhari, H.R., A. AghaKouchak, B.F. Sanders, D.L. Feldman, W. Sweet, R.A. Matthew, and A. Luke, 2015b. Increased Nuisance Flooding along the Coasts of the United States Due to Sea Level Rise: Past and Future. Geophysical Research Letters 42:9846–9852.

Molteni, F., R. Buizza, T.N. Palmer, and T. Petroliagis, 1996. The ECMWF Ensemble Prediction System: Methodology and Validation. Quarterly Journal of the Royal Meteorological Society 122:73–119.

Mulligan, R., G. Clunies, A. Rey, S. Culver, N. Zaremba, E. Leorri, and S. Mitra, 2019. Estuarine Responses to Long-Term Changes in Inlets, Morphology, and Sea Level Rise. Journal of Geophysical Research: Oceans. doi:10.1029/2018JC014732.

Nadimpalli, R., K.K. Osuri, U.C. Mohanty, A.K. Das, and D. Niyogi, 2021. Effect of Vortex Initialization and Relocation Method in Anticipating Tropical Cyclone Track and Intensity over the Bay of Bengal. Pure and Applied Geophysics. doi:10.1007/s00024-021-02815-x.

Nair, U.S., E. Rappin, E. Foshee, W. Smith, R.A. Pielke, R. Mahmood, J.L. Case, C.B. Blankenship, M. Shepherd, J.A. Santanello, and D. Niyogi, 2019. Influence of Land Cover and Soil Moisture Based Brown Ocean Effect on an Extreme Rainfall Event from a Louisiana Gulf Coast Tropical System. Scientific Reports 9. doi:10.1038/s41598-019-53031-6.

NOAA, 2021. NOAA Tides and Currents High Tide Bulletin Harmful Algal Bloom Forecasts.

NOAA/NCEI-2, 2021. Billion-Dollar Weather and Climate Disasters: Overview. NOAA National Centers for Environmental Information:1–3.

Olabarrieta, M., J.C. Warner, B. Armstrong, J.B. Zambon, and R. He, 2012. Ocean-Atmosphere Dynamics during Hurricane Ida and Nor'Ida: An Application of the Coupled Ocean-Atmosphere-Wave-Sediment Transport (COAWST) Modeling System. Ocean Modelling 43–44:112–137.

Phadke, A.C., C.D. Martino, K.F. Cheung, and S.H. Houston, 2003. Modeling of Tropical Cyclone Winds and Waves for Emergency Management. Ocean Engineering 30:553–578.

Powell, M.D., P.J. Vickery, and T.A. Reinhold, 2003. Reduced Drag Coefficient for High Wind Speeds in Tropical Cyclones. Nature 422:279–283.

Rahman, M.A., Y. Zhang, L. Lu, S. Moghimi, K. Hu, and A. Abdolali, 2022. Relative Accuracy of HWRF Reanalysis and a Parametric Wind Model during the Landfall of Hurricane Florence and the Impacts on Storm Surge Simulations. Springer Netherlands. doi:10.1007/s11069-022-05702-3.

Rao, Y.R., C.R. Murthy, and P.C. Sinha, 2008. The Coastal Ocean. Modelling and Monitoring of Coastal Marine Processes:3–10.

Resio, D.T., N. J. Powell, M. A. Cialone, H.S. Das, and J.J. Westerink, 2017. Quantifying Impacts of Forecast Uncertainties on Predicted Storm Surges. Natural Hazards 88:1423–1449.

Ryan, K., L. Bucci, J. Delgado, R. Atlas, and S. Murillo, 2019. Impact of Gulfstream-IV Dropsondes on Tropical Cyclone Prediction in a Regional OssE System. Monthly Weather Review 147:2961–2977.

Santiago-Collazo, F.L., M. V. Bilskie, and S.C. Hagen, 2019. A Comprehensive Review of Compound Inundation Models in Low-Gradient Coastal Watersheds. Environmental Modelling and Software 119. doi:10.1016/j.envsoft.2019.06.002.

Schloemer, R.W., 1954. Analysis and Synthesis of Hurricane Wind Patterns over Lake Okeechobee, Florida. D. Government Printing Office, Washington (Editor)., p. 31.

Sheng, Y.P., V. Alymov, and V.A. Paramygin, 2010. Simulation of Storm Surge, Wave, Currents, and Inundation in the Outer Banks and Chesapeake Bay during Hurricane Isabel in 2003: The Importance of Waves. Journal of Geophysical Research: Oceans 115. doi:10.1029/2009JC005402.

Smith, S.D. and E.G. Banke, 1975. Variation of the Sea Surface Drag Coefficient with Wind Speed. Quarterly Journal of the Royal Meteorological Society 101:665–673.

Spicer, P., K. Huguenard, L. Ross, and L.N. Rickard, 2019. High-Frequency Tide-Surge-River Interaction in Estuaries: Causes and Implications for Coastal Flooding. Journal of Geophysical Research: Oceans 124:9517–9530.

Stewart and, S.R. and R. Berg, 2019. National Hurricane Center Tropical Cyclone Report: Hurricane Florence:1–125.

Sumich, J.L., 1996. An Introduction to the Biology of Marine Life, Sixth Edition W. C. Brown (Editor). Dubuque, IA.

Tong, M., J.A. Sippel, V. Tallapragada, E. Liu, C. Kieu, I.H. Kwon, W. Wang, Q. Liu, Y. Ling, and B. Zhang, 2018. Impact of Assimilating Aircraft Reconnaissance Observations on Tropical Cyclone Initialization and Prediction Using Operational HWRF and GSI Ensemble-Variational Hybrid Data Assimilation. Monthly Weather Review 146:4155–4177.

Tozer, B., D.T. Sandwell, W.H.F. Smith, C. Olson, J.R. Beale, and P. Wessel, 2019. Global Bathymetry and Topography at 15 Arc Sec: SRTM15+. Earth and Space Science 6. doi:10.1029/2019EA000658.

Uhlhorn, E.W. and D.S. Nolan, 2012. Observational Undersampling in Tropical Cyclones and Implications for Estimated Intensity. Monthly Weather Review 140:825–840.

USDA Forest Service Southern Research Station, HUC 8 Areas in Mississippi.

USGS, 2021. USGS Flood Event Viewer: Providing Hurricane and Flood Response Data. 2018.

USGS, USGS_Baton_Rouge. Geologic Units in East Baton Rouge Parish, Louisiana.

Valle-Levinson, A., M. Olabarrieta, and L. Heilman, 2020. Compound Flooding in Houston-Galveston Bay during Hurricane Harvey. Science of the Total Environment 747:141272.

Vickery, P.J., F.J. Masters, M.D. Powell, and D. Wadhera, 2009. Hurricane Hazard Modeling: The Past, Present, and Future. Journal of Wind Engineering and Industrial Aerodynamics 97:392–405.

Vickery, P.J., P.F. Skerlj, A.C. Steckley, and L.A. Twisdale, 2000. Hurricane Wind Field Model for Use in Hurricane Simulations. Journal of Structural Engineering 126. doi:10.1061/(asce)0733-9445(2000)126:10(1203).

Wahl, T., S. Jain, J. Bender, S.D. Meyers, and M.E. Luther, 2015. Increasing Risk of Compound Flooding from Storm Surge and Rainfall for Major US Cities. Nature Climate Change 5:1093–1097.

Wang, Y., 2012. Recent Research Progress on Tropical Cyclone Structure and Intensity. Tropical Cyclone Research and Review 1:254–275.

Watson, K.M., J.B. Storm, B.K. Breaker, and C.E. Rose, 2017. Characterization of Peak Streamflows and Flood Inundation of Selected Areas in Louisiana from the August 2016 Flood. U.S. Department of the Interior, U.S. Geological Survey: Scientific Investigations Report 2017 – 5005:1–36.

Watson, K.M., J.B. Storm, B.K. Breaker, and C.E. Rose, 2017. Characterization of Peak Streamflows and Flood Inundation of Selected Areas in Louisiana from the August 2016 Flood. U.S. Department of the Interior, U.S. Geological Survey: Scientific Investigations Report 2017 – 5005:1–36.

Weaver, R.J. and D.N. Slinn, 2005. Effect of Wave Forcing on Strom Surge. , pp. 1532–1538.

Willoughby, H.E., J.A. Clos, and M.G. Shoreibah, 1982. Concentric Eye Walls, Secondary Wind Maxima, and the Evolution of the Hurricane Vortex. Journal of the Atmospheric Sciences 39. doi:10.1175/1520-0469(1982)039<0395:CEWSWM>2.0.CO;2.

Willoughby, H.E., R.W.R. Darling, and M.E. Rahn, 2006. Parametric Representation of the Primary Hurricane Vortex. Part II: A New Family of Sectionally Continuous Profiles. Monthly Weather Review 134:1102–1120.

WL | Delft Hydraulics, 1999. Delft3D-FLOW User Manual.

Wunsch, K.E.D. and A.C. Didlake, 2018. Analyzing Tropical Cyclone Structures during Secondary Eyewall Formation Using Aircraft in Situ Observations. Monthly Weather Review 146:3977–3993.

Ye, F., W. Huang, Y. Zhang, S. Moghimi, E. Myers, S. Pe'eri, and H.-C. Yu, 2020. A Cross-Scale Study for Compound Flooding Processes during Hurricane Florence. Natural Hazards and Earth System Sciences:1–24.

Ye, F., Y.J. Zhang, H. Yu, W. Sun, S. Moghimi, E. Myers, K. Nunez, R. Zhang, H. V. Wang, A. Roland, K. Martins, X. Bertin, J. Du, and Z. Liu, 2020. Simulating Storm Surge and Compound Flooding Events with a Creek-to-Ocean Model: Importance of Baroclinic Effects. Ocean Modelling 145. doi:10.1016/j.ocemod.2019.101526.

Yoo, J., J.A. Santanello, M. Shepherd, S. Kumar, P. Lawston, and A.M. Thomas, 2020. Quantification of the Land Surface and Brown Ocean Influence on Tropical Cyclone Intensification over Land. Journal of Hydrometeorology 21:1171–1192.

Zhang, J.A., R.F. Rogers, D.S. Nolan, and F.D. Marks, 2011. On the Characteristic Height Scales of the Hurricane Boundary Layer. Monthly Weather Review 139:2523–2535.

Zhang, Z., J.A. Zhang, G.J. Alaka, K. Wu, A. Mehra, and V. Tallapragada, 2021. A Statistical Analysis of High-Frequency Track and Intensity Forecasts from NOAA's Operational Hurricane Weather Research and Forecasting (HWRF) Modeling System. Monthly Weather Review 149:3325–3339.

Zheng, F., S. Westra, and S.A. Sisson, 2013. Quantifying the Dependence between Extreme Rainfall and Storm Surge in the Coastal Zone. Journal of Hydrology 505:172–187.

Zou, X., Z. Qin, and Y. Zheng, 2015. Improved Tropical Storm Forecasts with GOES-13/15 Imager Radiance Assimilation and Asymmetric Vortex Initialization in HWRF. Monthly Weather Review 143:2485–2505.

Zscheischler, J., S. Westra, B.J.J.M. Van Den Hurk, S.I. Seneviratne, P.J. Ward, A. Pitman, A. Aghakouchak, D.N. Bresch, M. Leonard, T. Wahl, and X. Zhang, 2018. Future Climate Risk from Compound Events. Nature Climate Change 8:469–477.

APPENDIX

Table: Validation stats of barometric pressure during hurricane Florence produced by HWRF and Holland (2010) models

Sensor ID	RMSE (hPa)		R		% BIAS	
	HWRF	Holland	HWRF	Holland	HWRF	Holland
NCBEA11768	0.12	0.21	0.77	0.63	0.30	-0.57
NCBEA11788	0.11	0.19	0.94	0.80	0.33	-0.53
NCBEA11808	0.11	0.19	0.94	0.80	0.34	-0.52
NCBEA13648	0.11	0.18	0.94	0.78	0.36	-0.51
NCBRU11888	0.15	0.16	0.92	0.90	0.23	-0.25
NCBRU11890	0.15	0.16	0.92	0.91	0.23	-0.25
NCBRU11891	0.14	0.15	0.93	0.92	0.24	-0.25
NCBRU11892	0.14	0.15	0.93	0.92	0.24	-0.25
NCBRU12048	0.14	0.16	0.93	0.91	0.22	-0.26
NCBRU12068	0.14	0.16	0.93	0.91	0.22	-0.27
NCCAR00001	0.10	0.19	0.95	0.87	0.21	-0.52
NCCAR00005	0.11	0.20	0.92	0.86	0.15	-0.53
NCCAR00006	0.11	0.27	0.89	0.80	-0.04	-0.75
NCCAR00007	0.11	0.20	0.93	0.85	0.20	-0.53

NCCAR12128	0.11	0.20	0.92	0.83	0.22	-0.53
NCCAR12228	0.11	0.20	0.93	0.86	0.21	-0.52
NCCAR12288	0.11	0.20	0.93	0.85	0.23	-0.51
NCCAR12348	0.11	0.20	0.92	0.85	0.19	-0.53
NCCAR12408	0.11	0.26	0.89	0.80	-0.04	-0.75
NCCAR12409	0.12	0.27	0.87	0.79	-0.06	-0.76
NCCAR12410	0.12	0.27	0.86	0.78	-0.04	-0.76
NCCAR12411	0.11	0.19	0.93	0.86	0.22	-0.47
NCCAR12412	0.11	0.19	0.93	0.86	0.21	-0.47
NCCAR12428	0.10	0.19	0.94	0.86	0.22	-0.51
NCCRA12508	0.10	0.18	0.95	0.86	0.29	-0.51
NCCRA12509	0.10	0.18	0.95	0.87	0.27	-0.51
NCCRA13628	0.10	0.20	0.92	0.83	0.21	-0.55
NCCRV00003	0.10	0.20	0.93	0.84	0.22	-0.54
NCCUR00001	0.07	0.25	0.93	0.48	0.22	-0.76
NCCUR12568	0.08	0.25	0.90	0.49	0.23	-0.73
NCDAR00001	0.07	0.23	0.92	0.75	0.17	-0.70
NCDAR00002	0.08	0.23	0.93	0.74	0.21	-0.67
NCDAR00003	0.08	0.23	0.91	0.72	0.22	-0.68
NCDAR00004	0.08	0.23	0.91	0.72	0.21	-0.68
NCDAR00005	0.08	0.24	0.91	0.65	0.24	-0.70
NCDAR00008	0.08	0.25	0.91	0.49	0.24	-0.72
NCDAR00009	0.08	0.25	0.89	0.55	0.22	-0.73
NCDAR00010	0.06	0.26	0.92	0.68	0.14	-0.79
NCDAR00011	0.07	0.25	0.88	0.55	0.21	-0.74
NCDAR12248	0.11	0.20	0.93	0.85	0.21	-0.52

NCDAR12630	0.08	0.25	0.89	0.55	0.22	-0.73
NCDAR12631	0.08	0.25	0.89	0.55	0.22	-0.73
NCDAR12633	0.08	0.25	0.89	0.55	0.22	-0.73
NCDAR12668	0.07	0.25	0.92	0.57	0.21	-0.74
NCDAR12669	0.07	0.25	0.92	0.57	0.22	-0.73
NCDAR12688	0.08	0.24	0.91	0.65	0.23	-0.70
NCDAR12689	0.07	0.24	0.90	0.67	0.19	-0.74
NCDAR12708	0.06	0.25	0.91	0.68	0.17	-0.75
NCDAR12709	0.06	0.25	0.91	0.68	0.17	-0.75
NCDAR12711	0.06	0.22	0.98	0.85	0.20	-0.70
NCDAR12729	0.07	0.23	0.92	0.75	0.18	-0.69
NCDAR12749	0.07	0.23	0.92	0.75	0.17	-0.70
NCDAR12788	0.06	0.25	0.91	0.68	0.17	-0.75
NCDAR12790	0.08	0.22	0.93	0.74	0.21	-0.67
NCDAR13668	0.07	0.25	0.92	0.57	0.22	-0.74
NCDAR18739	0.07	0.23	0.92	0.75	0.18	-0.69
NCHYD00001	0.08	0.22	0.92	0.76	0.20	-0.66
NCHYD12828	0.06	0.26	0.93	0.74	0.12	-0.78
NCNEW00002	0.16	0.20	0.90	0.88	0.14	-0.33
NCNEW00003	0.16	0.20	0.90	0.88	0.13	-0.34
NCNEW00004	0.18	0.20	0.90	0.88	0.19	-0.29
NCNEW00005	0.18	0.20	0.89	0.88	0.15	-0.33
NCNEW00006	0.17	0.20	0.90	0.88	0.16	-0.32
NCNEW00007	0.17	0.20	0.88	0.87	0.15	-0.36
NCNEW12848	0.18	0.20	0.89	0.87	0.14	-0.35
NCNEW12868	0.18	0.20	0.90	0.87	0.20	-0.30

NCNEW12888	0.18	0.20	0.90	0.88	0.19	-0.29
NCNEW12908	0.18	0.20	0.89	0.87	0.19	-0.29
NCNEW12928	0.18	0.20	0.90	0.87	0.19	-0.30
NCNEW12948	0.19	0.20	0.88	0.87	0.20	-0.29
NCNEW13008	0.18	0.20	0.89	0.88	0.16	-0.33
NCNEW13629	0.16	0.19	0.90	0.89	0.17	-0.32
NCNEW27844	0.18	0.20	0.89	0.87	0.17	-0.31
NCNEW27845	0.18	0.20	0.89	0.87	0.17	-0.31
NCNEW27846	0.19	0.20	0.88	0.87	0.18	-0.31
NCNEW27847	0.18	0.20	0.89	0.87	0.17	-0.31
NCNEW27848	0.18	0.20	0.89	0.87	0.17	-0.31
NCONS00001	0.11	0.20	0.92	0.85	0.17	-0.52
NCONS00002	0.11	0.19	0.94	0.89	0.15	-0.46
NCONS13048	0.12	0.20	0.93	0.88	0.15	-0.46
NCONS13128	0.11	0.21	0.93	0.87	0.08	-0.56
NCONS13168	0.11	0.21	0.93	0.88	0.06	-0.57
NCONS13189	0.11	0.19	0.94	0.90	0.16	-0.46
NCONS13208	0.10	0.21	0.94	0.89	0.08	-0.57
NCONS13228	0.11	0.21	0.90	0.84	0.14	-0.53
NCONS27840	0.12	0.20	0.93	0.88	0.15	-0.46
NCPAM13230	0.10	0.20	0.93	0.84	0.24	-0.54
NCPAM13231	0.10	0.19	0.94	0.84	0.27	-0.52
NCPAM13248	0.08	0.20	0.95	0.85	0.21	-0.59
NCPAM13269	0.08	0.21	0.94	0.83	0.22	-0.59
NCPAS13288	0.03	0.29	0.93	0.51	0.07	-0.89
NCPEN00001	0.16	0.19	0.90	0.88	0.16	-0.36

NCPEN00002	0.14	0.20	0.91	0.89	0.12	-0.42
NCPEN00003	0.14	0.20	0.91	0.89	0.12	-0.42
NCPEN13368	0.40	0.28	0.61	0.57	1.02	0.12
NCPEN13408	0.15	0.20	0.90	0.88	0.12	-0.42
NCPEN27841	0.15	0.20	0.90	0.87	0.13	-0.41
NCPEN27842	0.15	0.20	0.90	0.87	0.13	-0.41
NCPEN27843	0.15	0.20	0.90	0.87	0.13	-0.41
NCBEA11728	0.12	0.22	0.78	0.64	0.27	-0.58